A Comparison of Bistatic Scattering from Two Geologically Distinct Mid-Ocean Ridges

by

Chin-Swee Chia

B.S., Electrical & Electronics Engineering (1993)
Nanyang Technological University

Submitted to the Department of Ocean Engineering
in Partial Fulfillment of the Requirements for the Degree of
Master of Science in Ocean Engineering
at the
Massachusetts Institute of Technology
February 1999

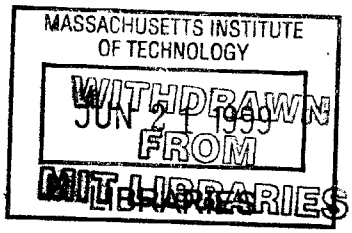

Eng.

Signature of Author .....
Department of Ocean Engineering
January 22, 1999

Certified by .....
Professor Nicholas C. Makris
Assistance Professor of Ocean Engineering
Thesis Supervisor

Accepted by .....
Professor Arthur B. Baggeroer
Ford Professor of Engineering
Chairman, Departmental Committee on Graduate Studies

A Comparison of Bistatic Scattering from Two Geologically Distinct Mid-Ocean Ridges

by
Chin-Swee Chia

Submitted to the Department of Ocean Engineering
in Partial Fulfillment of the Requirements for the Degree of
Master of Science in Ocean Engineering

Abstract

This thesis compares bistatic scattering from two distinct mid-ocean ridges, known as B' and C', via experimental data collected by a system of low-frequency towed arrays. Since B' and C' belong to the two geologically distinct classes of ocean ridges that span the Mid-Atlantic Ridge (MAR), this comparison helps to determine whether their scattering characteristics can be extrapolated to ridges throughout the MAR. Concurrently, the resolving power of a towed-array system in imaging the seafloor geomorphology, and the effects on scattering strength estimation using two different resolutions of bathymetry data at B' are also investigated.

First, the bi-azimuthal scattering strengths of two major scarps at B' are computed using a range-dependent propagation model with supporting bathymetry data sampled at 5-m resolution. Results show that the mean bi-azimuthal scattering strengths (MBASS) of the two major scarps on B' are identical, and roughly equal to the constant of -17dB +/- 8dB. Signal-dependent noise present in the actual data is found to be the primary limiting factor in the bistatic towed-array system's ability to resolve small-scale features (~100-200m scale) along the B' scarps.

The bi-azimuthal scattering strengths of the major scarps at B' and C' are then computed using the supporting 200-m resolution bathymetry data. The MBASS of the B' scarps evaluated at the two different resolutions of bathymetry data are found to differ because of their differing projected area. The difference primarily arises from the under-resolved slope gradients estimated in 200-m resolution sampling. This finding indicates that sufficient sampling of bathymetry data is necessary to accurately estimate the seafloor's scattering strength. Unfortunately, the required sampling is extremely dense and difficult to obtain experimentally.

Our results evaluated at 200-m resolution show that the bi-azimuthal scattering strengths of B' and C' are roughly equal to -11dB +/- 10dB. Specifically, their MBASS are comparable, and are spatially homogenous across the receiver azimuths. Extrapolating the 5-m resolution MBASS obtained at B' to C', and given the similar 200-m MBASS results, we hypothesize that these two mid-ocean ridges can be modeled as diffuse scatterers with a constant bi-azimuthal scattering strength of -17dB +/- 8dB when remotely imaged by the towed-array system at ½ CZ and beyond. This result also suggests that ridges throughout the MAR can be modeled as diffuse scatterers with albedo $\pi/10^{1.7}$.

Thesis Supervisor: Professor Nicholas C. Makris
Title: Assistance Professor of Ocean Engineering

"Some people come into our lives and quickly go. Some stay for a while and leave footprints on our hearts and we are never, ever the same."

~ Chicken Soup for the Soul

Acknowledgments

Although it was a short one-and-half years stay, I have learnt and benefited from many people that I came to know at MIT. First, I would like to express my sincere appreciation to Assistance Professor Nicholas C. Makris for his excellent guidance throughout my study. He has offered me a great opportunity to work on this thesis, which allowed me to explore the real-world experimental data, besides the otherwise theoretical course work. In addition, his understanding and generosity towards his students are greatly appreciated. Thank you, Prof. Makris!

During my course study, I have benefited from many professors in the OE department, along with the Teaching Assistants: Kyle, Wen Xu, and Yanwu. Fellow graduate students like Peter, Yuri, Jaiyong, Pierre, Vincent, and Brian are equally helpful when I need an advice. Friendships from Yi-San and Kevin will always remain in my memory of MIT. And, I must thank Jean, Sabina and Robert for all the administrative work that they have done for me. Furthermore, I need to acknowledge the collaboration and assistance from Ms Laurie Fialkowski (NRL-DC) who has kindly shared her knowledge with me.

I am also thankful to the Ministry of Defence (Singapore) and DSO National Laboratories for awarding me the scholarship to study here. In addition, I would not have come to MIT without the recommendations from Mr Philip Chan (DRD) and Mr Peh Kok Wah; as well as the valuable advice from Dr Goh Joo Thiam.

Like all other graduating students, I am most deeply grateful to my parents and family for their support and encouragement. Especially to my wife Fee Lip: many thanks for your love and care in these past one and half years. I will love you more each day. To the friends that we have acquainted here: we will definitely miss you all. Take care!

Dedicated to My wife,

Fee Lip

TABLE OF CONTENTS

1	**INTRODUCTION**		**11**
	1.1	Background	11
	1.2	Literature Review	13
	1.3	Motivations	14
	1.4	Objectives	15
	1.5	Thesis Outline	16
2	**DESIGN OF THE EXPERIMENTS**		**17**
	2.1	Experimental Geometry	17
	2.2	Environmental Parameters	21
	2.3	Configuration of Sonar Array Systems and Signals	23
		2.3.1 Cory's Transmitter	23
		2.3.2 Cory's Receiver	24
		2.3.3 Alliance's Receiver	25
	2.4	Data Acquisition and Recording	26
3	**DATA EXTRACTION AND PROCESSING**		**27**
	3.1	Off-line Data Processing System	27
	3.2	Procedure of Data Processing	28
	3.3	Calibration of Monostatic and Bistatic Data	31
4	**BI-AZIMUTHAL SCATTERING DISTRIBUTION OF B'**		**34**
	4.1	Geomorphology of The B' Abyssal Hill	34
	4.2	Wide-Area Bistatic Images	42
	4.3	High Resolution Images of B' Scarps	48
	4.4	High Resolution Reverberation Modeling & Scattering Strength Estimation	52
	4.5	Comparison between Measured and Modeled Reverberation	58
	4.6	Mean Bi-Azimuthal Scattering Strength	59

5 BI-AZIMUTHAL SCATTERING DISTRIBUTION OF C' 67

5.1 Geomorphology of The C' Inside Corner 67

5.2 Wide-Area Bistatic Images 72

5.3 Reverberation Modeling and Scattering Strength Estimation 77

5.4 Comparison between Measured and Modeled Reverberation 82

5.5 Mean Bi-Azimuthal Scattering Strength 86

6 COMPARISON OF THE BI-AZIMUTHAL SCATTERING DISTRIBUTIONS OF B' AND C' 93

6.1 Comparison of The Bi-Azimuthal Scattering Distributions of B' at Two Different Resolutions 93

6.2 Comparison between B' and C' Scattering Distributions 107

7 CONCLUSIONS 113

7.1 Summary 113

7.2 Conclusions 116

BIBLIOGRAPHY 118

LIST OF FIGURES

2-1 Tow-ship tracks overlain on the experimental area 19

2-2 A sketch of the sonar array systems deployed during the ARSRP93 experiments 20

2-3 A typical sound speed profile measured during the experiments 22

3-1 Travel time difference between the ray-trace and slant-range methods (S426) 30

3-2 Comparison of reverberation measured in segments S478 and S218 after compensated with their appropriate calibration constants 33

4-1 High resolution bathymetry and directional derivative charts computed on the East-Central face of B' ridge 36

4-2 Normalized auto-correlation function of the upper scarp's bathymetry 37

4-3 Sonar resolution footprint overlain on the upper scarps region for S435 38

4-4 Histograms illustrating the distributions of incident and scattered angles in a single sonar footprint for S435 transmission 39

4-5 Bistatic locations of the two research vessels, given in Eastings and Northings, during the LFM transmissions analyzed for the B' study 40

4-6 Azimuthal distribution of the source-receiver locations for the B' study 41

4-7 Wide-area images of monostatic and bistatic reverberation measured for 200-255 Hz LFM S478 45

4-8 Wide-area images of monostatic and bistatic reverberation measured for 200-255 Hz LFM S435 46

4-9 Wide-area images of monostatic and bistatic reverberation measured for 200-255 Hz LFM S528 47

4-10 High resolution charts of monostatic and bistatic measured and modeled reverberation for S435 over the upper and lower scarp contours 49

4-11 High resolution charts of monostatic and bistatic measured and modeled reverberation for S478 over the upper and lower scarp contours 50

4-12 High resolution charts of monostatic and bistatic measured and modeled reverberation for S528 over the upper and lower scarp contours 51

4-13 Range-depth map of broadband transmission loss incoherently averaged over 200-255 Hz frequency band using Parabolic Equation 57

4-14 Mean reverberation levels measured over the upper and lower scarps as a function of receiver azimuth Ω_r (high resolution B' study) 62
4-15 Mean reverberation levels modeled over the upper and lower scarps as a function of receiver azimuth Ω_r (high resolution B' study) 63
4-16 Mean surface projection over the upper and lower scarps as a function of receiver azimuth Ω_r (high resolution B' study) 64
4-17 Mean 2-way transmission loss over the upper and lower scarps as a function of receiver azimuth Ω_r (high resolution B' study) 65
4-18 MBASS estimated over the upper and lower scarps as a function of receiver azimuth Ω_r (high resolution B' study) 66
5-1 Bathymetry and directional derivative of the C' ridge plotted at 200-m resolution grid 69
5-2 Bistatic locations of the two research vessels, given in Eastings and Northings, during the LFM transmissions analyzed for the C' study 70
5-3 Azimuthal distribution of the source-receiver pairs for the C' study 71
5-4 Wide-area images of monostatic and bistatic reverberation measured for 200-255 Hz LFM S229 74
5-5 Wide-area images of monostatic and bistatic reverberation measured for 200-255 Hz LFM S874 75
5-6 Wide-area images of monostatic and bistatic reverberation measured for 200-255 Hz LFM S883 76
5-7 Surface projection and transmission loss charts computed over the SW corner of C' for S229 transmission 80
5-8 Transmission loss and modeled sum charts over the SW corner of C' for S874 and S236 transmission 81
5-9 The 200-m resolution charts of measured and modeled reverberation for S229 over the SW corner of C' 83
5-10 The 200-m resolution charts of measured and modeled reverberation for S874 over the SW corner of C' 84
5-11 The 200-m resolution charts of measured and modeled reverberation for S883 over the SW corner of C' 85

5-12 Mean measured and modeled reverberation over the C' scarp as a function of receiver azimuth Ω_r 89
5-13 Mean surface projection and mean 2-way transmission loss over the C' scarp as a function of receiver azimuth Ω_r 90
5-14 MBASS curve estimated over the C' scarp as a function of receiver azimuth Ω_r 91
5-15 Wide-area images of bistatic reverberation for 200-255 Hz LFM S236 and S239 92
6-1 Contours of the B' scarps designated for 5-m and 200-m resolution studies 96
6-2 Shaded relief plots for a section of the upper scarp at 5-m and 200-m resolutions 97
6-3 Comparison of the surface projection and two-way transmission loss charts at the B' scarps using 5-m and 200-m resolution bathymetry data 98
6-4 The 200-m resolution charts of monostatic and bistatic measured and modeled reverberation for S435 over the B' scarp contours 99
6-5 Mean reverberation levels measured over the upper and lower scarps as a function of receiver azimuth Ω_r (200-m resolution B' study) 102
6-6 Mean reverberation levels modeled over the upper and lower scarps as a function of receiver azimuth Ω_r (200-m resolution B' study) 103
6-7 Mean surface projection over the upper and lower scarps as a function of receiver azimuth Ω_r (200-m resolution B' study) 104
6-8 Mean 2-way transmission loss over the upper and lower scarps as a function of receiver azimuth Ω_r (200-m resolution B' study) 105
6-9 MBASS estimated over the upper and lower scarps as a function of receiver azimuth Ω_r (200-m resolution B' study) 106
6-10 Comparison of the B' and C' bathymetric features and their directional derivatives 109
6-11 Mean reverberation levels measured over the B' and C' scarps as a function of receiver azimuth Ω_r 110
6-12 Mean reverberation levels modeled over the B' and C' scarps as a function of receiver azimuth Ω_r 111
6-13 Mean bi-azimuthal scattering strengths estimated over the B' and C' scarps as a function of receiver azimuth Ω_r 112

LIST OF TABLES

2-1 Summary of the RV Cory's HLA characteristics 24

3-1 Summary of Gain and Equalizer settings for all the RV Alliance's data segments analyzed in this thesis 32

1 INTRODUCTION

1.1 BACKGROUND

The understanding of ocean bottom scattering is useful for active sonar in highly reverberant environments, and may also provide a practical method of remotely surveying seafloor geomorphology. It is well known that active sonar is often corrupted by echoes reflected or scattered from the seafloor features. These unwanted echoes are termed as *bottom reverberation* by the underwater acousticians. While a high level of ambient noise reduces the probability of target detection in a sonar system, bottom reverberation introduces multiple false targets which will confuse the sonar operator. To make matters worse, reverberation is strongly dependent upon the transmitted signal, and the received signal-to-reverberation ratio cannot be improved by purely increasing the transmission power. Therefore, if we can characterize the acoustic scattering from the ocean bottoms, it will allow active sonar to discriminate between a submerged target and the bottom reverberation.

By analogy, low-frequency sound can be used for remote sensing of the ocean bottoms, just as ultrasound is used in the medical imaging applications. Although sidescan sonar systems are commonly used to survey the ocean bottoms, low-frequency towed array systems provide a rapid mean of surveying the deep-ocean bottom over hundreds of kilometers in near real-time.[2] Furthermore, resolution of the towed-array imaging system is significantly better than the current available bathymetric maps of roughly 10-20 km resolution.[2,14] Hence, there is a real promise that the low-frequency towed-array system can be used to survey the world's remaining uncharted ocean bottoms.[2,14]

Until now, the phenomenon of acoustic scattering from rough ocean bottoms has not yet been fully understood. To improve this understanding of ocean bottom scattering, several experiments were conducted in July 1993 using a system of towed arrays at the Mid-Atlantic Ridges (MAR).[1,2,4,7,13-15,17-20] These experiments were carried out as parts of the Office of Naval Research's (ONR) Acoustic Reverberation Special Research Program (ARSRP).

In this thesis, we focus our analysis on the bistatic scattering data collected at the two selected ocean ridges, known as B' and C', during the ARSRP experiments in 1993. These bistatic experiments, designed by Prof. Makris, belonged to the Main Acoustics Experiment (MAE).[1,4] The main purpose of this study is to experimentally determine the scattering characteristics of these two ocean ridges because they span the two geologically distinct classes of ridges found in the MAR.

Two research vessels, RV Cory Chouest and RV Alliance, were used to obtain the monostatic and bistatic reverberation from B' and C'. The RV Cory deployed a vertical source array, operating in 200-255 Hz, and transmitted at roughly ½ Convergence Zone (CZ) range, or equivalent to 33 km, from each of these selected ridges. Concurrently, the RV Alliance maneuvered in a semi-circle about each ridge to cover a full sector of 180^0 bistatic azimuths. A horizontal line array was towed behind these two ships to collect the reverberation data, which were subsequently recorded onto 8 mm magnetic tapes, for post-trial analysis. Only transmissions from the Cory's source are analyzed here since it provides a higher source level and directivity than the Alliance's source.

Besides the acoustic data, a database of 200-m resolution bathymetry was collected over the entire experimental area. Another set of database, which contains high resolution bathymetry sampled at 5-m resolution, was also surveyed over the East-Central face of B'. These two sets of bathymetry data are used to support our analyses.

1.2 LITERATURE REVIEW

Long-range backscatter measured by towed-array has been found to sometimes correlate well with gross bathymetry trends by several investigators.[21-25] However, most of these studies have focused upon environments with isolated large-scale scattering features such as seamounts and coastal margins. The MAE advances beyond the previous studies since it was conducted in a more complex environment where reverberation were returned from small-scale geomorphology in the MAR.

The previous works of Makris et. al. are most directly relevant to the content of this thesis.[2,3,8] In the analysis of Acoustic Reconnaissance Cruise (ARC) and MAE experiments, Makris et. al. demonstrate that prominent sonar echoes are returned from extended ridges such as B' with steep scarps facing the source and receiver.[2,3] They have computed a measure of the seafloor's slope gradients called Directional Derivative (DD) by taking the dot product of the gradient vector of seafloor with a unit vector pointing in the direction of source or receiver location. Consequently, ridge surfaces facing the tow-ship are registered with positive DD, and surfaces facing away the ship are registered with negative DD. Their results show that a high percentage of the prominent returns are well charted to the positive DD regions of the experimental area.

In addition, Makris et. al. illustrate that prominent echo returns are highly dependent on the acoustic propagation paths. Strong returned echoes from B', C' and other prominent ridges are observed at ½ and n + ½ CZ ranges. They found reverberation modeled with a Parabolic Equation technique correlates well with measured reverberation. Their results have also indicated a characteristic difference between the monostatic and bistatic reverberation at the B' scarps for large bistatic angles. Small-scale anomalies, such as gullies and trellises, are found to introduce large variances in bistatic scattering characteristics of the scarps. A further study was then carried out to measure a bi-azimuthal scattering distribution of the two major scarps at B' using high resolution bathymetry data, which led to the first part of this thesis.

Although the reverberation data collected at B' have been studied extensively for the past few years, the bistatic reverberation data at C' have not yet been fully analyzed. Since B' and C' are known to span the two geologically distinct classes of ridges that are commonly found in the

Mid-Atlantic Ocean, which are respectively an inside corner and an outside corner, it is valuable to compare their bistatic scattering characteristics. By evaluating the scattering strengths of these two ridges, we may determine whether their scattering functions can be extrapolated to the other ocean ridges.

1.3 MOTIVATIONS

This thesis is divided into two parts. First, a study is carried out to measure the bi-azimuthal scattering distributions of the two major scarps at B' using 5-m high resolution bathymetry data.[14] The primary motivation is to establish an empirical bistatic scattering function for a typical abyssal hill B', also known as an outside corner, commonly found in the MAR. Since the towed-array system's theoretical resolution can be severely degraded by experimental uncertainties such as towed-array's orientation, sound-speed profile and statistical fluctuations in the scattered returns, which all are difficult to account a priori, this analysis also helps to experimentally assess the resolving power of a towed-array imaging system.

In the second part of this thesis, the same approach is used to measure the bi-azimuthal scattering distribution of C'. This study is motivated by the fact that the scattering functions for these two distinct classes of ocean ridges might be characterized according to their respective geomorphologic features, and a comparison will be helpful for identifying other uncharted ridges or bottom bathymetry in future surveys. However, due to unavailability of 5-m resolution bathymetry data at C', the bi-azimuthal scattering distributions of B' and C' are evaluated using 200-m resolution bathymetry data so as to compare their scattering characteristics appropriately. Consequently, the effects on the scattering strength estimation using the two different resolutions of bathymetry data at B' will also be investigated as a control on the C' results.

1.4 RESEARCH OBJECTIVES

The objectives of this research are:

1. To measure the bi-azimuthal scattering distributions of the two major scarps at B' with the supporting bathymetry data sampled at 5-m resolution;
2. To evaluate the effective resolving power of a low-frequency towed-array system in remotely imaging the seafloor geomorphology;
3. To investigate the effects on scattering strength estimation using the 5-m and 200-m resolutions of bathymetry data at B';
4. To compare the bistatic scattering characteristics of B' and C', which are two distinct classes of ocean ridges found in the MAR.

1.5 THESIS OUTLINE

In Chapter 2, the Main Acoustics Experiment and MAR environmental parameters are briefly explained to familiarize reader with the experiments. The sonar array systems and signals used are included to provide a background for the data acquisitions.

Chapter 3 outlines the procedure we adopted in the post-trial data processing. A computer utility system, previously developed by Prof. Makris and his group at NRL-DC, is used to extract raw data from the 8 mm magnetic tapes, and these data are subsequently converted into reverberation images on a two-dimensional Cartesian map projection. The calibration of the Alliance's towed-array data is also described.

Chapter 4 presents the bi-azimuthal scattering distributions of the two major scarps at B', primarily conducted by Makris and Fialkowski, using the supporting bathymetry data sampled at 5-m resolution. High resolution reverberation images are presented to demonstrate the correlation between the measured and modeled reverberation. Wide-area reverberation images are produced, using 200-m resolution bathymetry data, to check for any left-right ambiguity of the towed array that might be falsely charted onto B'. Detailed descriptions of our modeling and mean bi-azimuthal scattering strengths of the two B' scarps are also presented.

Chapter 5 discusses the bi-azimuthal scattering distribution of a major scarp at C' evaluated using 200-m resolution bathymetry data. The measured and modeled reverberation images are presented to illustrate their close agreements. A detailed analysis on the mean bi-azimuthal scattering strength of the C' scarp is carried out for comparison with the scattering strengths of the B' scarps in the subsequent chapter.

Chapter 6 first describes the bi-azimuthal scattering distributions of the two B' scarps evaluated at 200-m resolution. The effects on the scattering strength estimation of the B' scarps using 5-m and 200-m resolutions of bathymetry data are then discussed. Subsequently, the bistatic scattering characteristics of the B' and C' scarps, evaluated at 200-m resolution, are compared by examining their mean bi-azimuthal scattering strengths, mean measured and model reverberation as a function of receiver azimuth.

Finally, Chapter 7 contains an executive summary of this study and the conclusions drawn.

2 DESIGN OF THE EXPERIMENTS

2.1 EXPERIMENTAL GEOMETRY

Geographically, the experiments took place in 25.5^0 to 27.5^0 North latitude and 45^0 to 49^0 West longitude at the western flank of the Mid-Atlantic Ridges.[4] Nine experiments, which are known as *runs* by the ARSRP community, were conducted. In particular, runs 5a and 5b were conducted to measure the bistatic scattering at site B', while runs 3 and 8 were conducted to measure the bistatic scattering at site C'.

There is a narrow channel of deep bathymetry running roughly east-west across the center of the experimental area as shown in Figure 2-1. This channel, which is termed as *fracture zone* or *segment valley*, is caused by the separation of the local plate segment according to the theory of plate tectonics. At the western end, the segment valley is bounded by an *outside corner* ridge named B', and its eastern end bounded by an *inside corner* ridge named C'.[2,4] Consequently, the experiments conducted at the two sites are referred to as the *B'- C' corridor* experiments, which comprised roughly 90% of the Main Acoustics Experiment (MAE), designed by Prof. Makris.[1,2,4,14]

Two research vessels RV Cory Chouest (from NRL) and RV Alliance (from SACLANT) were deployed in these experiments, and their bistatic tow-ship tracks are overlain on the experimental area in Fig. 2-1.[2] During each experimental run, RV Cory and Alliance began at the edges of the star-shaped tracks with a slow cruising speed of 3 knots. While the RV Cory traced its straight-line path in the central star, the RV Alliance would zig-zag along the semi-circular arcs about B' and C'. A horizontal line array was towed behind each research vessel to measure the bottom reverberation in these two sites. To maximize the sonar cross-range resolution at B' and C', the towed array's broadside was directed towards each ridge throughout the measurements, while the ships' radiated noise was kept within each other's lowest resolution endfire beams to minimize mutual noise interference.

Subsequently, the two vessels returned to the central star location along a slightly deviated path which would allow reverberation data to be collected at different array headings. These

redundant data are useful for resolving any inherent left-right ambiguity of the line array by applying techniques such as *global inversion* as described by Makris in Ref. [9].

Previous study in Ref. [3] indicates that significant variations in reverberation can occur for a small change of measurement position due to bathymetry-induced variations in transmission loss (TL). The star-shaped ship tracks avoid the problem of comparing measurements with different TL by providing a point of global convergence over all the towed-array headings. Consequently, the star tracks with point of convergence placed at the eastern focal point (corresponding to runs 3 & 8) and western focal points (corresponding to runs 5a & 5b) are referred to as the *Easternstar* and *Westernstar* respectively.

Figure 2-2 illustrates the sonar array systems deployed by the two vessels in the ARSRP93 experiments. The sonar source, onboard RV Cory, consists of a ten-element vertical line array (VLA) deployed at 181 m water depth. Throughout the respective experimental runs, the Cory's VLA transmitted at roughly ½ CZ range of 33 km from each selected ridge, and quasi-monostatic reverberation returned from each ridge was received by the Cory's 128-element horizontal line array (HLA) at 170 m depth. The RV Alliance's HLA was towed at an average depth of 460 m for the bistatic receptions. Although the Alliance's source was also deployed in the experiments, we did not analyze any data associated with it in this thesis because its source strength and directivity was much lower than that of Cory.

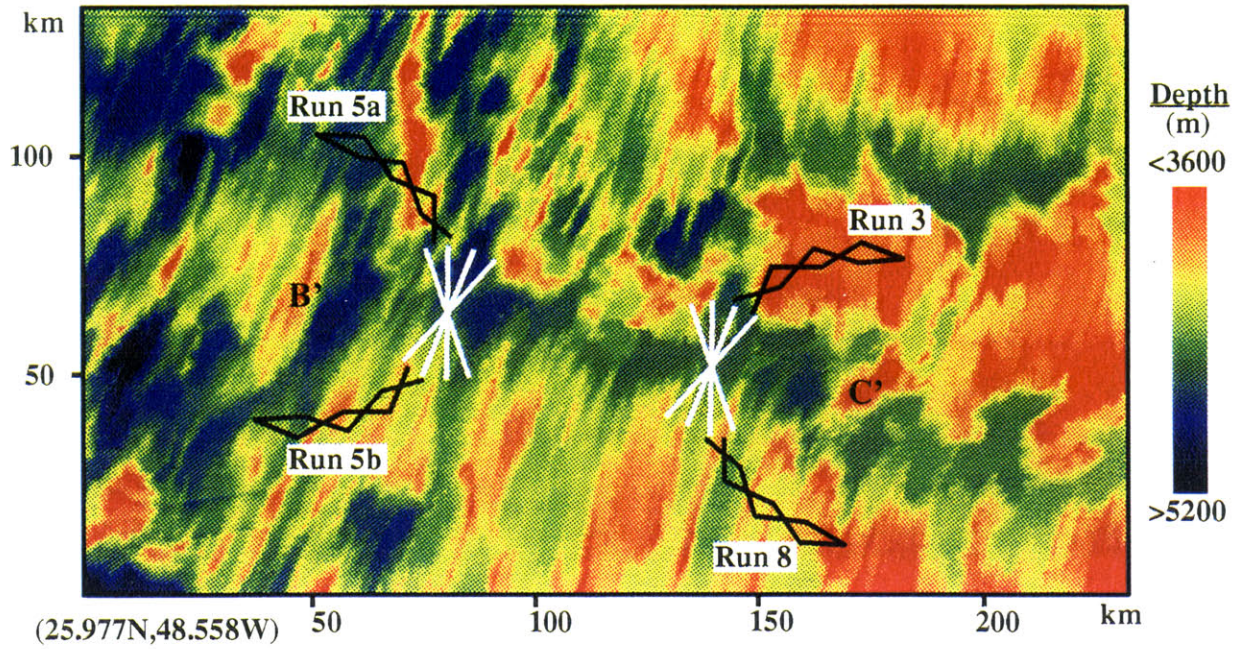

Figure 2–1: Tow–ship tracks overlain on the 200–m resolution bathymetry data of the experimental area. The B' and C' ridges are observed to be two prominent bottom features in the segment valley which runs roughly east–west across the bathymetry area. White color tracks denote the monostatic positions of RV Cory, while the black tracks indicate the bistatic positions of RV Alliance along the semi–circular arcs about B' and C'. Extracted from Ref. [2].

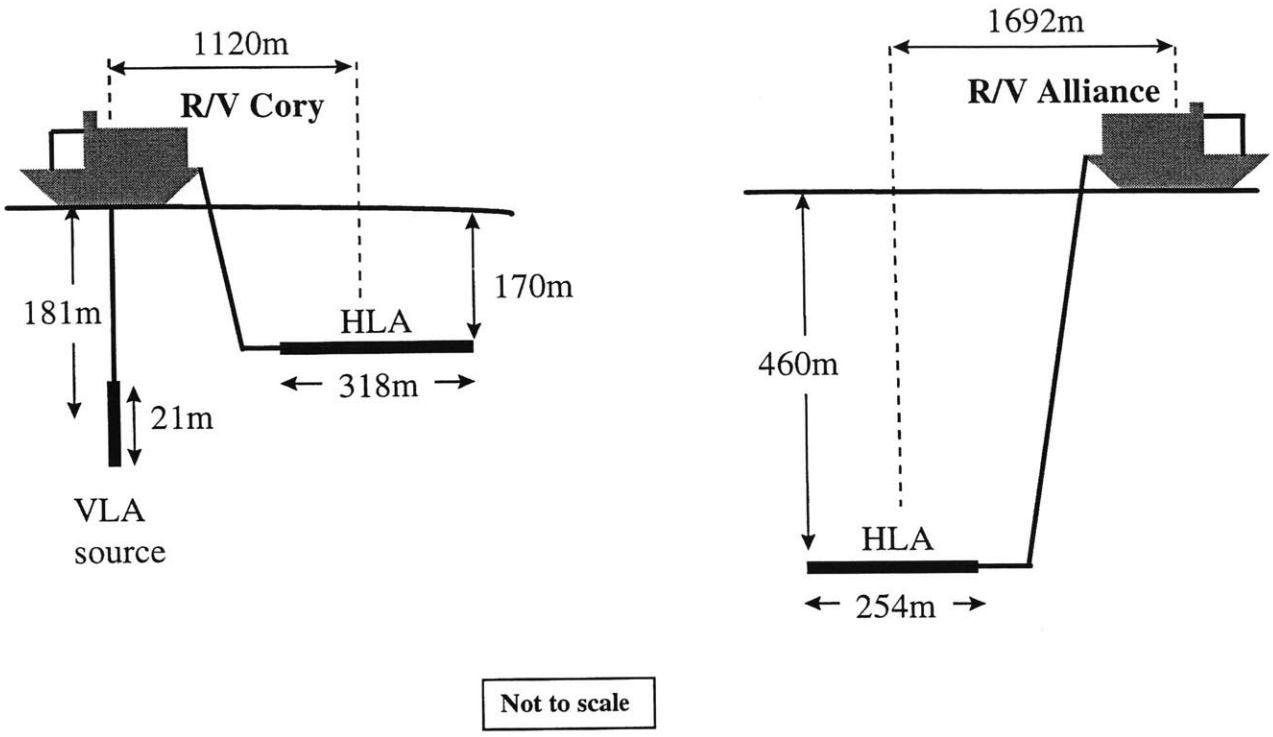

Figure 2-2: A sketch of the sonar array systems deployed by the two vessels in the ARSRP93 experiments. The sonar source, onboard RV Cory, consists of a ten-element vertical line array (VLA) deployed at 181 m water depth. Throughout the respective experimental runs, the Cory's VLA transmitted at roughly ½ CZ range of 33 km from each selected ridge, and quasi-monostatic reverberation returned from each ridge was received by the Cory's 128-element horizontal line array (HLA) at 170 m depth. The RV Alliance's HLA was towed at an average depth of 460 m for bistatic receptions. Although the Alliance's source was also deployed in the experiments, we did not analyze any data associated with it in this thesis because its source strength and directivity was much lower than that of Cory.

2.2 ENVIRONMENTAL PARAMETERS

The sound speed profiles measured by the RV Cory and Alliance during the experiments were plotted in Ref. [2], and they were found to follow classical Deep Sound Channel characteristics. A range-dependent acoustic modeling of the MAR ocean environment was previously carried out by Makris et. al. as described in Ref. [3]. In the model, the ocean bottom is assumed to comprise of sediment with uniform density of 1.5 g/cm^3, sound speed 1700 m/s, and attenuation 0.5 dB/λ. These parameters were then used with a wide-angle Parabolic Equation (PE) model to simulate the acoustic propagation paths in the water column. The modeling results show that the first sonar beam vertex occurs at the ½ CZ of approximately 33 km from the source, and the vertex bends at a water depth of 3,800 m to 4,500 m. For practical considerations, the sonar beam is expected to propagate through the water column for bottom bathymetry below 4,500 m, and will be scattered by bathymetry higher than 3,800 m.

In Fig. 2-1, B' and C' are observed to be two prominent seafloor features since their heights protrude well above the rest of segment valley. Moreover, these two ridges are much higher than the conjugate depth of 3,800 m, while most parts of the segment valley are well below the conjugate depth. Hence, B' and C' are expected to return the strongest backscatter where waterborne paths are available. For the same reason, long range sound propagation (>100 km) between B' and C' without any bottom interactions is also possible. Figure 2-3 illustrates a typical sound speed profile measured during the ARSRP93 experiments, whereby the conjugate depth of 3,800 m is derived by Snell's Law with the Cory's source at a depth of 181 m.

Weather conditions throughout this sea trial were considered calm and stable. Wave heights were less than 2 m and wind speeds were always less than 12 knots. Therefore, the surface reverberation is negligible, and the ambient noise level recorded in the data is low.

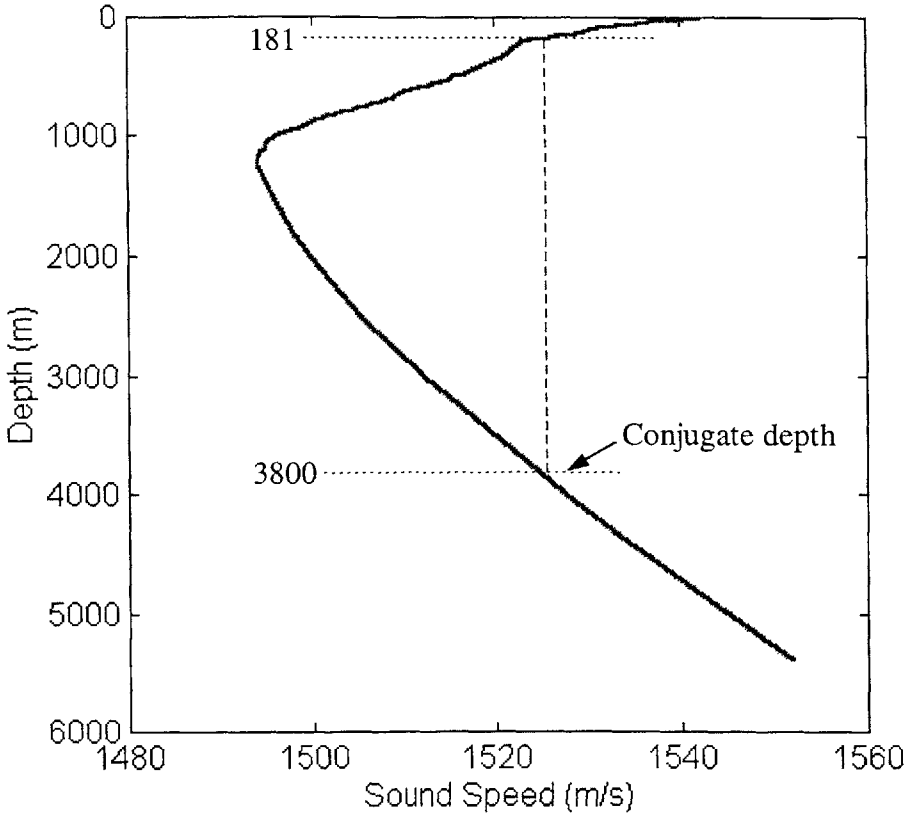

Figure 2-3: A typical sound speed profile measured in the ARSRP93 experiments. This profile is used during the off-line data processing to convert the beam-time data into beam-range data for the wide-area reverberation charts. A conjugate depth of 3,800 m is shown here, which corresponds to the Cory's source at 181 m depth deployed in the experiments.

2.3 SONAR ARRAY SYSTEMS AND SIGNALS

2.3.1 Cory's transmitter

The Cory's source consists of a ten-element vertical line array (VLA) with a source level measured at 229 dB re 1μPa @ 1m. The VLA has an operating frequency band of 200 to 280 Hz, with a 2.29 m spacing between each transducer element. It has a maximum source level at 200 Hz, and generally not less than 3 dB difference within the operating frequency band. During the B'- C' corridor experiments, the Cory's source was consistently deployed at a water depth of 181 m (with reference to the center of VLA), and maintained at almost 0^0 depression angle (i.e. horizontal transmission beam).

A low frequency active transmission subsystem (LTS) onboard the RV Cory controls the timing and transmission of the VLA source array. During each transmission cycle, the LTS performs a time delay beamforming with uniform shading to achieve a sonar beamwidth of approximately 10^0. Five sets of waveform, which consist of different coding schemes of LFM (Linear Frequency Modulated) and/or CW (Continuous Wave) pulses, were used in the sonar transmissions.

In this thesis, we only process the reverberation data associated to one of these waveforms called **WT93RP013**, which is a LFM pulse, with a 5-second duration sweeping across the frequency band of 200 to 255 Hz. During the experiments, this sonar transmission was activated in 12-minute cycles, and the corresponding reverberation data collected was assigned with a *data segment number* to identify each consecutive transmission cycle. Since the LFM pulse is always transmitted first in the cycle, the start time of LFM transmission coincides exactly to the segment time registered in the acquisition log.[4] Therefore, it is straight-forward, during the post-trial processing, to extract any particular LFM data segment from the 8 mm magnetic tapes by directly referring to the acquisition log.

Footnote: Most of the materials covered in this section are summarized from Ref. [4]

2.3.2 Cory's receiver

The RV Cory tows a horizontal line array (HLA) that records the reverberation data in its 128 uniformly spaced hydrophone groups of equal sensitivity. During the experiments, the Cory's HLA was towed at roughly 1.2 km (with reference to the array center) behind the ship at a water depth of 170 m. A summary of the HLA's characteristics is tabulated in Table 2-1.

Table 2-1: Summary of the RV Cory's HLA characteristics.

Center-to-center spacing of groups	2.5 m
Array aperture	317.5 m
Broadside beamwidth (Hamming shading) at 227.5 Hz	1.6^0
Endfire beamwidth (Hamming shading) at 227.5 Hz	23.2^0
Hydrophone Group sensitivity	-187.5 dB re 1v/μPa

The beamwidth resolution of the HLA, with aperture length L and steering angle θ, is given in Ref. [3] by the equation

$$\beta(\theta) \approx \mathrm{K}\frac{\lambda}{L}\frac{1}{\sin(\theta)},$$

where $\theta = \pi/2$ at broadside, and K depends on the weighting function used. During the ARSRP93 experiments, a Hamming function is used with K = 1.3. The array aperture length L is 317.5 m, and its wavelength λ is equal to 6.6 m for the LFM pulse of 227.5 Hz center frequency. Consequently, the broadside resolution is calculated to be $\beta(\pi/2) \approx 1.6^0$. When the towed array is steered towards the endfire direction, its main beam broadens and the beamwidth is expressed as

$$\beta(\theta) \approx 2.16\mathrm{K}\sqrt{\frac{\lambda}{L}}.$$

At the extreme azimuths $\theta = 0$ or π, the endfire resolution is found to be $\beta(0) = \beta(\pi) \approx 23.2^0$.

Prior to the experiment, dockside and at-sea calibrations were conducted for the HLA and its front-end sonar processing system. The calibration results indicated that 5 hydrophone groups were dead, and 13 hydrophone groups were 6 dB lower than the peak value for the MFA. As a result, the MFA beam pattern has its sidelobe structure altered from an ideal Hamming window. As shown by Makris in Ref. [20], the sidelobes of the "corrected" beam pattern stay fixed at roughly -30 dB below the main peak, instead of decreasing steadily towards the endfire directions. More importantly, the main-lobe structure is unaltered, and these calibrations confirmed the proper operation of the HLA and its front-end processing system.

2.3.3 Alliance's receiver

For our purposes, the receiving line array on the RV Alliance consists of 128 hydrophones spaced at 2.0 m apart. This line array was towed 1,692 m behind the Alliance at a depth of roughly 460 m throughout the ARSRP93 experiments.[4,7] The towed array data were digitized after the preampliers before being sent up the cable to the dry end processing system onboard the ship. A time domain beamformer, with Hanning weighting function, was used to generate 128 output beams from the acoustics data collected in a frequency band of 200 to 375 Hz. The array aperture length is 254 m long, and yields a beamwidth of $\beta(\pi/2) \approx 2.0^0$ at its broadside, which is comparable to the beamwidth of the Cory's receiver array.

2.4 DATA ACQUISITION AND STORAGE

Acoustic data from the Cory's receiving array were beamformed into 128 beams to cover a full 360^0 azimuthal sector in the 200-280 Hz frequency band. The 128 beams and 4 additional time series data were recorded onto 8 mm magnetic tapes (or known as Beam tapes, BTS) on a high-density Exabyte 8500 tape drive. A total of 96 beam tapes was used to record 1,090 data segments received by the Cory's towed array, and detailed records of these data segments are available in Ref. [4].

For the RV Alliance's receiving array, its 128 channels of beamformed data after digitization were band-shifted to the center frequency of 227.5 Hz. Subsequently, the band-shifted data was decimated, and stored as beam time series data (called "CBSHIFT" files) with 70 Hz bandwidth. These data are stored without any matched filtering, and each data segment is accompanied with a log file that includes the event name, receiver locations and the acquisition parameters such as the *Gain* and *Equalizer Bandwidth* settings. These parameter settings are essential for the calibration of raw data, which will be discussed in Section 3.3.

In this thesis, we are provided with the 8 mm magnetic tapes recorded by the RV Cory and Alliance. These data tapes are labeled with segment numbers and recording time that are cross-referenced with the acquisition log during the post-trial processing. The procedure of data extraction from these magnetic tapes will be discussed in the next chapter.

3 DATA EXTRACTION AND PROCESSING

An off-line data processing system, developed by Prof. Makris and his group while he was at NRL-DC, was used to process the ARSRP93 experimental data. Since the raw data was still kept in the 8 mm beam tapes, the following steps are required to process these data to be suitable for our analysis:

1. Download the selected data segments from 8 mm beam tapes into the off-line processor;
2. Perform FM matched filtering and data extraction on the selected data segments;
3. Compute the slant-range and ray-trace time maps for each data segment;
4. Bistatic mapping of the beam-time data to be displayed as reverberation image chart on a two-dimensional Cartesian map projection;
5. Compute the Directional Derivatives (DD) or Bistatic Horizontal Projection of the Bathymetry (BHBP) image charts using the supporting bathymetry data;
6. Overlay the reverberation images onto the DD or BHPB charts for visual correlation of prominent reverberation at B' or C'.

3.1 OFF-LINE DATA PROCESSING SYSTEM

The off-line computer system installed at MIT consists of a Silicon Graphics Indigo 4000 series workstation connected to a high density 8mm EXABYTE tape drive, optical disk drive, and Tektronix Color RGB printer. Prior to this study, several software programs on this system have already been developed by Prof. Makris and his former colleagues for processing the ARSRP93 data. Useful software utilities include the data retrieval programs (**SRPPLOT** and **SRP_PLOT**) for extracting the raw data from the 8 mm magnetic tapes. Bistatic mapping of the beam-time data is carried out by a program called **BISTATIC_MAP**, and a graphics software called **ARRAYPLANE** is used for displaying the reverberation and BHBP charts.

3.2 PROCEDURE OF DATA PROCESSING

Monostatic reverberation data collected by the RV Cory is first retrieved from the 8 mm beam tapes by running a program called **SRPPLOT**. Input parameters into the program include the start date and time, start beam, number of beams, and number of seconds to extract from the beam tapes. Based on the user-requested time, this program forwards the archive tape to the relevant segment, and converts the data from compressed 16-bit to IEEE 16-bit format. Subsequently, an FM matched filtering is performed on the raw data for signal-to-noise ratio improvement. On the other hand, bistatic reverberation data collected by the RV Alliance is retrieved from the beam tapes by first downloading the selected data segments into the SGI workstation. A program called **SRP_SACLANT** is then used to extract the beam-time data with FM matched filtering.

Next, the beam-time data is transformed to a Universal Transverse Mercator (UTM) coordinates by assigning the data to each point on a two-dimensional Cartesian grid system. A program from United States Geological Survey (USGS) is used to convert the bearing (in decimal degrees) into the UTM projection within an accuracy of 1 m.[2,4] Specifically, a program called **BISTATIC_MAP** has been written to convert the beam time data into reverberation image charts. A linear conversion from travel time to range was used during the ARC analysis by multiplying the beam-time data with a mean sound speed.[3] In this thesis, we use a *slant-range* conversion method to compute the travel time for the wide-area reverberation charts. This method offers an advantage of quick and easy computation to check for any inherent left-right ambiguity of the towed-array that might be falsely charted onto B' and C'. On the other hand, a range-dependent ray tracing method is used to achieve a more accurate range conversion for the high resolution reverberation charts.

In the slant-range method, distance between the source's location and the known seafloor bathymetry (refers to as the slanted range) is first computed by measuring their horizontal range and depth differences. A mean sound speed between the source's depth and bathymetry is calculated, and the travel time is obtained by dividing the slanted range with the mean sound speed. Generally, the travel time difference between the ray-trace and slant-range methods is found to be less than 0.15 seconds at ½ CZ range. For an illustration, the travel time difference

measured at the Cory's source and receiver for segment S426 are shown in Figure 3-1 (Data provided by Makris). A compound effect of the two-way range error is found to be ~ 230 m or roughly one pixel difference in the wide-area charts, which is still tolerable for the purpose of checking the left-right ambiguity errors. However, ray tracing is necessary in the high resolution study to achieve the required range accuracy, as will be discussed in Chapter 4.

To set up a consistent reference frame for all the reverberation charts in our study, a South-West (SW) corner of the experimental area is fixed as the origin (0,0) of the 2-dimensional horizontal grid system. For each wide-area chart of 1350 x 1350 pixels, the SW corner is set at (25.18309N, 48.57137W), while the SW corner of the 5-m high resolution chart is set at (26.54676N, 48.11122W). Each pixel increment of these charts corresponds to the resolution of bathymetry data used. Hence, the 5-m high resolution image, which has a total of 1600 x 1800 pixels, contains the 8 x 9 km area that was surveyed at the East-Central of B' ridge.

The output from bistatic mapping is stored in a binary file format. A program called **ARRAYPLANE** is then used to display this binary data file as a 3-D (x,y and color) image, whereby the reverberation levels can be displayed with a variety of color schemes. This graphics program also allows the reverberation contours to be overlain on the supporting bathymetry or DD/BHBP images. From which, we can visually correlate prominent echo returns with the bathymetry or prominent seafloor features.

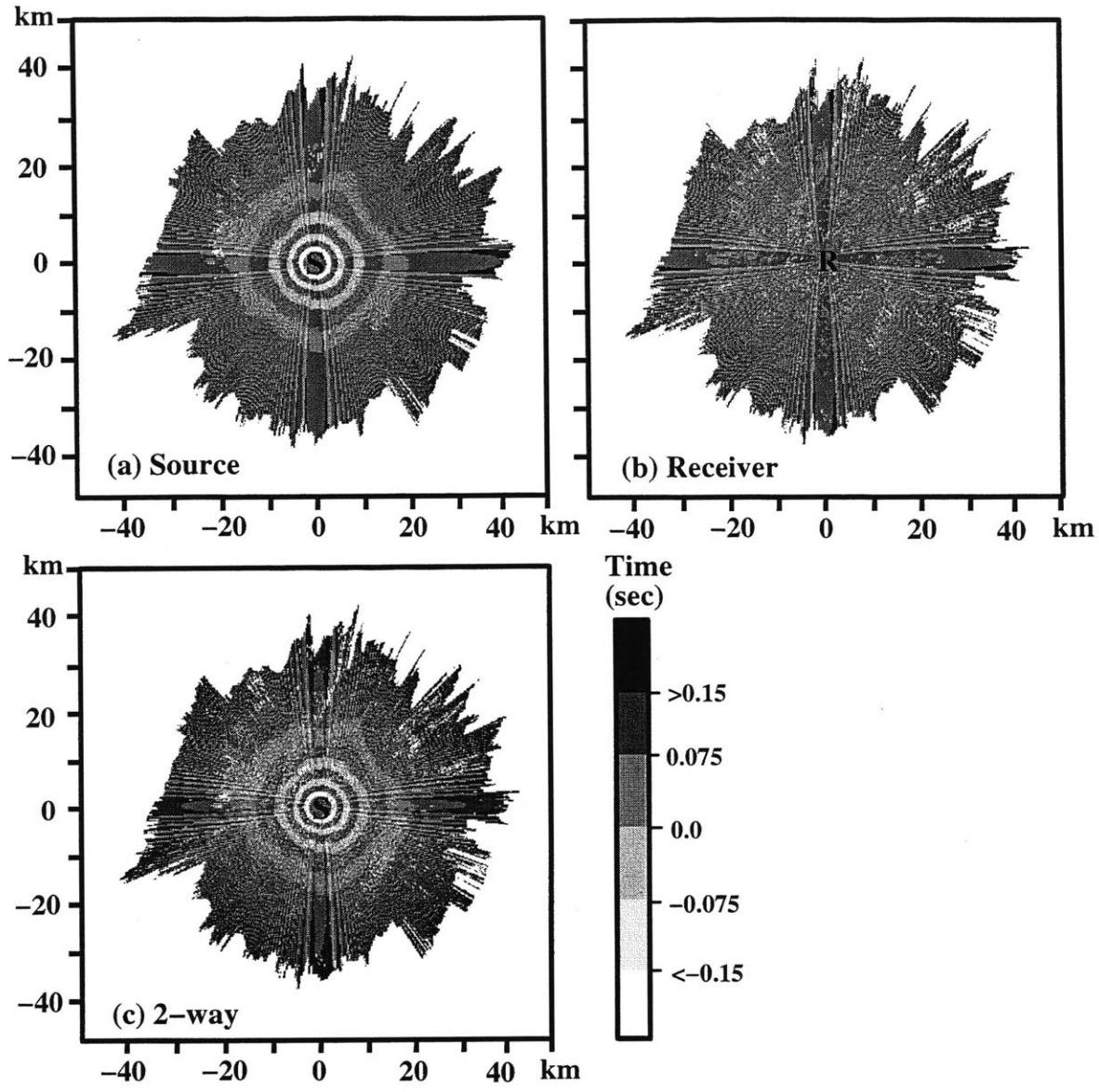

Figure 3–1: Travel time difference between the ray–trace and slant–range methods for S426 transmission. (a) The travel time difference measured from the Cory's source to bottom bathymetry within 1/2 CZ radius. (b) The travel time difference measured from the Cory's receiver array, and (c) The combined effect of 2–way time difference, which indicates that the time difference is within 0.15 seconds at 1/2 CZ range. Data provided by Makris.

3.3 CALIBRATION OF MONOSTATIC AND BISTATIC DATA

Calibration constant needed for the Cory's processed LFM data was found to be *-49 dB* from the previous study,[2] i.e. 49 dB is subtracted from the raw data to obtain the actual reverberation level in dB re 1 μPa. On the other hand, the calibration of the Alliance's raw data depends on 2 main parameters: the Equalizer Bandwidth *fl*, and Gain *G* settings that were configured during the data acquisitions. These settings were recorded in a log file accompanied in each data segment, and they were cross referenced during the post-trial processing to calibrate the reverberation data appropriately.

Sensitivity of the Alliance's towed array can be calculated via the equation [7]

$$Sensitivity = -151 + 10.\log\left[\frac{(\frac{f}{106})^2}{1+(\frac{f}{106})^2}\right] + 10.\log\left[\frac{(\frac{f}{fl})^2}{1+(\frac{f}{fl})^2}\right] + G,$$

where *f* denotes the center frequency of 227.5 Hz, and the calibration constant is expressed as

$$Calibration = -Sensivity + 20.\log\left(\frac{10\sqrt{2}}{32768}\right) - 49.$$

For most of the data segments collected at B', the settings correspond to G = 30 dB and fl = 1000 Hz, and the calibration constant is found to be approximately *+19 dB*. In other words, the RV Alliance's raw data is increased by 19 dB to produce a calibrated reverberation level in dB re 1 μPa comparable to that of the RV Cory. However, there is an exceptional case in segment S478, whereby the gain setting G = 42 dB, and the calibration constant is calculated to be +7 dB instead.

Figure 3-2 shows a comparison between the monostatic and bistatic reverberation measured in two data segments, S478 and S218, after compensated with their respective calibration constants. Since these two data segments were collected at the start of each run for measurements over B' and C' respectively, the RV Cory and Alliance were relatively close to each other (~1.6 km for S478 and ~2.1 km for S218). Therefore, we expect prominent echoes returned from B' and C' to be similar in these monostatic and bistatic receptions. Indeed, the reverberation charts confirm that their reverberation levels are almost identical in each segment.

Some minor differences occurred in the reverberation image patterns due to their differing array headings.

The Gain and Equalizer settings for all the RV Alliance's data segments analyzed in this thesis are tabulated in Table 4-1. The appropriate calibration constants calculated for these data segments are provided here for any future reference.

Table 3-1: Summary of Gain and Equalizer settings for all the RV Alliance's data segments analyzed in this thesis.

SEGMENT NUMBER	**GAIN SETTING, *G* (dB)**	**EQUALIZER BANDWIDTH, *fl* (Hz)**	**CALIBRATION CONSTANT (dB)**
S420 ~ 534 (except S478)	30	1000	19
S478	42	1000	7
S218 ~ 241	24	1000	25
S247 ~ 251	36	1000	13
S257 ~ 271	30	1000	19
S874 ~ 925	30	300	10

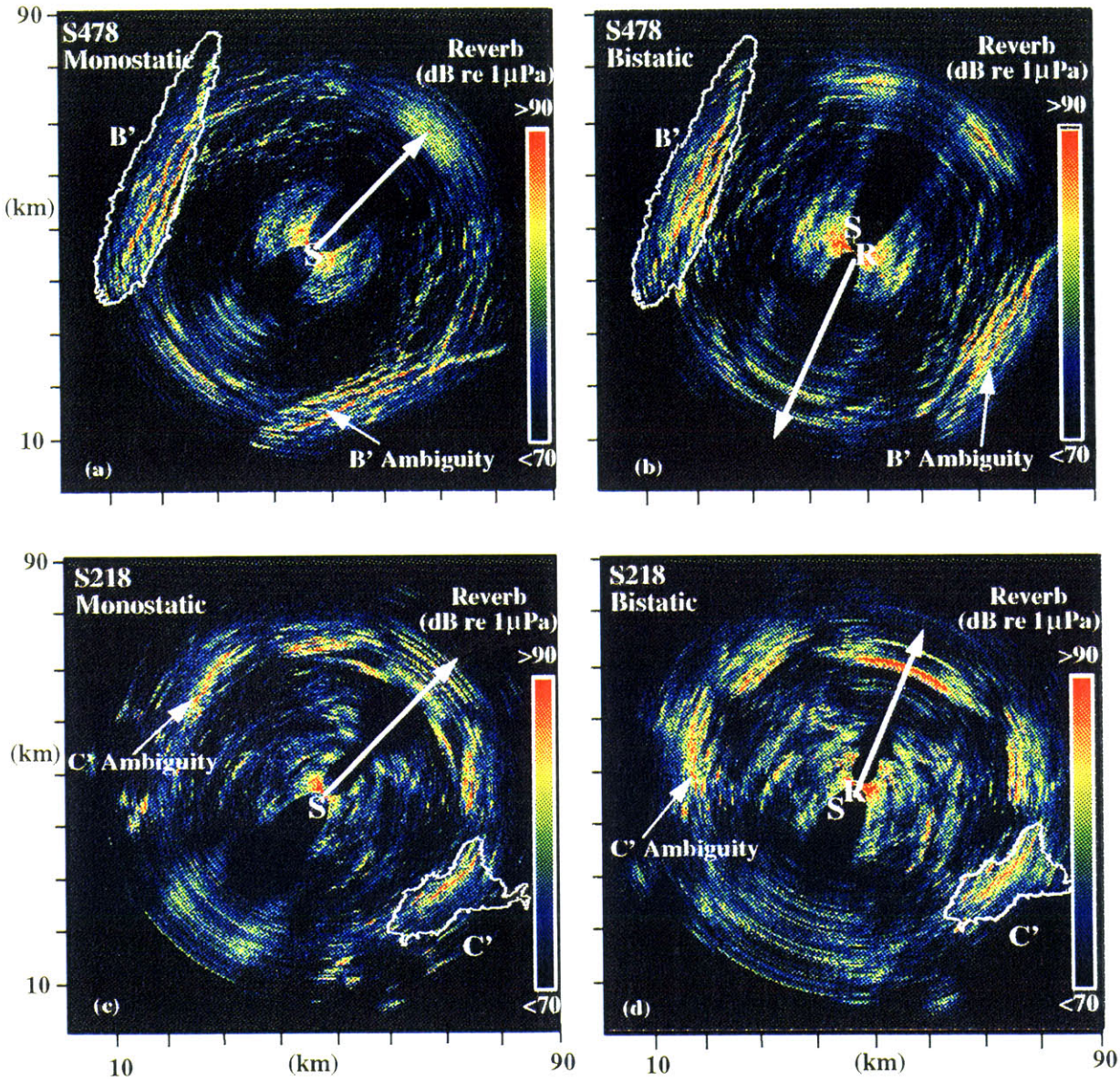

Figure 3–2: Reverberation levels measured in segments S478 and S218 after compensated with the appropriate calibration constants. (a) S478 monostatic reverberation. (b) S478 bistatic reverberation. (c) S218 monostatic reverberation. (d) S218 bistatic reverberation. Since the separations between the RV Cory and Alliance are relatively short (~1.6 km for S478 and ~2.1 km for S218), the reverberation received by both receivers are of similar strengths as expected. Some minor differences are observed in the reverberation image patterns because of the differing array headings.

4 BI-AZIMUTHAL SCATTERING DISTRIBUTION OF B'

A complete analysis of the bi-azimuthal scattering distribution of the B' abyssal hill is discussed by Makris et. al. in Ref. [14]. In this chapter, we only present the major findings of the B' analysis that are directly relevant to the comparison of results analyzed at C'. Particularly, the analysis and figures of Sections 4-3 to 4-6 are mostly developed by Makris and Fialkowski. These sections are essential to the thesis, however, since they will be expanded upon in later chapters.

4.1 GEOMORPHOLOGY OF THE B' ABYSSAL HILL

The B' ridge is a typical, highly lineated abyssal hill which is commonly found in the world's ocean bottoms. It is approximately 40 km long, with two narrow scarps that run parallel to the ridge axis 21^0 from true North. These two steep, unsedimented cliffs are approximately 100 m in height, and are typically inclined at 50^0 to 90^0. Moreover, both these two scarps are known to contain some small-scale anomalies such as canyons (~100-200 m wide) and gullies (~50 m wide). In between these two scarps, there is a relatively flat plateau region that projects little surface area towards the source and receiving arrays at low grazing angles.

The high resolution bathymetry surveyed at the East-Central face of B' ridge and its corresponding directional derivative (DD) are shown in Figures 4-1 (a) and (b) respectively. While gross geomorphologic features are observable in the 5-m resolution bathymetry chart, their fine details are better cast in the DD chart. As shown in Fig. 4-1 (b), the regions of positive DD indicate steep slope gradients at the two scarps facing the source and receiver locations. The two scarps are overlain with DD contours exceeding 0.5, corresponding to slope gradients of roughly 26.6^0 and greater. Throughout this study, these same contours are used to designate the upper and lower scarps.

The normalized auto-correlation function of the upper scarp's bathymetry is computed as shown in Figure 4-2, which illustrates the along and cross-scarp bathymetry scales (e-folding lengths) of 150 m and 50 m respectively. This result is consistent with the visual inspection of the

canyon and gully dimensions. Figure 4-3 shows a sonar footprint overlain onto the upper scarp area for S435 transmission. Typically, the sonar footprint of the two towed-array systems covers an areal resolution of 50 m x 1000 m at the ½ CZ range. In monostatic reception, as observed in Fig. 4-3(a), one resolution footprint may cover up to 5 or 6 canyons when its cross-range axis is parallel to the upper scarp's. In bistatic reception, the cross-range axis of the sonar footprint tends to skew across the scarp axis as the receiver moves to a larger bistatic angle. Frequently, the resolution footprint crosses both the scarp and plateau areas as shown in Fig. 4-3(b).

Ray-tracing is carried out to compute the incident and scattered angles at the scarp for S435 transmission. The distributions of incident and scattered angles in a single sonar footprint are then computed via histograms as shown in Figure 4-4. These histograms illustrate that the incident and scattered angles are widely distributed within the resolution footprint for both monostatic and bistatic receptions. Consequently, one can deduce that the surfaces resolved by sonar resolution footprint are not even approximately planar, and therefore cannot be represented by an unique surface normal. In fact, the towed-array system tends to integrate or smear out the scattering from roughly five canyons within the resolution footprint when its cross-range axis parallels to the scarp axes, as observed in the monostatic receptions.

A total of 20 monostatic and 18 bistatic segments has been processed to measure the bi-azimuthal scattering distribution of B'. The locations of the two research vessels for these data segments are distributed in a semi-circle of roughly 33 km centered at the high resolution area, as shown in Figure 4-5. The boxed alphabets denote the RV Cory's locations, while the corresponding unboxed alphabets denote the RV Alliance's locations for the same transmission. The black box in this figure indicates the 8 x 9 km area of 5-m resolution bathymetry data surveyed for this study, within which the two diagonal lines indicate the upper and lower scarps at B'. The azimuthal distribution of the source-receiver location pairs is plotted in Figure 4-6. Azimuth is measured counterclockwise by a vector that originates from the center of each scarp in the high resolution region, and points normal to its axis in a southeasterly direction. While the source azimuths Ω_i fall within $|\Omega_i| < 30^0$, the receiver azimuths Ω_r cover a full $+/-90^0$ sector, yielding a complete suite of bistatic scattering measurements at B'.

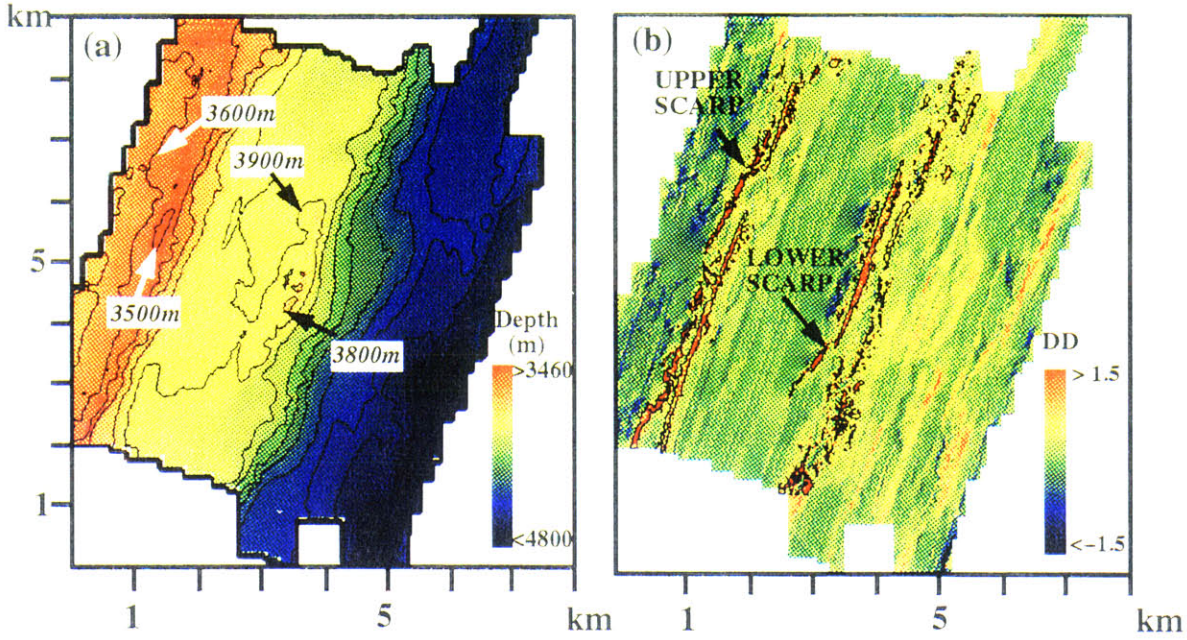

Figure 4–1: (a) High resolution bathymetry surveyed at the East–Central face of B' ridge. (b) The Directional Derivative (DD), normal to the B' axis, computed over the East–Central face of B' ridge with high resolution bathymetry data. The contour segments in (b) indicate the steep elevations on the upper and lower scarps with DD > 0.5, corresponding to slope gradients > 26.6^0. Figure by Makris & Fialkowski.

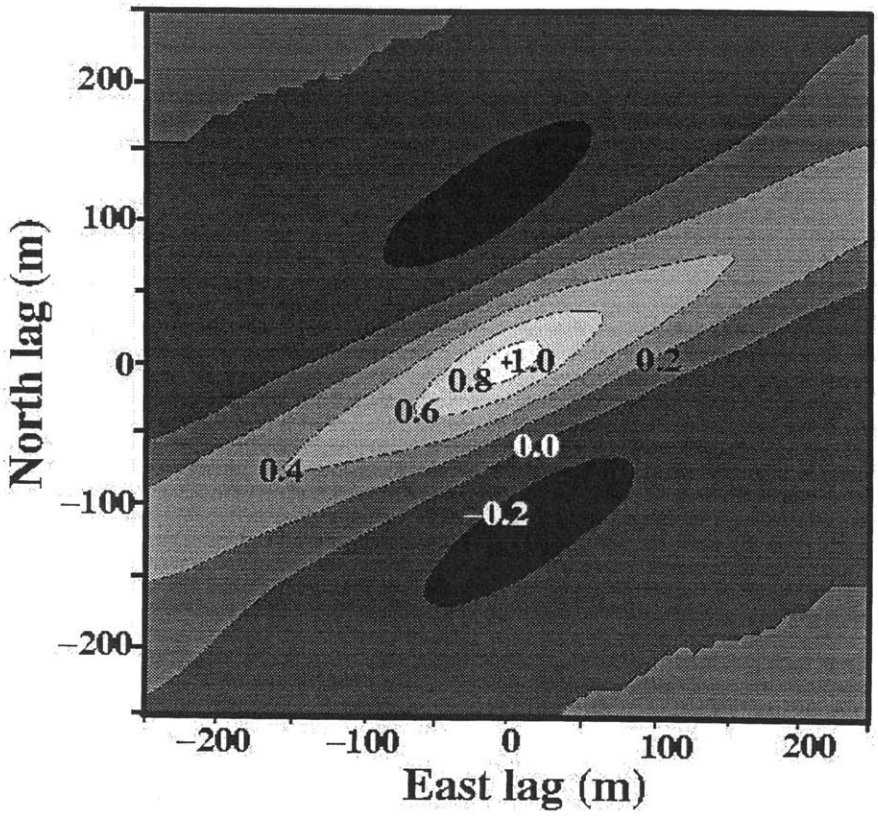

Figure 4-2: The normalized auto-correlation function of the upper scarp's bathymetry, given in North and East lags. It is computed to illustrate the along and cross-scarp bathymetry scales (e-folding lengths) of 150 m and 50 m respectively.

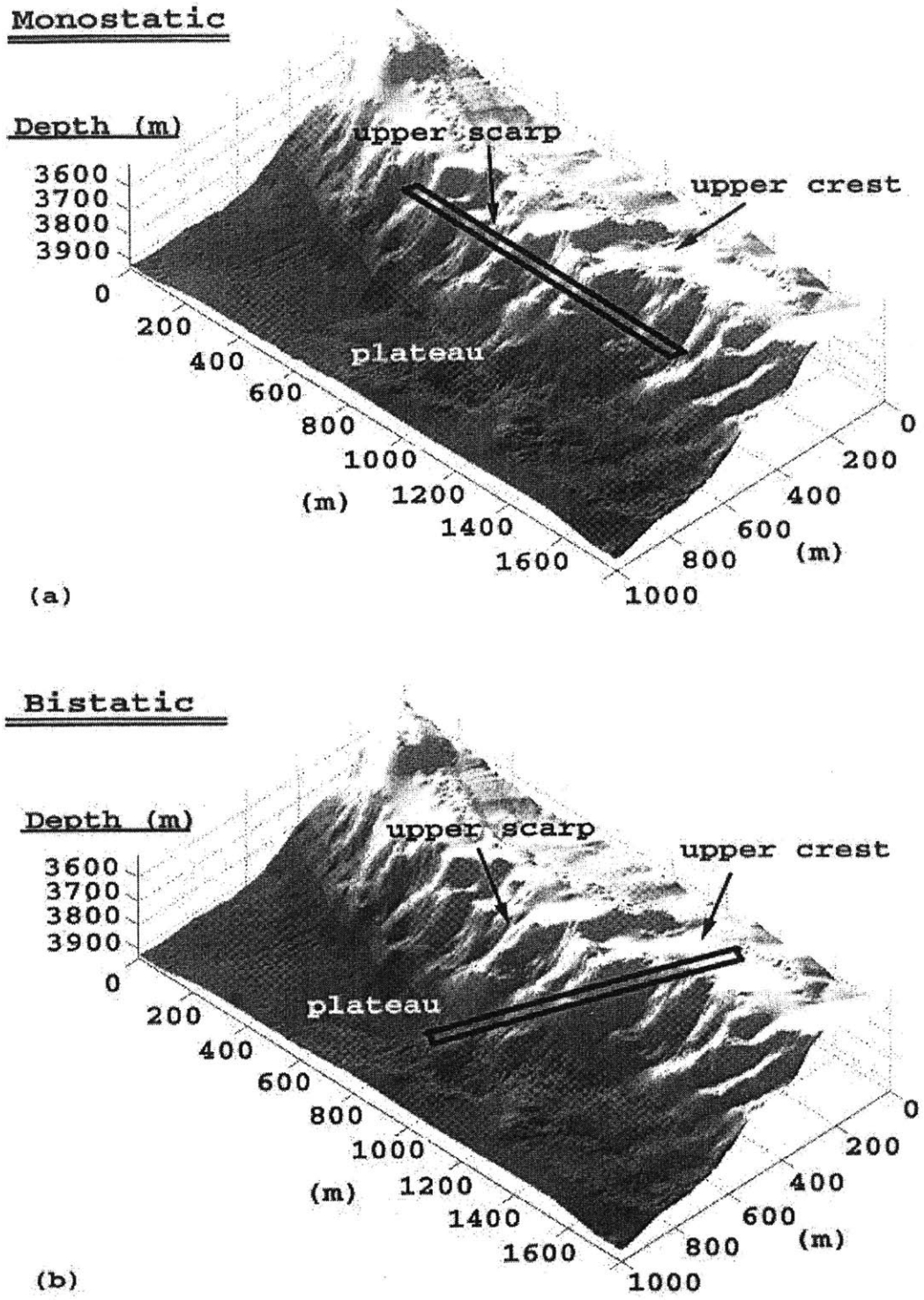

Figure 4-3: Sonar resolution footprint overlain on the upper scarp region for S435 transmission. (a) For monostatic reception, the footprint cross-range axis is parallel to the scarp axis; while (b) in bistatic reception, the cross-range axis is often skew across the scarp axis.

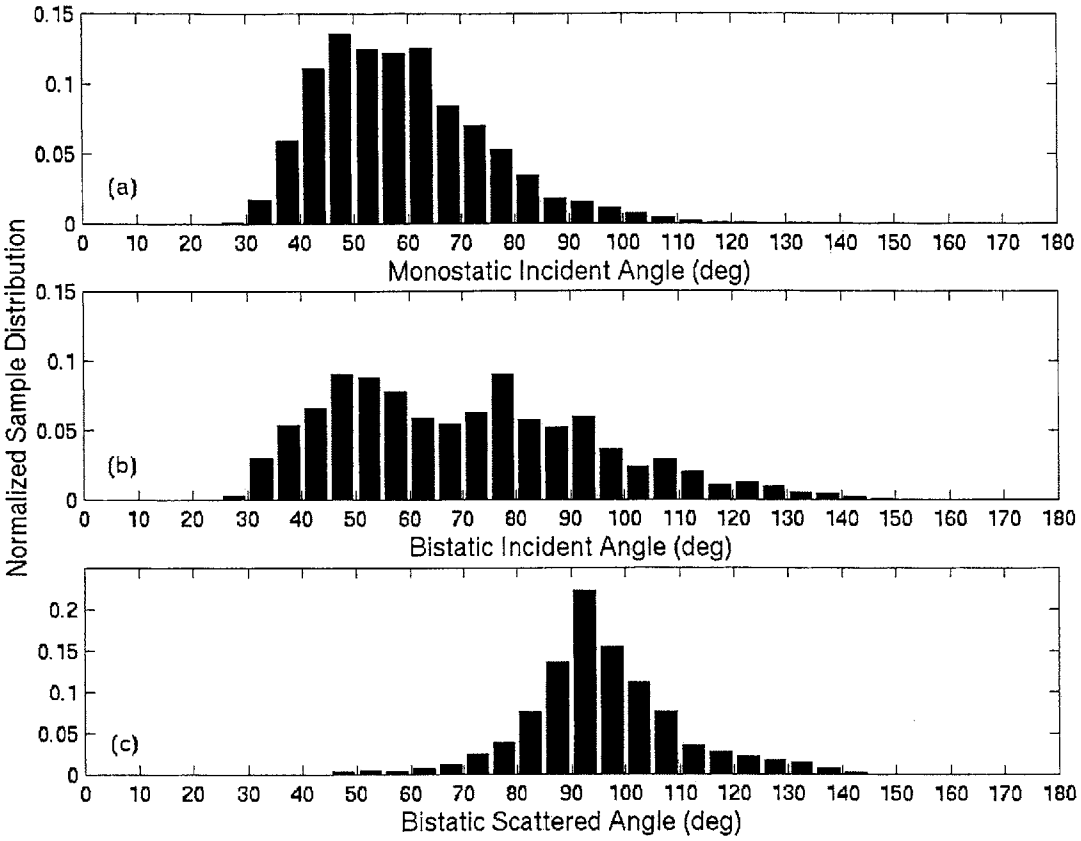

Figure 4-4: Histograms to illustrate the distributions of incident and scattered angles in a single sonar footprint for S435 transmission as shown in Fig. 4-3. (a) Monostatic incident angles within the sonar footprint resolution for S435 transmission. (b) and (c) show the bistatic incident and scattered angles within the sonar footprint resolution for the same transmission.

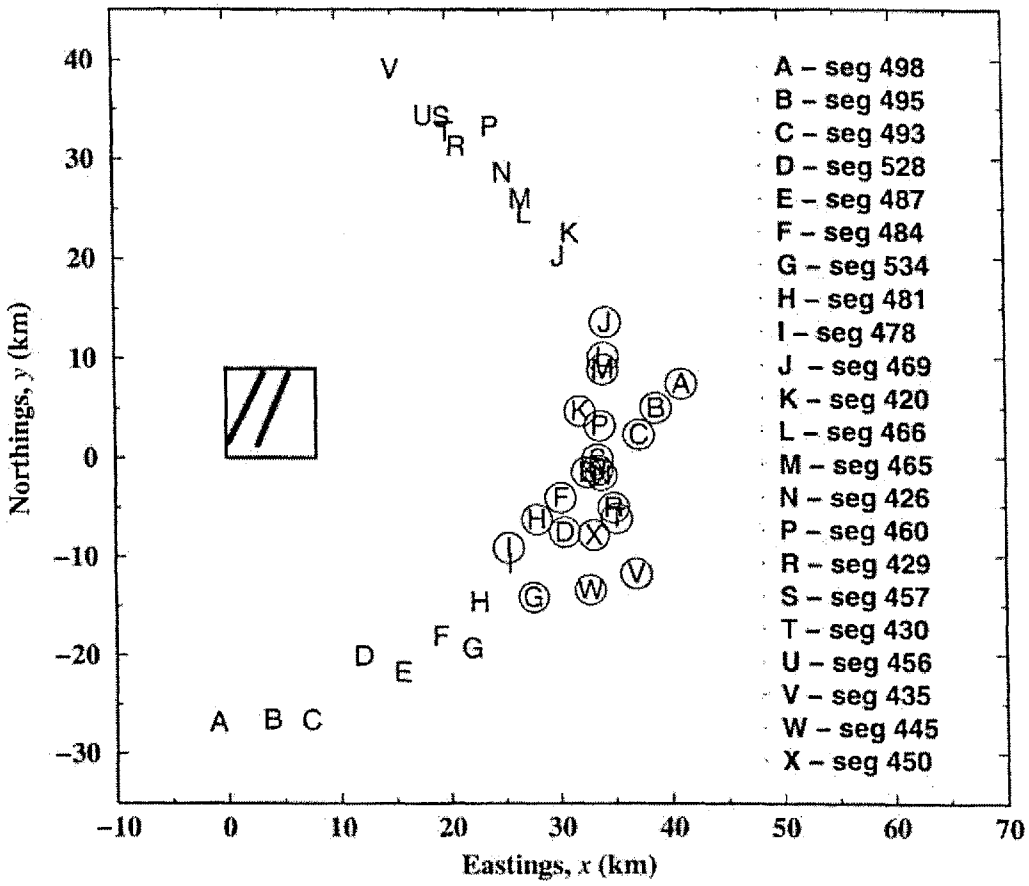

Figure 4-5: Bistatic locations of the two research vessels during the LFM transmissions analyzed in this study, given in Eastings and Northings. These locations are distributed in a semi-circle centered at the high resolution region shown by the central box, within which the two diagonal lines indicate the upper and lower scarps. Figure by Makris & Fialkowski.

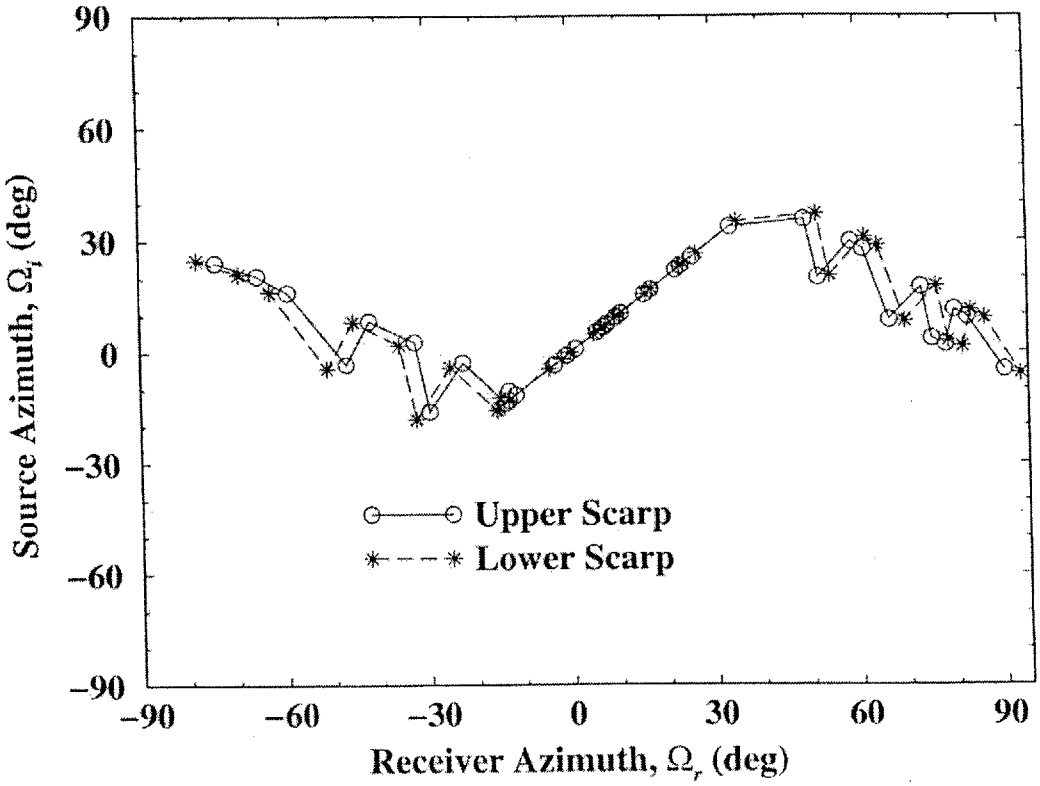

Figure 4-6: Azimuthal distribution of the source-receiver location pairs for the B' study. While the source azimuths Ω_i fall within $|\Omega_i| < 30^0$, the receiver azimuths Ω_r cover a full 180^0 sector, yielding a complete suite of bistatic scattering measurements at B'. Figure by Makris & Fialkowski.

4.2 WIDE-AREA BISTATIC IMAGES

Figure 4-7 shows the wide-area reverberation charts obtained from the monostatic and bistatic receptions for segment S478. On the left, the two charts display the calibrated reverberation data collected by the RV Cory and Alliance. Strong lineated echoes, which correspond to returns from the two steep scarps at B', are found at the receiver array's broadside. The left-right ambiguity, due to the conical beam pattern of horizontal line array, mirrors the echoes at B' onto the right-hand plane. Reverberation returned to the forward and rear sectors of the receiving array are spread spatially as a result of its broadening beamwidth towards the endfire directions.

On the right, the two charts show prominent reverberation contours, after threshold above 80 dB re 1 μPa, overlain on the Bistatic Horizontal Projection of the Bathymetry (BHPB). The Horizontal Projection of the Bathymetry towards the Source (HPBS) is defined as the inner product of the local seafloor normal vector and a unit vector towards the horizontal position of the source. The BHPB is computed by multiplying the HPBS with the HPBR or Horizontal Projection of the Bathymetry towards the Receiver which is defined similarly to the HPBS. Note that the product of a negative HPBS and a negative HBPR is always plotted as a negative BHBP to indicate the shadowed slope gradients of seafloor bathymetry. Moreover, all the wide-area BHBP charts are plotted using the supporting 200-m resolution bathymetry data.

As revealed by Fig. 4-7 (b) & (d), there are two distinct lines of positive BHPB, which coincide to the upper and lower scarps, running parallel to the B' ridge axis. The black box at the East-Central of B' indicates the 8 x 9 km area of high resolution bathymetry data surveyed. It can be seen in these charts that prominent echoes correlate remarkably well with the positive BHPB registered at the upper and lower scarps. This observation is consistent with the previous analysis of the CW transmissions as described in Ref. [2].

While the bistatic and monostatic reverberation charts for S478 are shown with similar behavior in Figure 4-7, it appears to be true only when the bistatic separation angle is small. When the bistatic angle is increased, such as segments S435 and S528 in Figures 4-8 and 4-9 respectively, the bistatic reverberation charts differ significantly from the monostatic ones. In particular, the circular symmetry pattern observed in the monostatic reverberation charts is

missing in these bistatic charts. This difference can be explained by examining the left-right ambiguity of the towed array in bistatic sonar reception.

For simple range-independent propagation and a flat bottom environment, the range ambiguity of bistatic sonar reception is mapped onto an elliptical contour with the source and receiver positions as its foci. The major axis of the ellipse is given as the sum of source-to-scatterer range and scatterer-to-receiver range. Since the Cory's receiver array is towed roughly 1.2 km behind the sonar source, the source-receiver separation is relatively short as compared to the stand-off range of 33 km from B'. Geometry teaches us that an ellipse becomes a circle if the separation between its two foci approaches zero. Therefore, the range ambiguity appears with a circular symmetry in all the monostatic reverberation charts because of the comparatively short source-receiver separation. On the other hand, the separation between the Alliance's receiving array and Cory's source may be beyond tens of kilometers during the bistatic measurements (eg. segment S435). Hence, the range ambiguity follows an elliptical pattern which is characteristics of bistatic sonar reception.

In some bistatic receptions, such as S478, the bistatic reverberation displays a well-balanced symmetry when the receiver array's heading is in line with the source-receiver axis (i.e. the major axis of the bistatic ellipse). However, such *balanced* symmetry is often absent in the bistatic charts when the receiver's array heading is tilted considerably from the source-receiver axis, such as S435 and S528. In these segments, the B' ambiguity, which is mirrored about the receiver's array axis, tends to fall at a much shorter range than the true return to preserve the two-way travel time.

Moreover, the B' ambiguity is compressed into a smaller spatial area than the true return to conform with the cross-range resolution of sonar footprint along the elliptical contour. This leads to a distortion in the bistatic reverberation image. Conversely, any false ambiguity charted onto the B' scarps will be magnified spatially. Nevertheless, the ARSRP93 experiments have been designed to eliminate the contamination of false ambiguity at B' by exploiting the natural geomorphology of the experimental areas. Hence, many of the data segments collected are not affected by the left-right ambiguity errors at B'.

While the BHPB patterns of B' are remarkably long and linear in S435 monostatic reception, they become speckle-like along the scarp areas in the bistatic reception [Fig. 4-8(d)]. In fact, this speckled pattern is caused by the projected areas of small-scale features, such as canyons and gullies, along the scarps when the Alliance's receiver is moved to the northern extreme of B'. Similarly, prominent echoes charted onto B' are also observed to follow a speckle-like pattern of elliptical arcs across the two scarps.

Although the BHBP model is capable of predicting the general characteristics of measured reverberation, the two-way transmission loss due to acoustics propagation in the water column has not been included in these BHBP charts. A complete model, which takes into account of the two-way transmission loss and surface projection of the bathymetry at 5-m resolution, is subsequently conducted and will be discussed in the next section.

Since the high resolution image only covers the 8 x 9 km area at B', it does not provide a full pictorial view to examine the left-right ambiguity of the towed-array that might be falsely charted onto B'. As such, all the wide-area reverberation images of data segments analyzed in this thesis are produced, and these images are visually inspected to ensure that the left-right ambiguity was not a problem for our analysis. (Although data segments such as S420 bistatic, S465 bistatic, S484 monostatic and S487 monostatic were found to have some ambiguities charted to the B' ridge, fortunately they did not bleed into the high resolution region.)

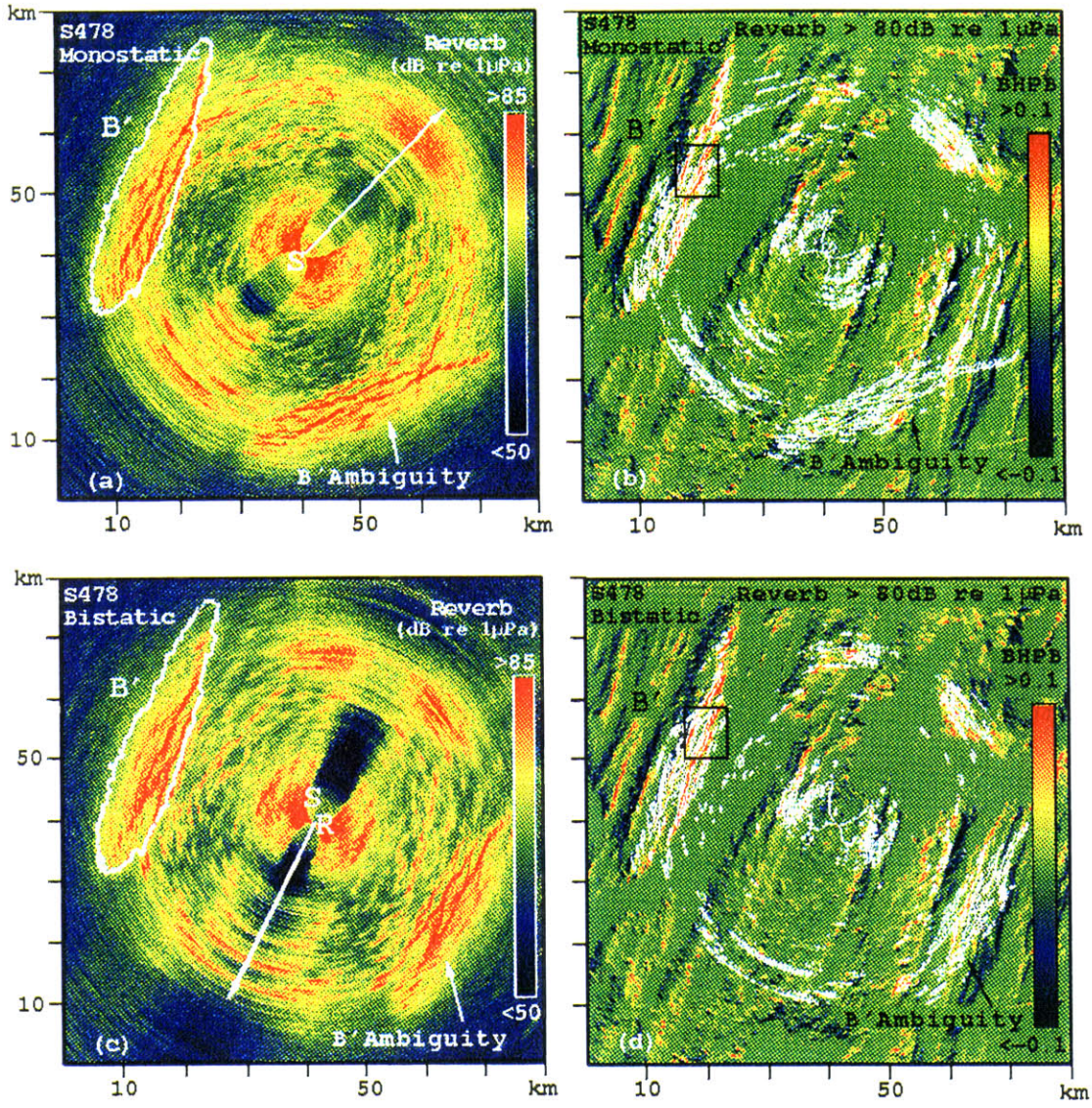

Figure 4–7 : Wide–area images of monostatic and bistatic reverberation measured for 200–255 Hz LFM S478. (a) Monostatic reverberation chart showing symmetry about the array axis for Cory heading at 45^0. (b) Contours of high level backscatter, overlain on the BHBP, coregister with major scarps on B' facing the source–receiver. (c) Bistatic reverberation chart showing circular symmetry about the Alliance's array heading at 207^0. (d) Contours of high level backscatter overlain on the BHPB.

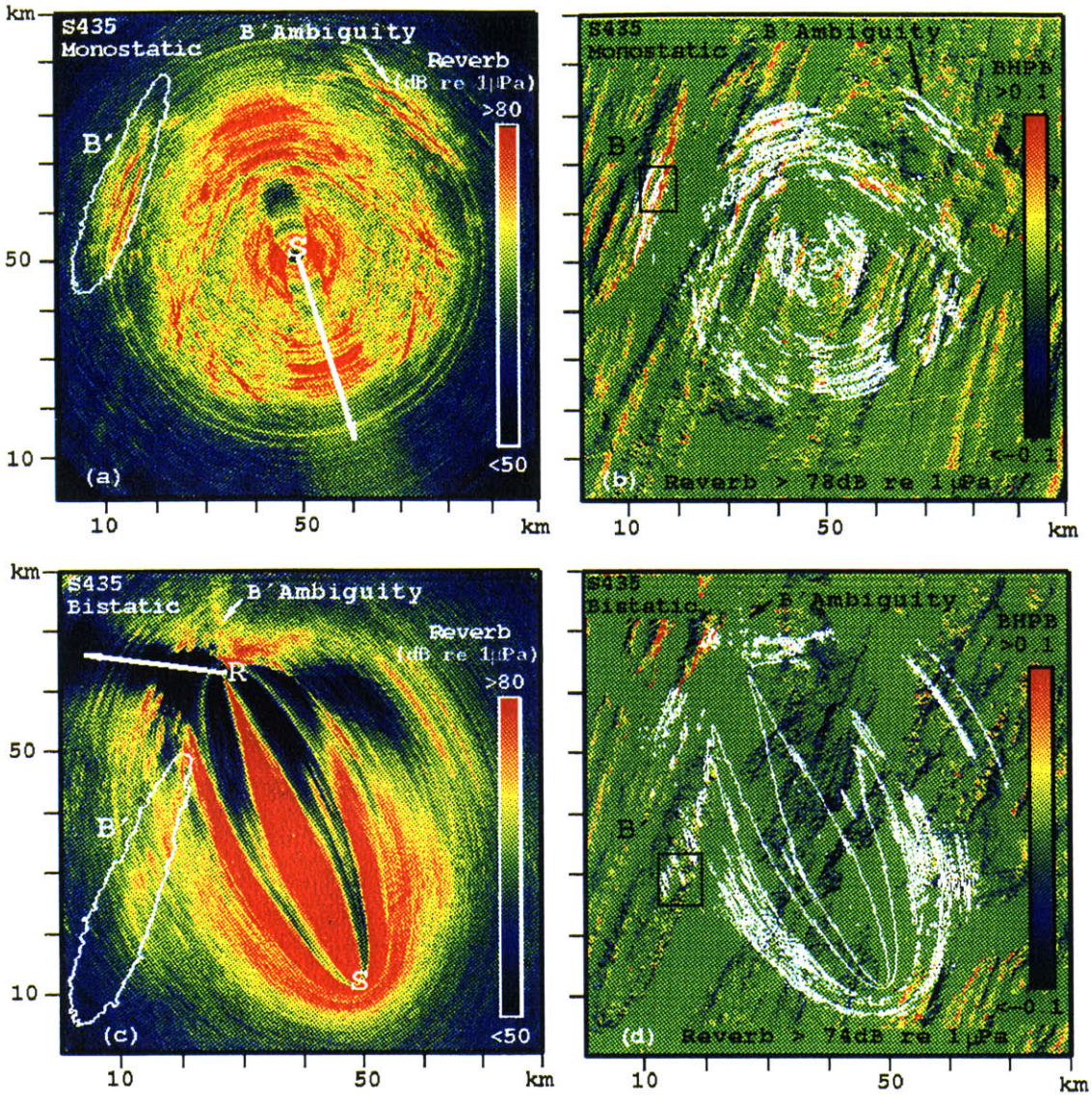

Figure 4–8: Wide–area images of monostatic and bistatic reverberation measured for 200–255 Hz LFM S435. (a) Monostatic reverberation chart showing symmetry about the array axis for Cory heading at 163^0. (b) Contours of high level backscatter, overlain on the BHBP, coregister with major scarps on B' facing the source–receiver. (c) Bistatic reverberation chart showing oblique symmetry about the Alliance's array heading at 277^0. (d) Contours of high level backscatter overlain on the BHPB.

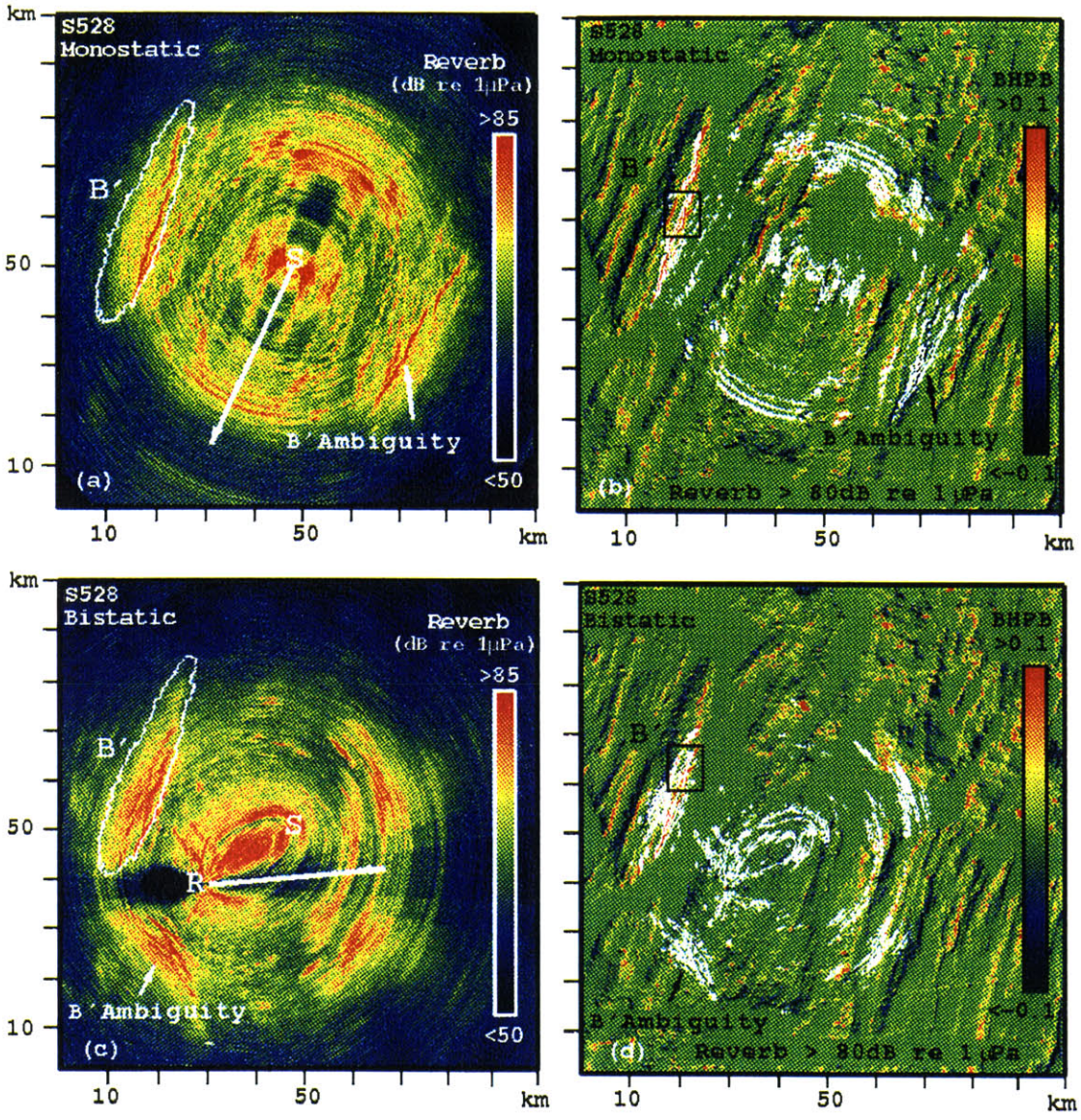

Figure 4–9: Wide–area images of monostatic and bistatic reverberation measured for 200–255 Hz LFM S528. (a) Monostatic reverberation chart showing symmetry about the array axis for Cory heading at 206^0. (b) Contours of high level backscatter, overlain on the BHBP, coregister with major scarps on B' facing the source–receiver. (c) Bistatic reverberation chart showing elliptical symmetry about the Alliance's array heading at 87^0. (d) Contours of high level backscatter overlain on the BHPB.

4.3 HIGH RESOLUTION IMAGES OF B' SCARPS

Firstly, ray-tracing is carried out to compute the two-way travel time. The bending of acoustic rays along the propagation paths is taken into account to accurately chart the long range echoes onto the 5-m high resolution bathymetry. In our study, we trace rays from a point source, at the center of Cory's source, through a bottomless ocean half-space with a pressure-release surface. A range-depth map is then produced for the minimum travel time. Similarly, another range-depth map of travel time at the receiver's location is generated by tracing rays from a point source at the center of Alliance's receiver array (since reciprocity allows us to do so). Finally, the two-way travel time maps are determined by sweeping these range-depth maps across the known bathymetry at B'. As mentioned in Chapter 3, these travel time maps are subsequently used in the bistatic mapping program to convert raw data into high resolution reverberation charts.

High resolution reverberation images for segments S435, S478 and S528 are presented in Figures 4-10 to 4-12 respectively. Locations of the upper and lower scarps are illustrated by the overlain contours in these figures. In most of the monostatic charts, such as S435 and S478, echo returns are prominently charted onto the two major scarps when the cross-range axis of sonar footprint coincides with the scarp axes. In some data segments, such as S528, there are no echo returns from the upper scarp since the entire scarp falls into the shadow zone of the source main beam's refractive path. On the other hand, echo returns from the lower scarp are consistently present in all the monostatic segments since it lies at a lower depth that is always below the shadow zone. Hence, the lower scarp is well insonified by the sonar source throughout the experiments.

Moreover, we observe that the high resolution reverberation charts for S435 and S528 bistatic receptions are significantly different from their monostatic charts, which are also noted during the wide-area analysis. In the extreme cases such as S435, the towed-array system sometimes cannot distinguish between the two scarps when its cross-range axis is normal to the scarp axes. Strong echo returns are occasionally charted across both scarps in elliptic arcs centered at the plateau region. This effect may be due to the relative close proximity of the two scarps, which is roughly 2 km separation or twice the cross-range resolution of receiving array.

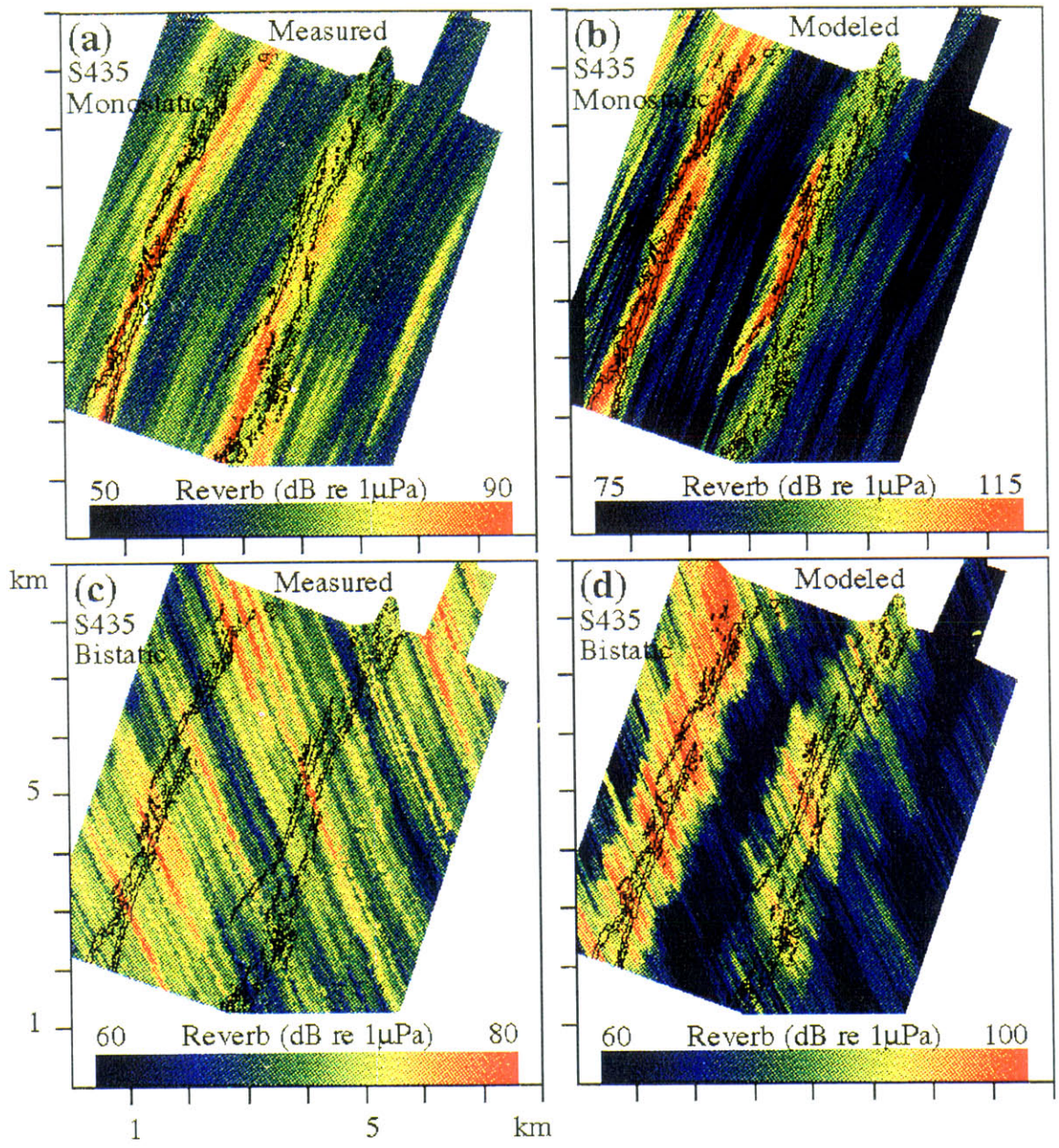

Figures 4–10: High resolution charts of monostatic and bistatic measured and modeled reverberation for S435 over the upper and lower scarp contours. (a) Measured monostatic reverberation. (b) Model monostatic reverberation. (c) Measured bistatic reverberation. (d) Modeled bistatic reverberation. Figure by Makris & Fialkowski.

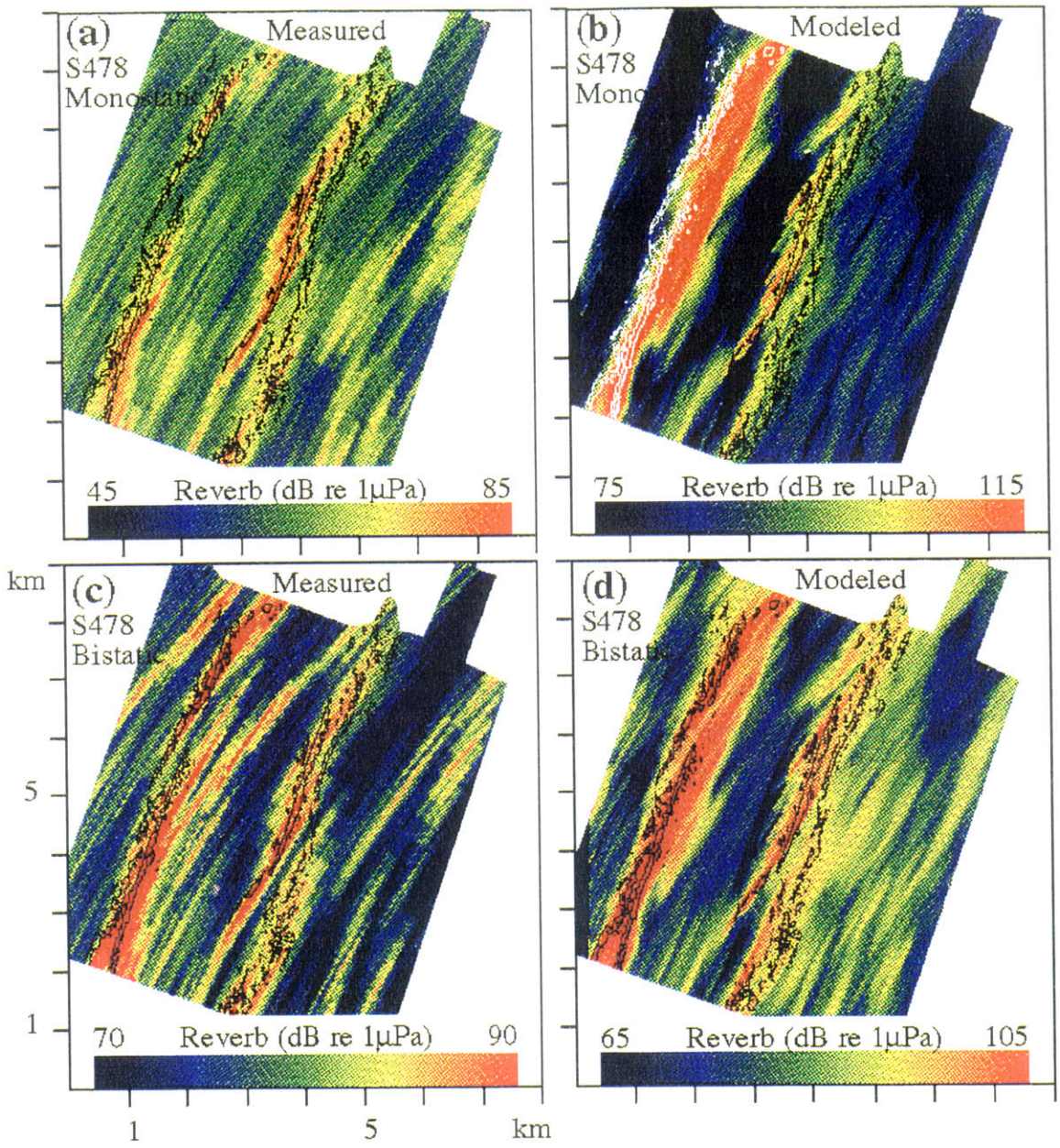

Figures 4–11: High resolution charts of monostatic and bistatic measured and modeled reverberation for S478 over the upper and lower scarp contours. (a) Measured monostatic reverberation. (b) Model monostatic reverberation. (c) Measured bistatic reverberation. (d) Modeled bistatic reverberation. Figure by Makris & Fialkowski.

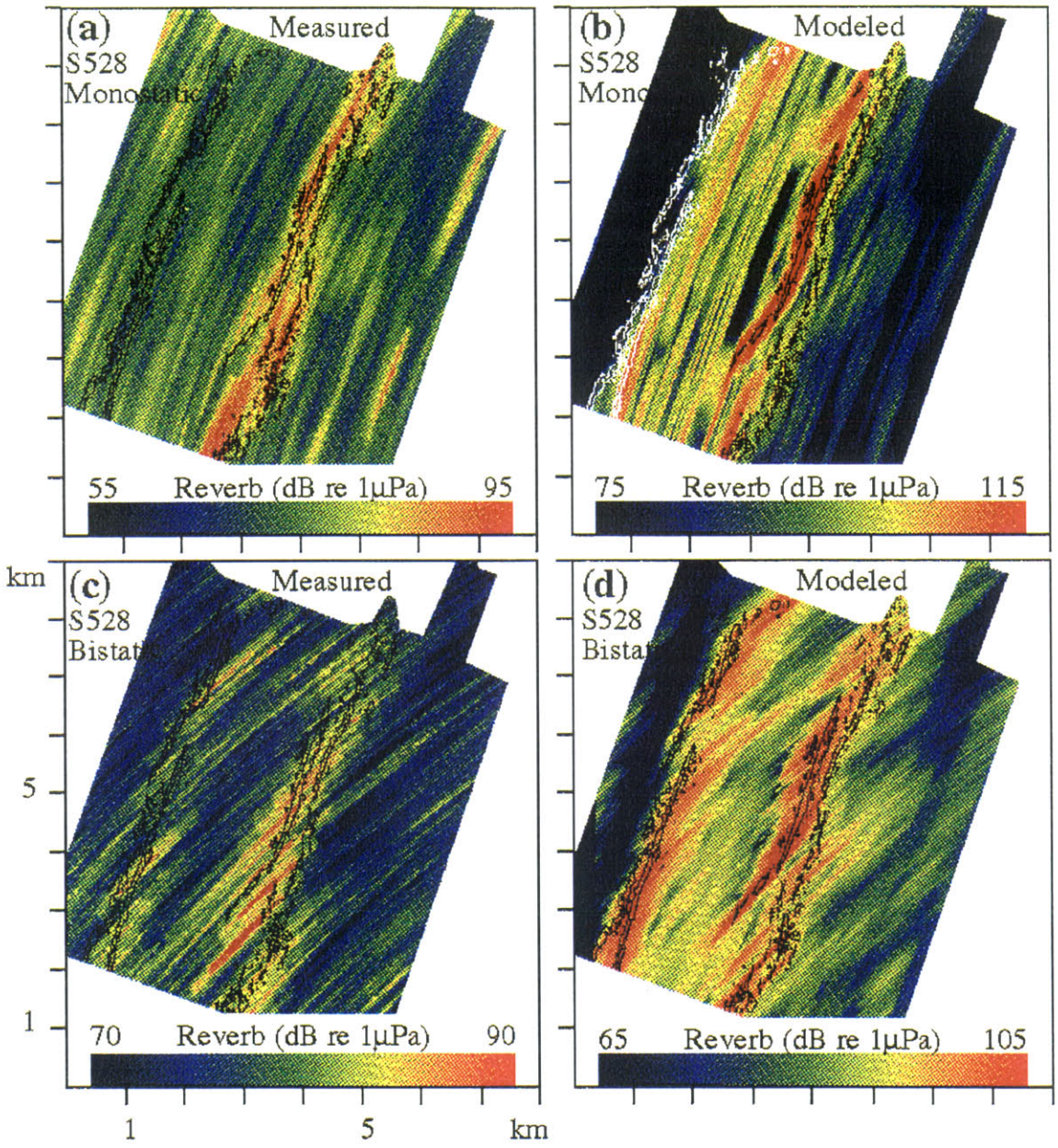

Figures 4–12: High resolution charts of monostatic and bistatic measured and modeled reverberation for S528 over the upper and lower scarp contours. (a) Measured monostatic reverberation. (b) Model monostatic reverberation. (c) Measured bistatic reverberation. (d) Modeled bistatic reverberation. Figure by Makris & Fialkowski.

4.4 HIGH RESOLUTION REVERBERATION MODELING AND SCATTERING STRENGTH ESTIMATION

From an infinitesimal planar surface patch of area dA, the scattered intensity received in the far field can be written as[14]

$$dI = f(\theta_i, \phi_i; \theta_r, \phi_r) w l_i l_r \cos\theta_i \cos\theta_r dA, \quad \textbf{(1)}$$

where θ and ϕ denote the elevation and azimuth angles with respect to the surface, and the subscripts i and r indicates the incident and scattered angles respectively. The function f is known as the bi-directional scattering distribution function (BSDF) of the surface, which is similar to the concept of bi-directional reflectance distribution function in the modern radiometry.[6] The other factors include the transmission power w, and the transmission losses l_i and l_r. For convenience, Eq (1) can be expressed in decibels as

$$R_{dA} = S(\theta_i, \phi_i; \theta_r, \phi_r) + W - TL_i - TL_r + C_i + C_r + 10\log(dA / A_{ef}) \quad \textbf{(2)}$$

with the following set of notations:

R_{dA} : Reverberation level in dB re 1 μPa,

S : Scattering strength in dB re 1 μPa @ 1 m,

W : Source level in dB re 1 μPa @ 1 m,

TL_i : Transmission loss from source to scattering patch in dB re 1 m,

TL_r : Transmission loss from the scattering patch to the receiver in dB re 1 m,

C_i, C_r : Surface projection in dB re 1 m by taking 10log of the cosine terms in Eq (1),

dA : Area term in dB re 1 m.

Since the supporting bathymetry data is represented in a Cartesian coordinates in x and y, we can express $dA = dxdy$.

Footnote: Eq (1) to (9) follow closely to Ref. [14] as discussed by Makris

However, Eq (1) and (2) do not directly describe the measured reverberation since the bathymetry within the resolution footprint of the towed arrays cannot be approximated as a planar surface. Section 4.1 has illustrated that multiple bathymetric features may exist within one resolution footprint, as well as wavelength-scale roughness. This leads to a statistical description of the expected intensity at the receiver. The resolution footprint, at ½ CZ of 33 km range, has an annular sector of roughly 50-m by 1000-m. Hence, it contains many surface roughness scales as compared to the mean acoustic wavelength of 6.7 m. The total received field from the footprint can therefore be treated as the sum of a large number of statistically independent fields scattered from the disjoint sub-regions of the seafloor scattering patch.

The expected intensity radiated from the resolution patch can then be charted to the center of that patch by performing a convolution of

$$< I(x,y|r_i,r_r) >= \int\int_{\infty}^{\infty} G(x-X,y-Y|r_i,r_r) f(\theta_i,\phi_i;\theta_r,\phi_r) w l_i l_r \cos\theta_i \cos\theta_r dXdY \quad (3)$$

where $G(x, y|r_i, r_r)$ is a point-spread function equal to the magnitude-squared of the combined linear beam pattern and matched-filter functions that define the azimuth and range resolution of the towed array system. The average intensity is a function of the source and receiver locations r_i, r_r. When the side-lobe leakage is insignificant, Eq (3) can be approximated by

$$< I(x,y|r_i,r_r) > \approx \int\int_{A_f(x,y|r_i,r_r)} f(\theta_i,\phi_i;\theta_r,\phi_r) w l_i l_r \cos\theta_i \cos\theta_r dXdY \quad (4)$$

Again, this result can be expressed in decibels which yields

$$R_{<I>}(x,y|r_i,r_r) \approx W + 10\log\left[\int\int_{A_f(x,y|r_i,r_r)} 10^{\frac{S(\theta_i,\phi_i;\theta_r,\phi_r)-TL_i-TL_r+C_i+C_r}{10}} dXdY\right] \quad (5)$$

Since the scattering strength S is not constant over the resolution footprint, any estimate of the seafloor scattering strength obtained from the high resolution analysis will be blurred over the resolution footprint of the towed-array system. For convenience, we define a modeled reverberation from the seafloor that scatters equally in all directions as

$$R_M(x,y|r_i,r_r) = W + 10\log\left[\iint_{A_f(x,y|r_i,r_r)} 10^{\frac{-TL_i-TL_r+C_i+C_r}{10}} dXdY\right] \tag{6}$$

The mean scattering strength over the resolution footprint can then be expressed as

$$\overline{S}(x,y|r_i,r_r) = R_{<I>}(x,y|r_i,r_r) - R_M(x,y|r_i,r_r) \tag{7}$$

where the dependence on the incident and scattered angles is integrated over the footprint to account for the blurring effect. The maximum likelihood estimate for $\overline{S}$ is given by

$$\hat{\overline{S}}(x,y|r_i,r_r) = R(x,y|r_i,r_r) - R_M(x,y|r_i,r_r) \tag{8}$$

which is the difference between the reverberation measured and the modeled with a diffusely scattering assumption $S = 0$.

Under the assumption that the receiver measures a circular Gaussian random (CCGR) field,[21] a bias-corrected estimate for $\overline{S}$ is then expressed as [9]

$$\hat{\overline{S}}(x,y|r_i,r_r) = R(x,y|r_i,r_r) - R_M(x,y|r_i,r_r) + (10\log e)(\psi(\mu) - \ln\mu) \tag{9}$$

where $\psi(\mu)$ Euler's psi function with measurement degrees of freedom μ. For the LFM waveform analyzed in this study, it has a bandwidth B of 55 Hz, and the instantaneous intensity measured after matched-filtering is averaged over time period T, where T=0.0625 s for Cory's reception and T=0.0533 s for Alliance's reception. Consequently, the degrees of freedom, given by $\mu = BT$, is computed to be roughly *3.4* and *3.0* for the RV Cory and Alliance respectively.

To model reverberation, we need to compute the range-depth maps of transmission loss and surface projection, using the same approach of deriving the travel time maps as described in Section 4.3. Single-frequency TL maps spanning across the 200 - 255 Hz frequency band for a 10-element source are first produced by the PE model. Subsequently, they are averaged across the entire frequency band to obtain a broadband incoherent transmission loss, which exhibits a well-defined main beam with frequency-averaged Lloyd mirror interfering beams and side-lobes, as shown in Figure 4-13 (a). The resultant source TL map is then swept through the high resolution bathymetry to obtain the incident transmission loss TL_i. Similarly, the TL_r maps are produced by modeling a point source at the depth of receiving array: 170 m for Cory, and 460 m for Alliance. These TL_r maps, as shown in Figure 4-13 (b) & (c), indicate little structure and often lead to relatively uniform transmission loss from the scattering patch to the receiver.

To find the surface projection of bathymetry at (x,y) in our Cartesian grid system, we compute the inner product of its local surface normal vector and a unit vector pointing towards the source or receiver location. The surface unit normal vector $\boldsymbol{n}$, expressed in terms of partial derivatives of the seafloor elevation $z(x,y)$ with respect to x and y, is given in Ref. [6] as

$$n = \frac{(-p,-q,1)}{\sqrt{1+p^2+q^2}}, \tag{10}$$

where $p = dz/dx$ and $q = dz/dy$. In our actual implementation, the values p and q are calculated by

$$p = \frac{z(x+dx,y)-z(x-dx,y)}{2dx},$$

and

$$q = \frac{z(x,y+dy)-z(x,y-dy)}{2dy}. \tag{11}$$

Consequently, the individual components of normal vector $\boldsymbol{n}$ are found by setting

$$n_x = \frac{-p}{\sqrt{1+p^2+q^2}},$$

$$n_y = \frac{-q}{\sqrt{1+p^2+q^2}},$$

and

$$n_z = \frac{1}{\sqrt{1+p^2+q^2}}. \qquad \textbf{(12)}$$

The grazing angle, θ_g, of the acoustic ray arriving at the local bathymetry is computed via ray-tracing in a bottomless ocean half-space as described in Section 4-3. Note that, in this method, θ_g is obtained with reference to the *horizontal plane* at the corresponding depth of local bathymetry, and not the slope gradient of bathymetry. If we define the directional vector pointing towards the source or receiver at (x_0,y_0) as vector $\boldsymbol{s}$, the individual components of this vector can be found by the following equations

$$s_x = \cos(\varphi)\cos(\theta_g),$$

$$s_y = \sin(\varphi)\cos(\theta_g),$$

and

$$s_z = \sin(\theta_g), \qquad \textbf{(13)}$$

where the azimuthal angle φ is given by

$$\varphi = \tan^{-1}\left(\frac{y-y_0}{x-x_0}\right).$$

Finally, the surface projection, which is defined as the dot product of vectors $\boldsymbol{n}$ and $\boldsymbol{s}$, is derived using the formula

$$\text{Projection} = s_x{*}n_x + s_y{*}n_y + s_z{*}n_z. \qquad \textbf{(14)}$$

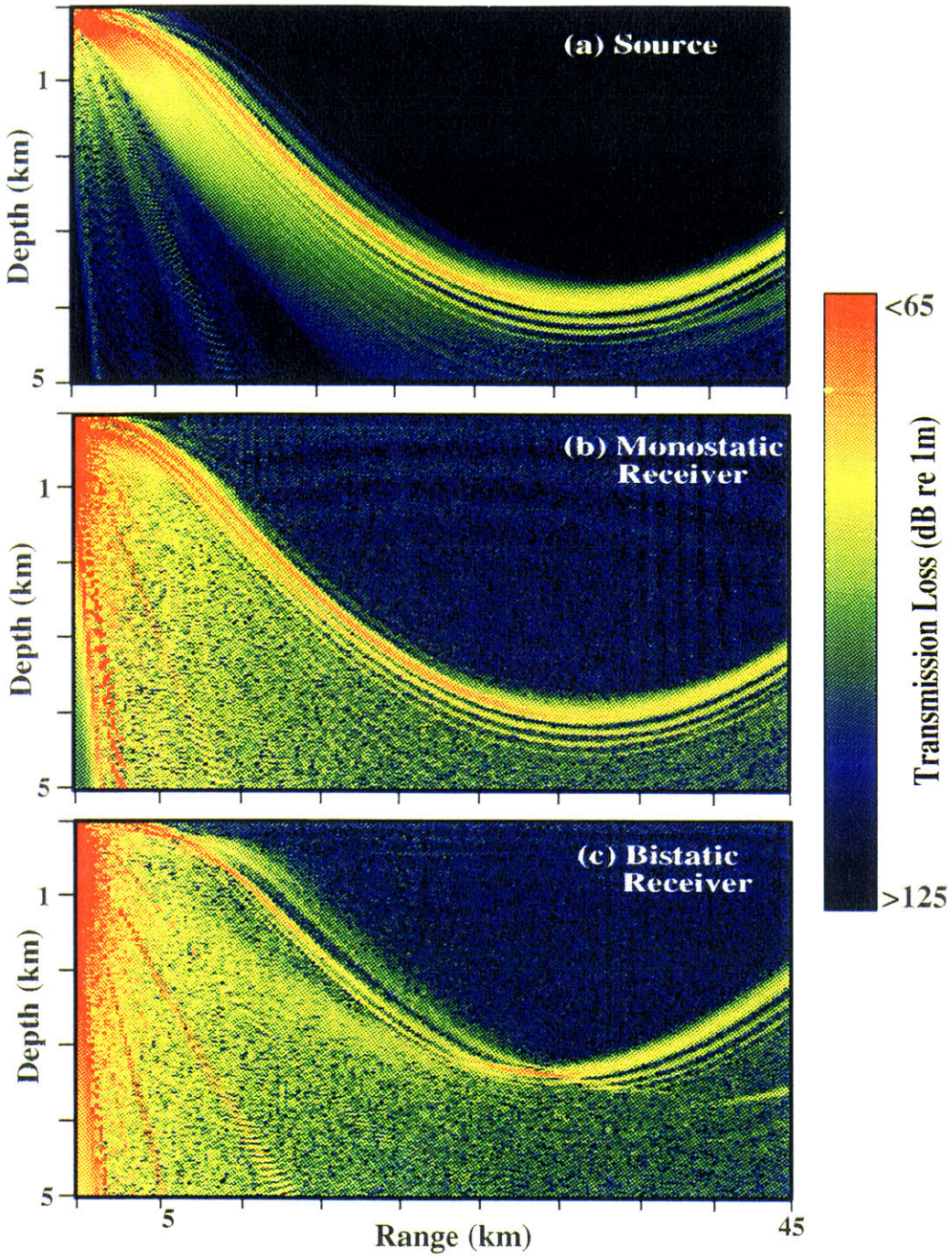

Figure 4–13: (a) Range–depth map of broadband transmission loss incoherently averaged over 200–255 Hz frequency band using Parabolic Equation with Cory's source at 181 m depth in the MAR sound speed profile given in Ref. [2] for a bottomless ocean half space. (b) Same as (a) except a point source at 170 m depth for the Cory's receiver. (c) Same as (a) except a point source at 460 m depth for the Alliance's receiver. Data provided by Makris.

4.5 COMPARISON BETWEEN MEASURED AND MODELED REVERBERATION

The modeled reverberation, as described in Eq (6), for S435, S478 and S528 are presented in Figures 4-10 through 4-12(b) & (d) respectively. Their measured reverberation charts are shown in the corresponding Figs. (a) & (c) for comparisons. Generally, the modeled and measured reverberation show high visual correlation in the monostatic charts. Prominent echo returns are observed to resolve the upper and lower scarps distinguishably when the cross-range axis of sonar footprint coincides with the scarp axes. Echo returns in the vicinity, such as the plateau between the two scarps, are typically 20 to 30 dB lower. Since this reverberation difference greatly exceeds the 5.6 dB standard deviation, one can conclude that the two scarps are deterministic features consistently charted with strong echo returns. Moreover, the model has also accurately predicted the upper scarp will fall in the shadow zone for S528. This is subsequently confirmed by the measured reverberation as shown in Fig. 4-12.

However, this close agreement only occurs in the bistatic reverberation charts when the receiver's bistatic angle is small. More often, the bistatic separation angle is too large, and elliptical arcs of both measured and modeled reverberation are charted obliquely across the scarp axes. Occasionally, some echo returns are charted at areas such as the plateau region where no scarps are present. While the general character of the measured reverberation qualitatively agrees with the modeled bistatic reverberation, one-to-one correspondence is absent when the bistatic separation is large. To explain this inconsistency in the modeled and measured reverberation charts, two possible reasons are offered in Ref. [14]. First, the model predicts variation in the expected reverberation level along the scarp with a maximum standard deviation of roughly 5.6 dB. This type of signal-dependent noise, known as *speckle*,[9,11] is sufficient to bury the reverberation pattern predicted by the model. Second, there may be charting errors that exceed the range-resolution of the towed-array system. This is possible since any fluctuations in the receiver array heading beyond 0.1^0 are sufficient to cause such errors at ½ CZ.

4.6 MEAN BI-AZIMUTHAL SCATTERING STRENGTH

Since the scarp elevation within the resolution footprint cannot be approximated as a planar surface, it is therefore meaningless to plot estimates of scattering strength as a function of incident and scattered angles. Instead, a mean bi-azimuthal scattering strength (MBASS) for the upper and lower scarps of B' is computed. In our study, the MBASS, the measured and modeled reverberation are all plotted as a function of receiver azimuth Ω_r. A full bi-azimuthal description of these parameters, with respect to source and receiver azimuths, can be regained by referring to the source-receiver location pairs as shown in Figure 4-6.

The mean reverberation level measured over the upper scarp $< R(x, y|\Omega_i, \Omega_r) >_{A_{up}}$ and the lower scarp $< R(x, y|\Omega_i, \Omega_r) >_{A_{low}}$ are plotted as a function of Ω_r in Figure 4-14 (a) & (b), together with their respective standard deviations $\sigma_{A_{up}}\{R(x, y)\}$ and $\sigma_{A_{low}}\{R(x, y)\}$. The two curves are notably flat with a gradual roll-off of roughly 5 dB from the origin to the extreme values. However, the mean value fluctuates in the order of its standard deviation, ranging from 6 dB within $|\Omega_r| < 30^0$, to roughly 3 dB beyond $|\Omega_r| > 30^0$. In view of these results, the mean measured reverberation level is considered to be spatially homogenous across the source and receiver azimuths.

High standard deviation within $|\Omega_r| < 30^0$ can be explained by the fact that the bathymetry-induced TL is most sensitive to small variations in range during the monostatic measurements when the cross-range axis of sonar footprint coincides with the scarp axes. Conversely, the standard deviation decreases as $|\Omega_r| > 30^0$ since the cross-range axis of sonar footprint is often skew obliquely across the scarp axes. It then becomes impossible for the towed-array system to miss the scarps at large $|\Omega_r|$.

The mean modeled reverberation level is computed with an assumption of diffusely scattering surface at the two scarps, $< R_M(x, y|\Omega_i, \Omega_r) >_{A_{up}}$ and $< R_M(x, y|\Omega_i, \Omega_r) >_{A_{low}}$ as shown in Figure 4-15 (a) & (b). For $|\Omega_r| > 30^0$, the standard deviations are low and typically near 5 dB. Within $|\Omega_r| < 30^0$, they vary from 7 to 10 dB, and the upper scarp exhibits larger fluctuations than the lower scarp since the main beam of source array has more consistently insonified the lower scarp. The modeled mean across the upper scarp shows a relatively flat behavior, while the

modeled mean across the lower scarp displays an apparently concave curve, with a peak near the origin and rolling off by about 10 dB at the extreme $|\Omega_r|$.

An examination of the surface projection and TL terms before spatial convolution is provided to elucidate the behavior of modeled reverberation curves. The mean surface projection $< C_i(x, y|\Omega_i, \Omega_r) + C_r(x, y|\Omega_i, \Omega_r) >_{A_{up}}$, $< C_i(x, y|\Omega_i, \Omega_r) + C_r(x, y|\Omega_i, \Omega_r) >_{A_{low}}$ over the upper and lower scarps are plotted as a function of Ω_r in Figure 4-16. The two curves display a smooth concave behavior with small standard deviations across the receiver azimuths. Maximum deviation of the mean value is within 5 dB, with the peak value at the origin. However, each of the roll off falls within the standard deviations of the two-way transmission loss curves, which typically exceed 10 dB. Hence, the concave behavior of the mean surface projection curves will be buried by the two-way TL in the modeled reverberation when these two terms are added together.

The mean two-way transmission loss $< TL_i(x, y|\Omega_i, \Omega_r) + TL_r(x, y|\Omega_i, \Omega_r) >_{A_{up}}$, $< TL_i(x, y|\Omega_i, \Omega_r) + TL_r(x, y|\Omega_i, \Omega_r) >_{A_{low}}$ over the two scarps are plotted in Figure 4-17. Large fluctuations in the two-way TL occur as a consequence of the upper scarp, in some data segments such as S528, falls into the shadow zone of the source's acoustics path. Since the lower scarp is constantly outside the shadow zone, the variations in its mean are smaller such that a concave dependence is observed across Ω_r. This leads to a similar concave behavior in the modeled reverberation curve, and perhaps also in the measured reverberation. Compared to the two-way TL curves, the mean modeled and measured reverberation curves exhibit smaller standard deviations. This is mainly due to the smoothing effects of spatial convolution within the sonar resolution footprint.

The MBASS curves estimated for the upper scarp $< \hat{\bar{S}}(x, y|\Omega_i, \Omega_r) >_{A_{up}}$ and lower scarp $< \hat{\bar{S}}(x, y|\Omega_i, \Omega_r) >_{A_{low}}$ are plotted in Figure 4-18, along with their respective standard deviations $\sigma_{A_{up}}\{\hat{\bar{S}}(x, y)\}$ and $\sigma_{A_{low}}\{\hat{\bar{S}}(x, y)\}$. The mean scattering strength computed over the upper scarp shows a relatively flat behavior within *-17 dB +/- 8 dB*. Large fluctuations in the mean value for small $|\Omega_r|$ can be explained by the similar observations found in modeled and measured reverberation curves. Although the mean scattering strength computed over the lower scarp

displays a mild concave trend, this trend still falls within the standard deviation of 7 dB. Consequently, a constant line of -17 dB can be drawn across the entire receiver azimuths for both curves.

In summary, our results indicate that spatial variations in the transmission loss and projected area lead to the dominant spatial variations in measured reverberation at long range. Moreover, the mean bi-azimuthal scattering strengths of the upper and lower scarps of B' are found to be identical, and roughly equal to the constant *-17dB +/- 8dB*. This suggests that long-range reverberation from the ocean basin can be adequately modeled from the two environmental inputs: (1) refractive index of the water column, and (2) seafloor bathymetry.

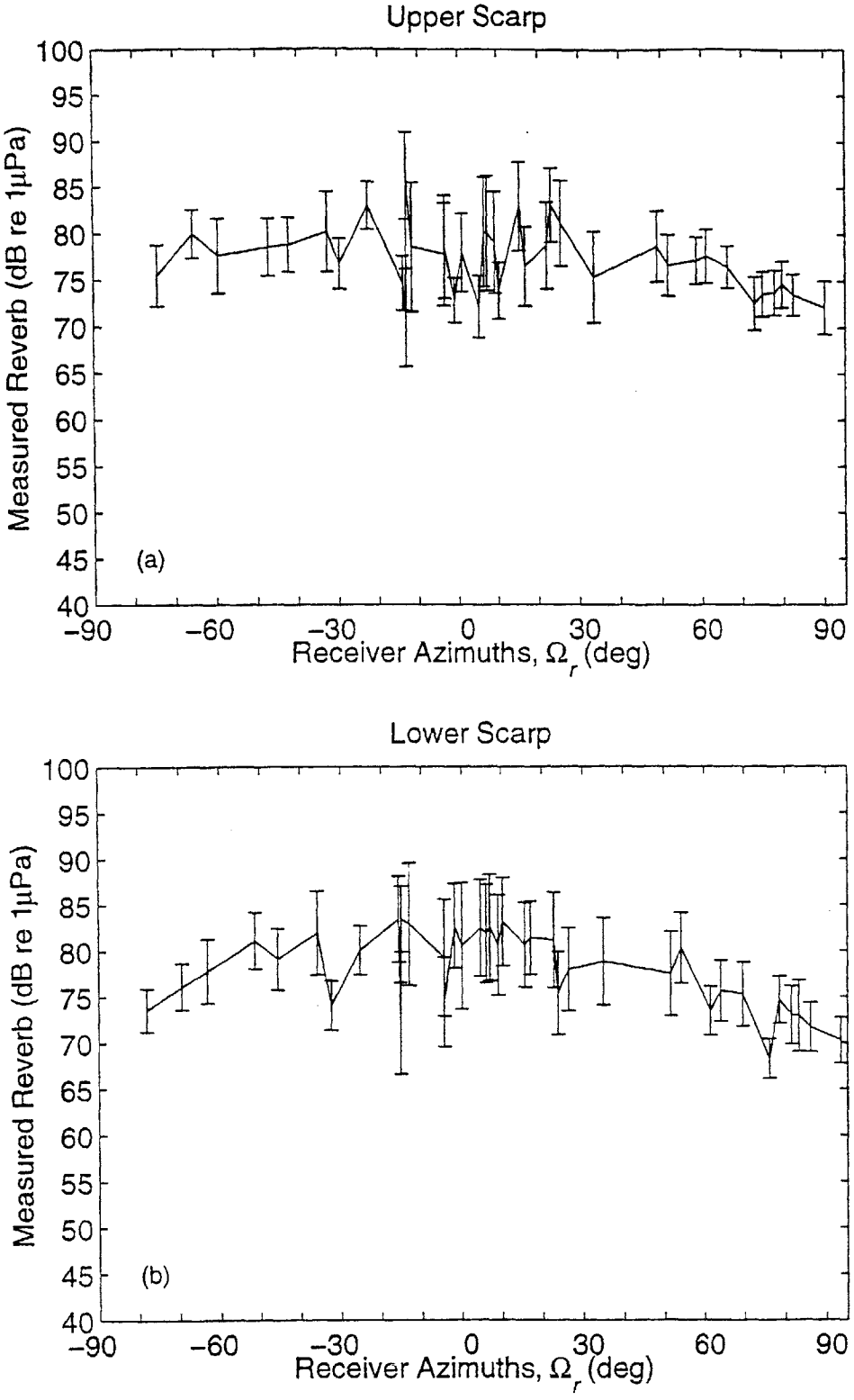

Figure 4-14: The mean reverberation level measured over (a) the upper scarp $< R(x, y|\Omega_i, \Omega_r) >_{A_{up}}$ and (b) the lower scarp $< R(x, y|\Omega_i, \Omega_r) >_{A_{low}}$ are plotted as a function of receiver azimuth Ω_r with their respective standard deviations $\sigma_{A_{up}}\{R(x, y)\}$, $\sigma_{A_{low}}\{R(x, y)\}$. Data provided by Makris & Fialkowski.

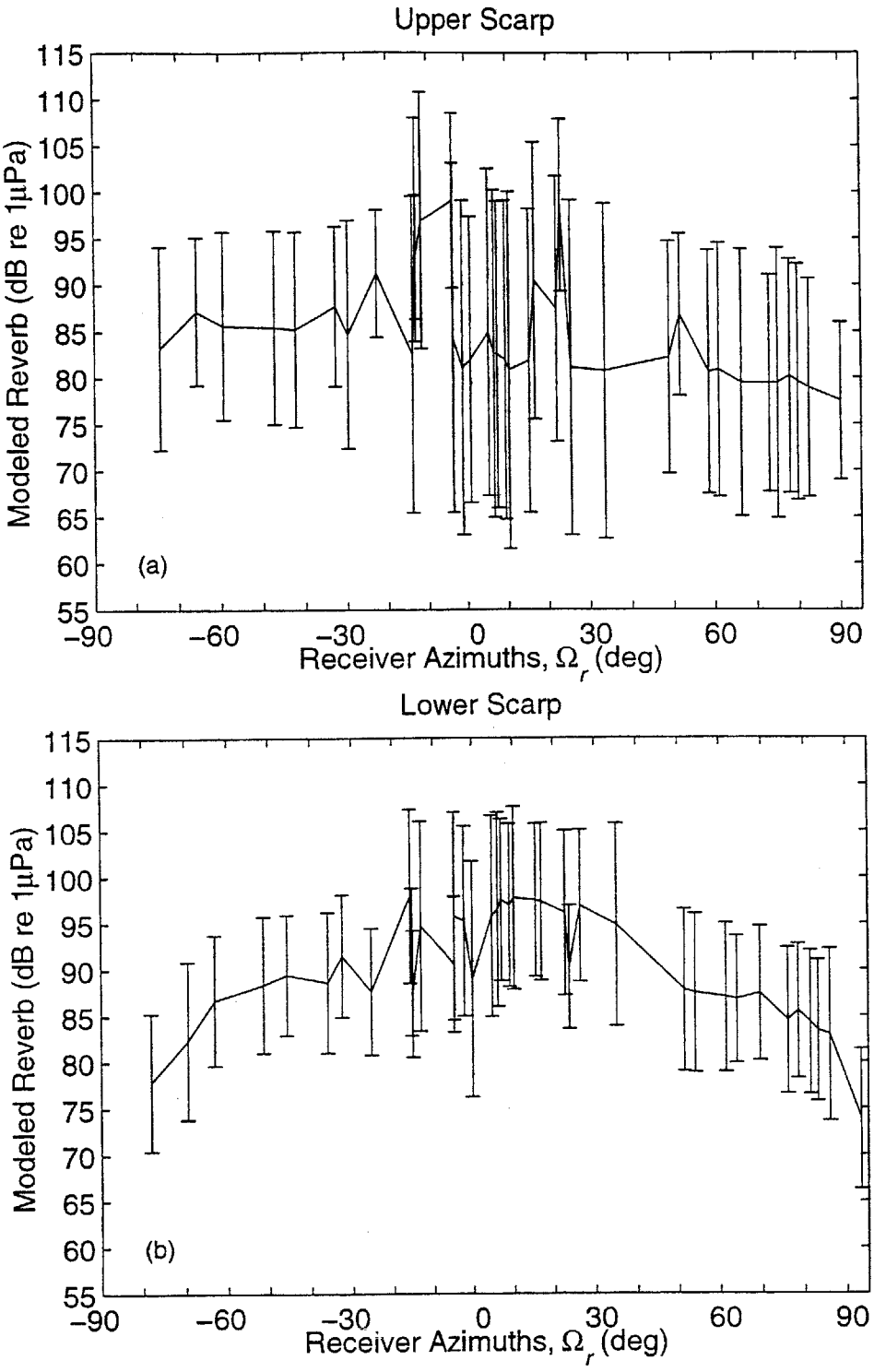

Figure 4-15: The mean modeled reverberation level is computed with the assumption of diffusely scattering surface in (a) the upper scarp, $< R_M(x, y|\Omega_i, \Omega_r) >_{A_{up}}$ and (b) the lower scarp $< R_M(x, y|\Omega_i, \Omega_r) >_{A_{low}}$ as a function of receiver azimuth Ω_r with their respective standard deviations $\sigma_{A_{up}}\{R_M(x, y)\}$, $\sigma_{A_{low}}\{R_M(x, y)\}$. Data provided by Makris & Fialkowski.

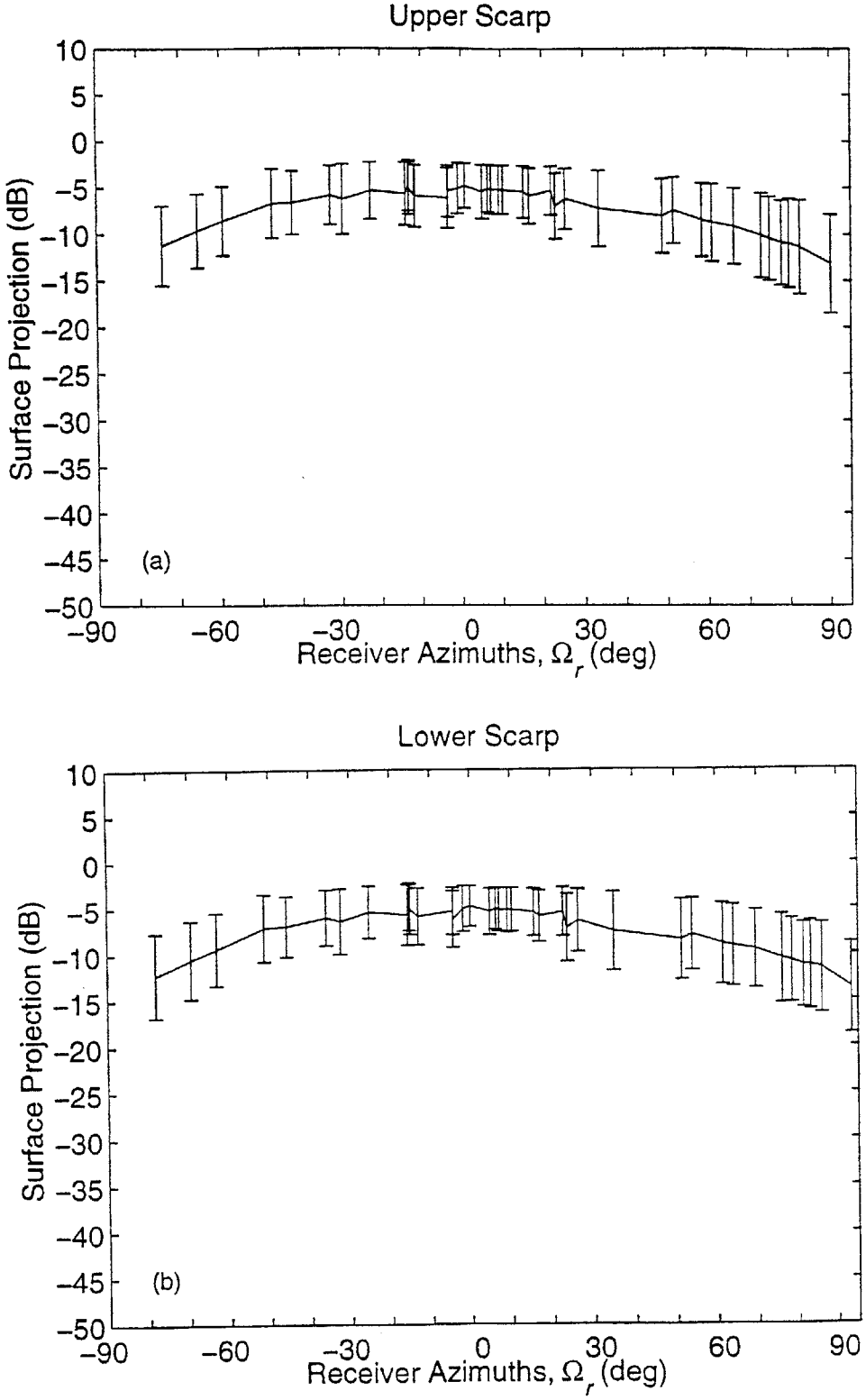

Figure 4-16: The mean surface projection over (a) the upper scarp $< C_i(x, y|\Omega_i, \Omega_r) + C_r(x, y|\Omega_i, \Omega_r) >_{A_{up}}$ and (b) the lower scarp $< C_i(x, y|\Omega_i, \Omega_r) + C_r(x, y|\Omega_i, \Omega_r) >_{A_{low}}$ as a function of receiver azimuth Ω_r with their respective standard deviations. Data provided by Makris & Fialkowski.

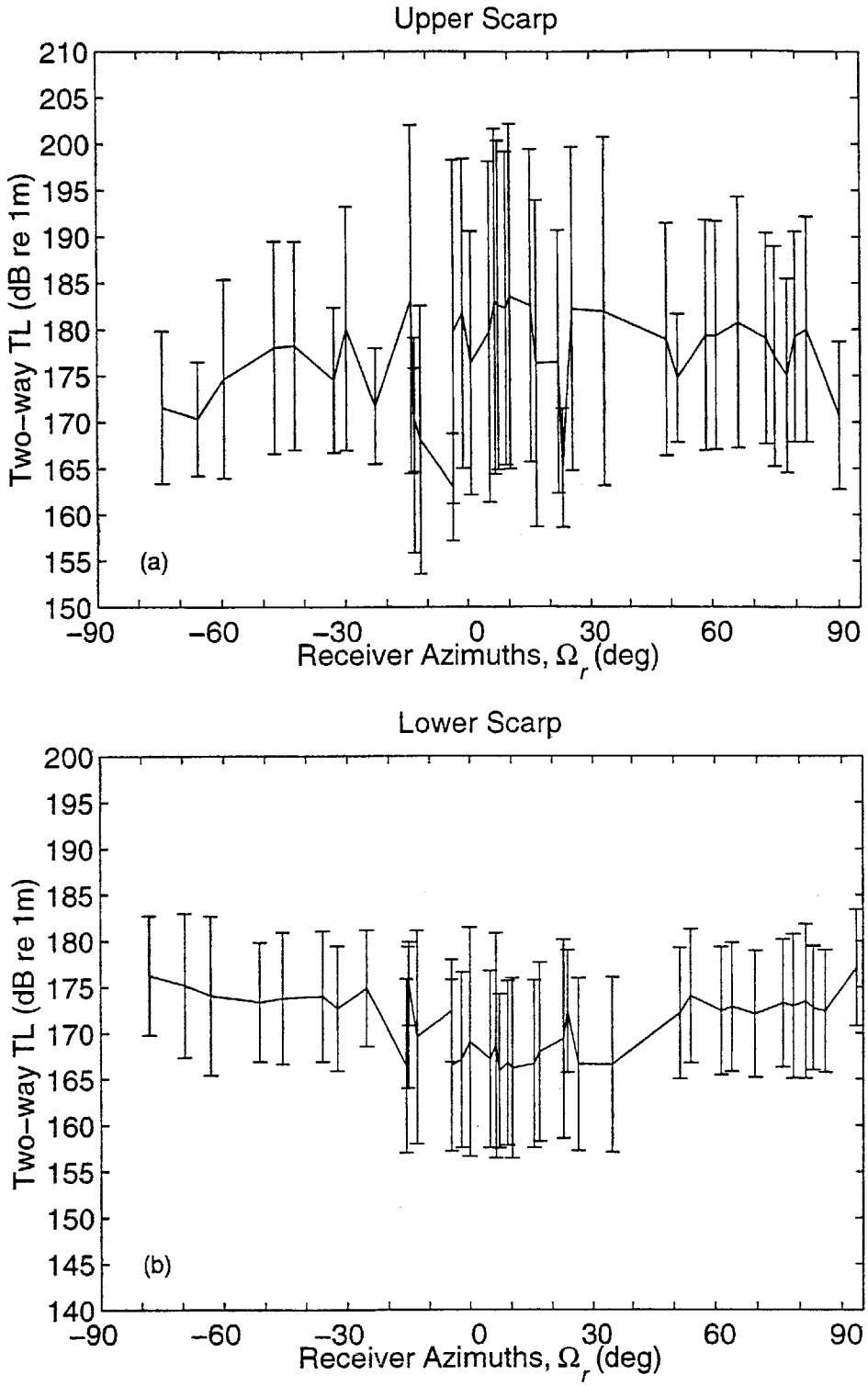

Figure 4-17: The mean 2-way transmission loss over (a) the upper scarp $< TL_i(x, y|\Omega_i, \Omega_r) + TL_r(x, y|\Omega_i, \Omega_r) >_{A_{up}}$ and (b) the lower scarp $< TL_i(x, y|\Omega_i, \Omega_r) + TL_r(x, y|\Omega_i, \Omega_r) >_{A_{low}}$ as a function of receiver azimuth Ω_r with their respective standard deviations. Data provided by Makris & Fialkowski.

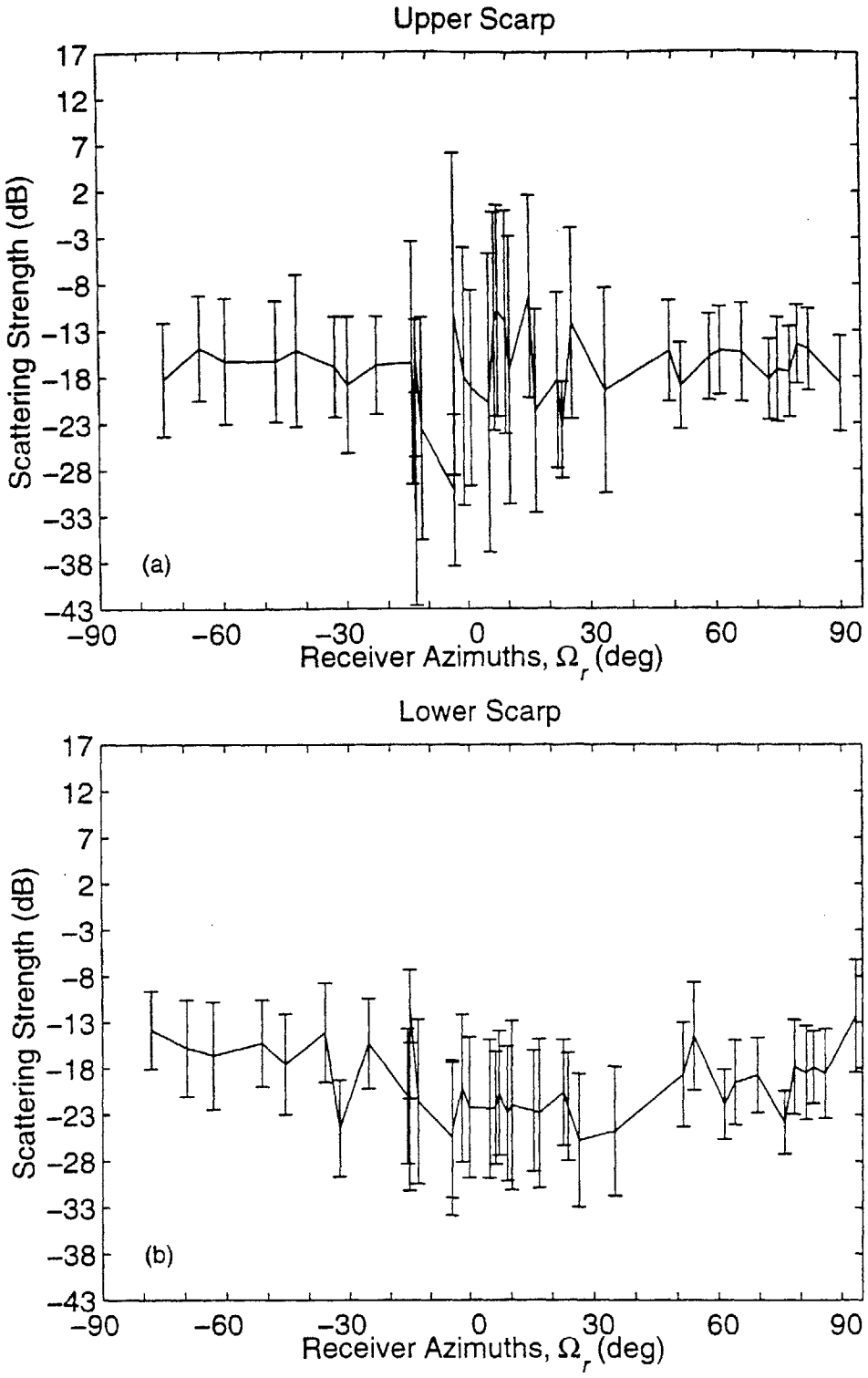

Figure 4-18: The MBASS curves estimated for (a) the upper scarp $< \hat{\bar{S}}(x, y|\Omega_i, \Omega_r) >_{A_{up}}$ and (b) the lower scarp $< \hat{\bar{S}}(x, y|\Omega_i, \Omega_r) >_{A_{low}}$ as a function of receiver azimuth Ω_r along with their standard deviations $\sigma_{A_{up}}\{\hat{\bar{S}}(x, y)\}$, $\sigma_{A_{low}}\{\hat{\bar{S}}(x, y)\}$. The mean scattering strength fluctuates within a constant value of roughly -17 dB +/- 8 dB. Data provided by Makris & Fialkowski.

5 BI-AZIMUTHAL SCATTERING DISTRIBUTION OF C'

Prior to this thesis, the bistatic scattering on C' (an inside corner) has not yet been analyzed in full detail. Since B' and C' span the two geologically distinct classes of ridges found in the Mid-Atlantic Ocean,[4,5,13] it is useful to compare their scattering characteristics. The outcome of this comparison will determine whether their scattering functions may be extrapolated to the other ocean ridges.

5.1 GEOMORPHOLOGY OF THE C' INSIDE CORNER

The C' ridge, known as *an inside corner*, is approximately 20 km long by 10 km wide, with a height of roughly 3,200 m rising above the surrounding segment valley. Figure 5-1(a) shows the geomorphology of C' at a resolution of 200 m. The black box at the South-West (SW) corner of C' indicates the 3 x 2 km scarp area designated for this study. This SW corner is selected since it is a section of C' that is constantly insonified by the sonar source's main beam throughout the experiments.

There are two main morphological differences between the outside corner B' and inside corner C'. First, in contrast to the long linear scarps found at B', there are no extensive lineated scarps at C'. In fact, the scarps at C' are relatively short and scattered over the entire ridge. Second, while the major scarps at B' often run parallel to its ridge axis, the scarps at C' appear to be irregularly orientated. As shown by the zoom-in plots in Fig. 5-1, the SW corner of C' reveals a steep scarp that is inclined at roughly 22.5^0 from true North. Since the SW corner's scarp extends from 4,000 m to 3,500 m, it well covers the source's conjugate depth of 3,800 m. Hence, we expect this scarp area to intersect the source's acoustic refractive path at ½ CZ stand-off range.

The structural difference between the B' and C' ridges can also be illustrated by the directional derivative (DD) chart of C', as shown in Figure 5-1(b). This directional derivative is computed with the source located to the west of C', and particularly corresponds to segment S229 transmission. The surfaces of C' facing the source are registered with positive DD, and

surfaces facing away are registered with negative DD. While B' reveals two distinct lines of positive DD running parallel to its ridge axis, the DD pattern of C' appears somewhat irregular and speckle-like over the entire ridge. Although the SW corner of C' exhibits a more prominent DD pattern, it is short and diffusive as compared to the major scarps of B'. Moreover, the DD pattern of C' is sensitive to small changes in the source-receiver orientation, as will be discussed in subsequent sections. Generally, this speckled DD pattern is consistent with the known geomorphology of C' which is characterized by irregularly oriented faults.

Besides the structural difference, the crust composition of B' and C' is known to be different: C' consists largely of serpentinities, while B' is likely to be basaltic. In this thesis, our emphasis is to evaluate the effects of transmission loss and surface projection of the seafloor features on their bistatic reverberation. Hence, their material compositions are assumed to be of secondary importance to the measured reverberation at long range. So far, this assumption has been supported by the previous results obtained at B'.

The locations of the two research vessels for data segments analyzed in this thesis are shown in Figure 5-2. The central black box in this figure indicates the 3 x 2 km scarp area at the SW corner of C' designated for our study. A total of 10 monostatic and 22 bistatic segments has been analyzed to cover a full suite of 180^0 bistatic angles, with respect to the center of SW box. The boxed alphabets indicate the RV Cory's locations, while the corresponding unboxed alphabets denote the RV Alliance's locations for the same transmission. These ship locations are roughly distributed in a semi-circle, centered about the black box, with bisecting diameter oriented along the scarp axis (~22.5^0) of the SW corner at C'.

The bi-azimuthal distribution of the source-receiver location pairs is plotted in Figure 5-3. Azimuth is measured counterclockwise by a vector that originates from the center of SW box, and points normal to its scarp axis in a northwesterly direction. Specifically, $\Omega_i=0^0$ corresponds to the vector pointing to the RV Cory's location for segment S229 (indicated by alphabet F in Fig. 5-2), which is located at the center of *Easterstar* ship tracks. While the source azimuths Ω_i fall within $|\Omega_i| < 30^0$, the receiver azimuths Ω_r span over +/- 90^0 sector for a complete study of bi-azimuthal scattering at C'.

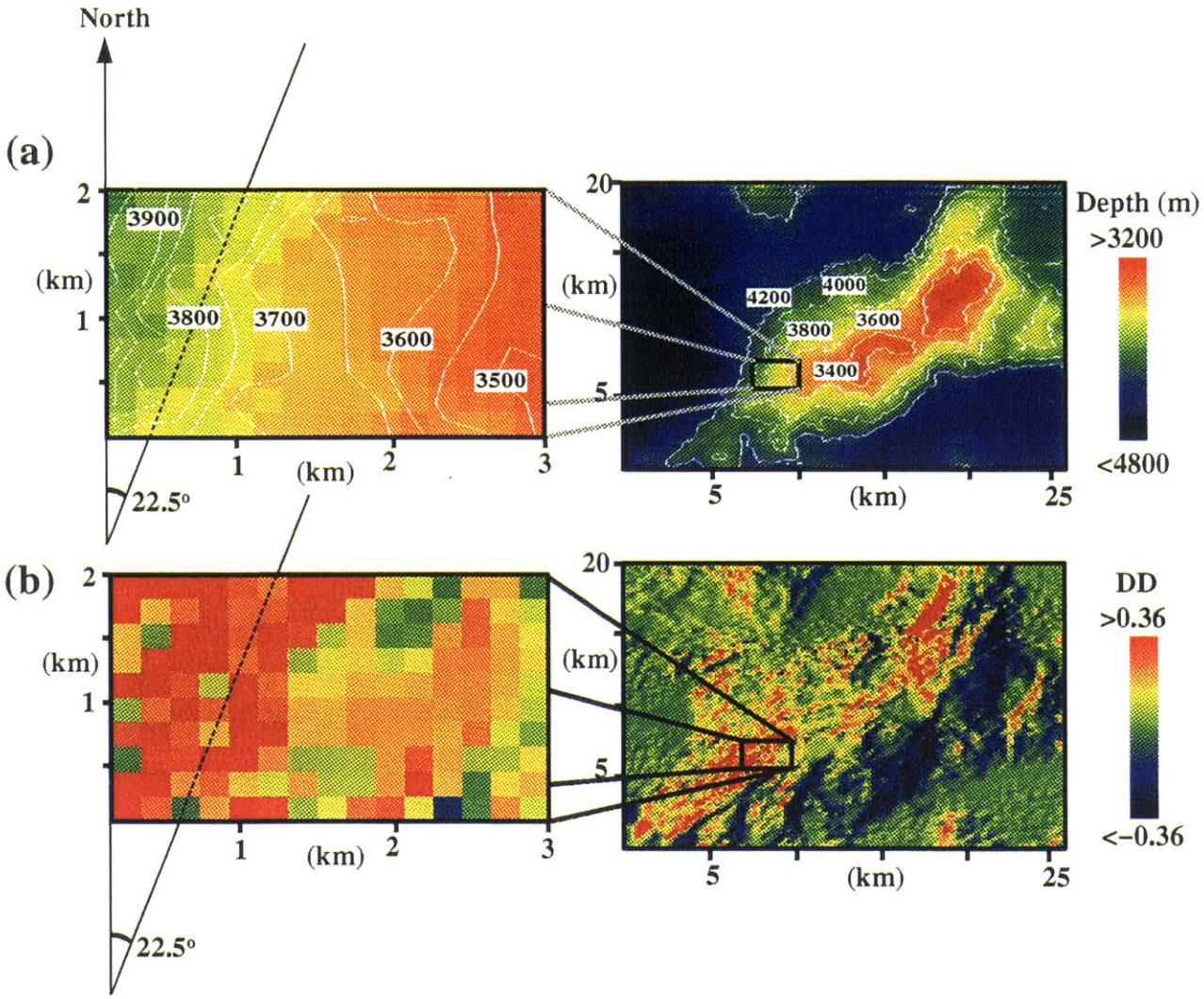

Figure 5–1: (a) The bathymetry of C' ridge, an inside corner which rises to a height of roughly 3,200 m above the surrounding segment valley, plotted at 200–m resolution grid. The black box at the SW corner of C' indicates the 3 x 2 km area chosen for this study. (b) The directional derivative (DD) computed with the source located to the west of C', which corresponds to S229 transmission. The steep slopes at C' are charted in red with DD >0.36, equivalent to slope gradients $>20^0$.

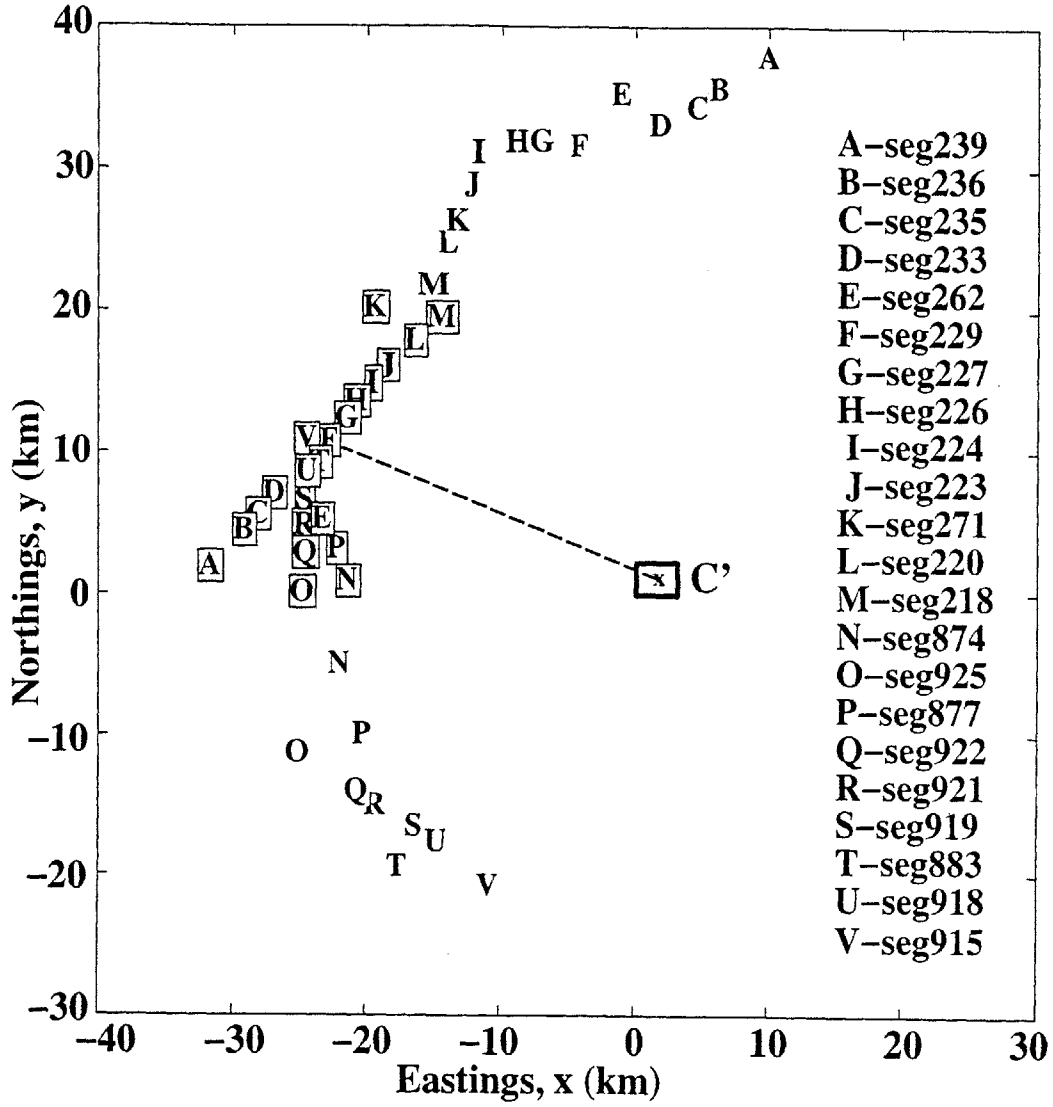

Figure 5-2: Bistatic locations of the two research vessels during the LFM transmissions analyzed in the C' study, given in Eastings and Northings. These locations are distributed in a semi-circle about the center of SW box, which indicates the scarp area designated for our study. The boxed alphabets denote the RV Cory's locations (i.e. the source locations), while the corresponding unboxed alphabets along the circular arc denote the RV Alliance's locations (i.e. bistatic receiver locations) for the same transmission.

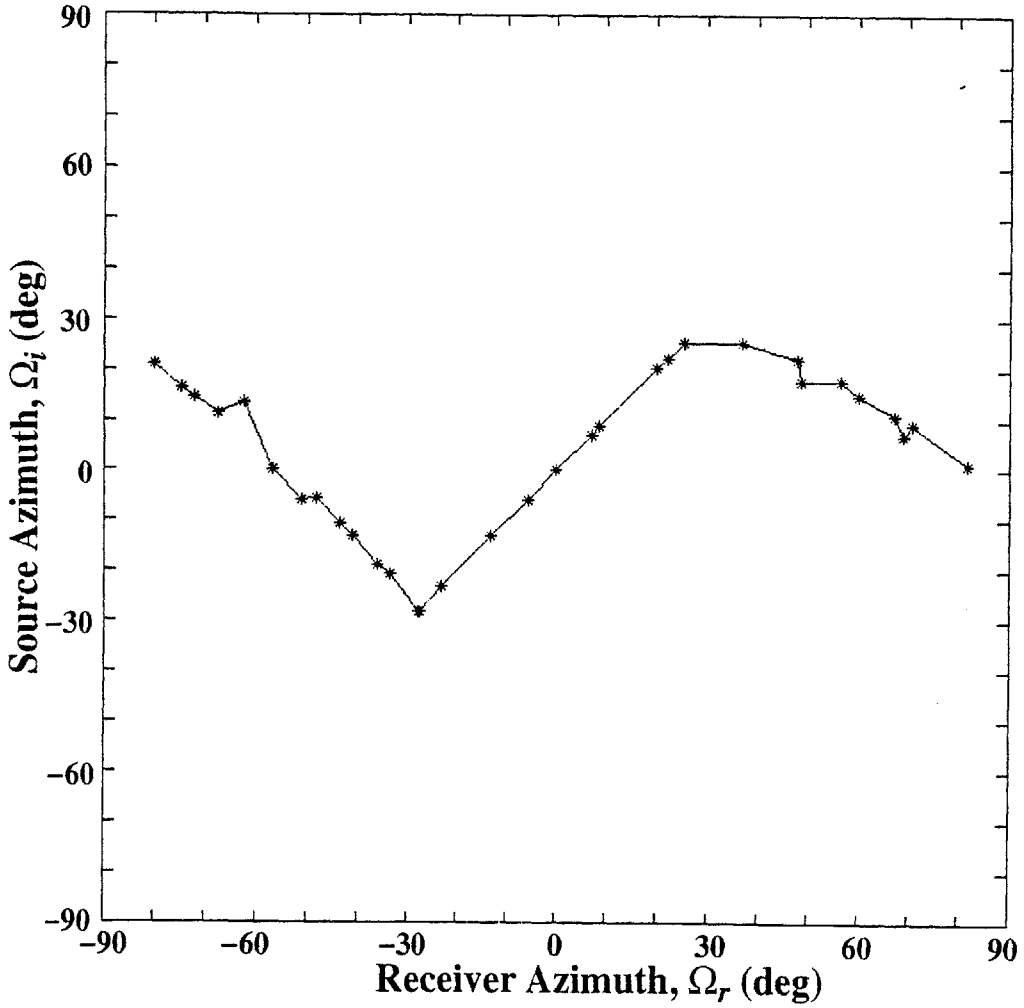

Figure 5-3: The azimuthal distribution of the source-receiver pairs for the C' study. While the source azimuths Ω_i fall within $|\Omega_i|<30^0$, the receiver azimuths Ω_r cover a full 180^0 sector of bistatic measurements at C'.

5.2 WIDE-AREA BISTATIC IMAGES

The monostatic and bistatic reverberation charts for S229, S874 and S883 are presented in Figures 5-4 to 5-6 respectively. In these segments, the RV Alliance was located at the broadside of C' in S874, at mid-way to the northern extreme in S229, and at mid-way to the southern extreme in S883. In particular, the source-receiver pairs are distributed at Ω_i ~0^0, Ω_r ~-57^0 for S229, Ω_i ~25^0, Ω_r ~37^0 for S874 and Ω_i ~7^0, Ω_r ~69^0 for S883. Consequently, these bistatic locations and their different towed-array headings lead to a variety of reverberation charts that occurred within the 180^0 bistatic angles.

As shown in Figures 5-4(a) to 5-6(a), prominent echoes are primarily charted onto the western scarps of C' since the RV Cory was located to the west of C' throughout the experiments. Since the Cory's source and its towed-array receiver are close to each other (~1.2 km), this leads to a quasi-monostatic reception at ½ CZ range. Echo returns are ambiguously mirrored across the Cory receiver's axis due to the inherent left-right ambiguity of the towed array. This leads to a circular symmetry pattern about the Cory's towed-array heading in all the monostatic reverberation charts.

Some differences in the measured reverberation patterns can be found when these monostatic reverberation charts are closely examined. For example, the echo returns from C' in segment S874 are substantially different from the segments S229 and S883, predominately due to changes in the sonar source's location. This also partly explains the fact that the scarps at C' are irregularly oriented, and their surface projections differ even for a small change of the source's location in these monostatic receptions. In which case, the echo returns are accordingly altered by variations in the projected area of bathymetry.

The bistatic reverberation charts, in Figures 5-4(c) to 5-6(c), demonstrate three ways of reverberation mapping that are possible in a typical bistatic sonar reception. Firstly, we observe a circular symmetry pattern, similar to that of its monostatic reverberation, in the S874 bistatic chart [Figure 5-5(c)]. This is not surprising since the separation between the RV Cory and Alliance is relatively short (~ 6 km), and the range ambiguity at ½ CZ is mapped onto a circular contour. Moreover, the C' ambiguity is reflected across the receiver's axis with negligible distortions in its image.

Secondly, for the S883 bistatic chart [Figure 5-6(c)], the range ambiguity is observed to follow an elliptical contour that is characteristics of bistatic sonar. A distinct left-right ambiguity symmetry, about the source-receiver axis or the major axis of ellipse, is displayed since the receiver's heading coincides with the source-receiver axis. While the echo ambiguity is mapped along the elliptical contour, it occupies a similar spatial area as the true return.

Thirdly, a distorted reverberation pattern is observed in the S229 bistatic chart [Figure 5-4(c)] when the receiver's heading is tilted considerably from the source-receiver axis. This distortion occurs because the C' ambiguity is compressed into a smaller spatial area than the true return, in accordance with the cross-range resolution of sonar footprint along the bistatic ellipse. Concurrently, the C' ambiguity falls at a shorter distance across the receiver's axis than the true return to preserve the two-way travel time.

Figures 5-4 to 5-6(b) & (d) illustrate a variety of BHBP patterns computed at C', overlain with high-amplitude reverberation contours that are threshold from their respective reverberation charts. The black box at the SW corner of C' indicates the scarp area designated for our study. Most of the western scarps at C' are registered with positive BHBP in these monostatic charts, and prominent echoes are found to correlated well with these positive BHBP patterns. On the other hand, the bistatic BHBP charts vary moderately over these three segments due to their different source-receiver orientations. In the extreme case of S883, only the SW corner is registered with positive BHBP, which corresponds well to the returned echoes [see Fig. 5-6(d)]. This happens because RV Alliance (receiver ship) has moved to the south-west extreme of C' in this segment, and the western scarps become partially blocked by its SW corner scarp along the receiver's field of view. In fact, the SW corner scarp is the only sector of C' that is well insonified by the source, and remains visible to the receiver throughout the 180^0 bistatic angles.

Wide-area images for all the data segments analyzed in this thesis have also been processed and checked that the left-right ambiguity of towed array was not a problem for our analysis. (Although data segments such as S220 monostatic, S919 monostatic and S925 monostatic were found to have some ambiguities charted to the C' ridge, fortunately they did not bleed into the designated SW corner.)

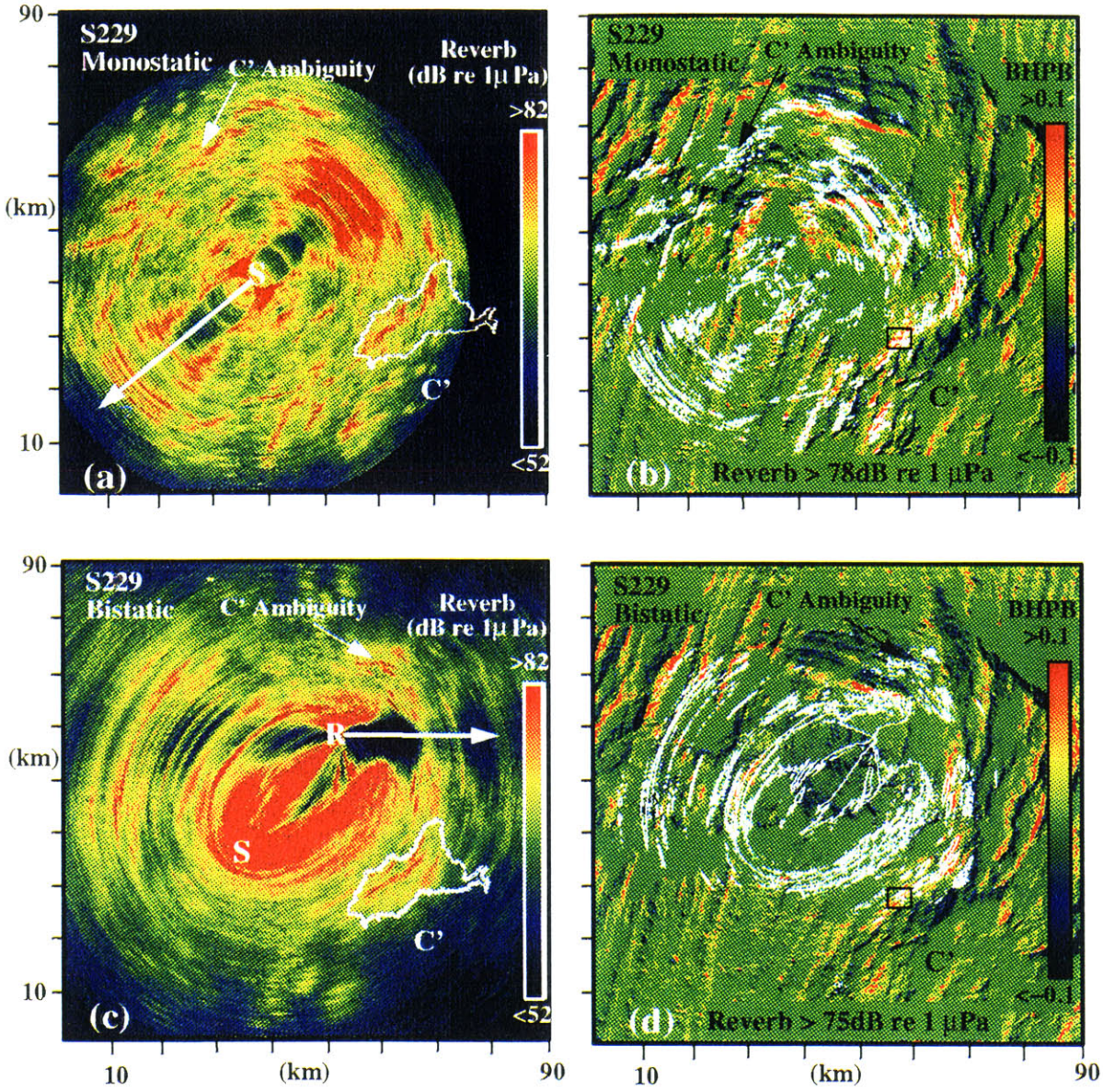

Figure 5–4: Wide–area images of monostatic and bistatic reverberation measured for 200–255 Hz LFM S229. (a) Monostatic reverberation chart showing symmetry about the array axis for Cory heading at 228^0. (b) Contours of high level backscatter, overlain on the BHBP, coregister with major scarps on C' facing the source–receiver. (c) Bistatic reverberation chart showing oblique symmetry about the Alliance's array heading at 91^0. (d) Contours of high level backscatter overlain on the BHPB. The SW box is shown in black in (c) & (d).

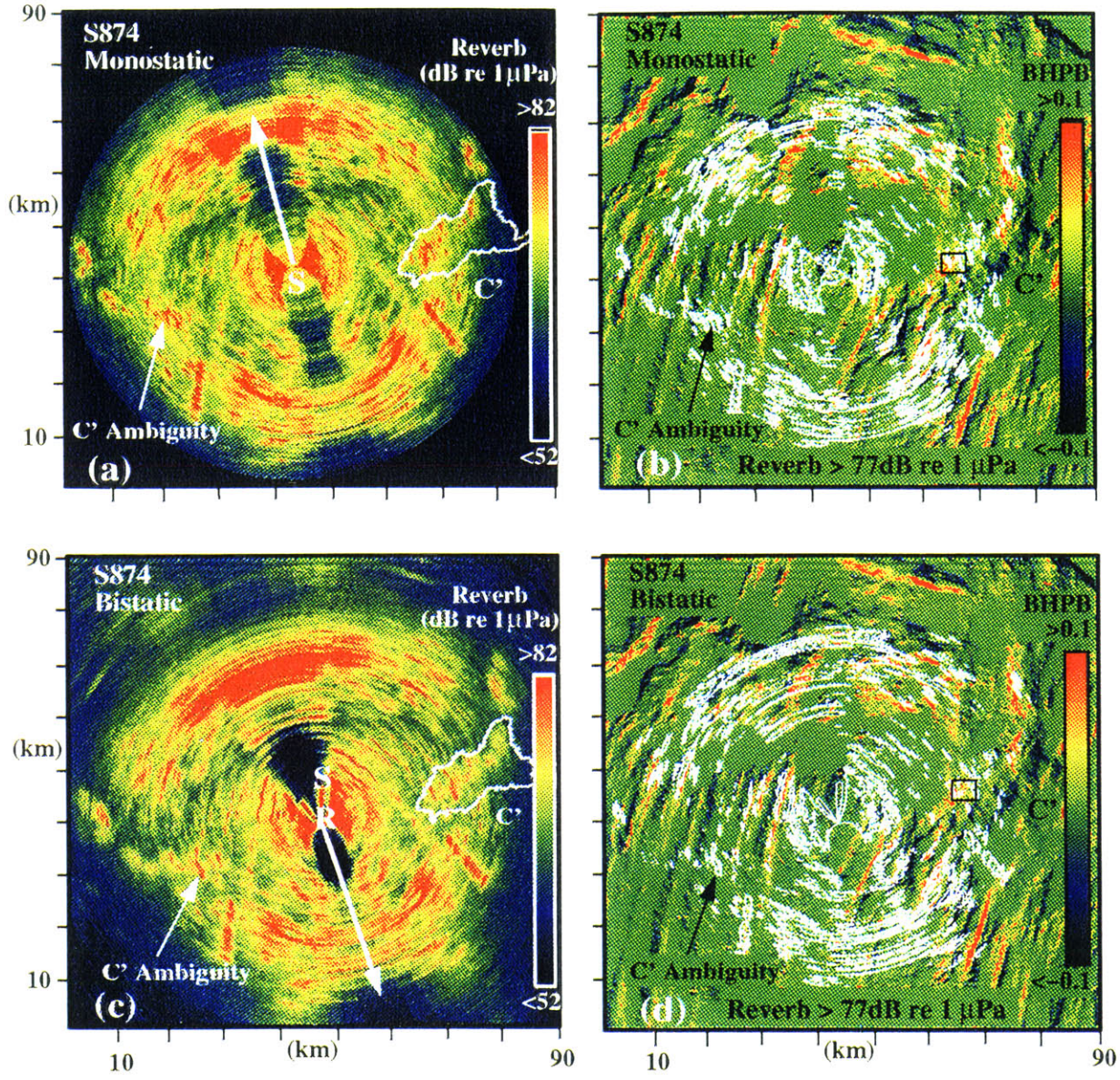

Figure 5–5: Wide–area images of monostatic and bistatic reverberation measured for 200–255 Hz LFM S874. (a) Monostatic reverberation chart showing symmetry about the array axis for Cory heading at 345^0. (b) Contours of high level backscatter, overlain on the BHBP, coregister with major scarps on C' facing the source–receiver. (c) Bistatic reverberation chart showing circular symmetry about the Alliance's array heading at 162^0. (d) Contours of high level backscatter overlain on the BHPB.

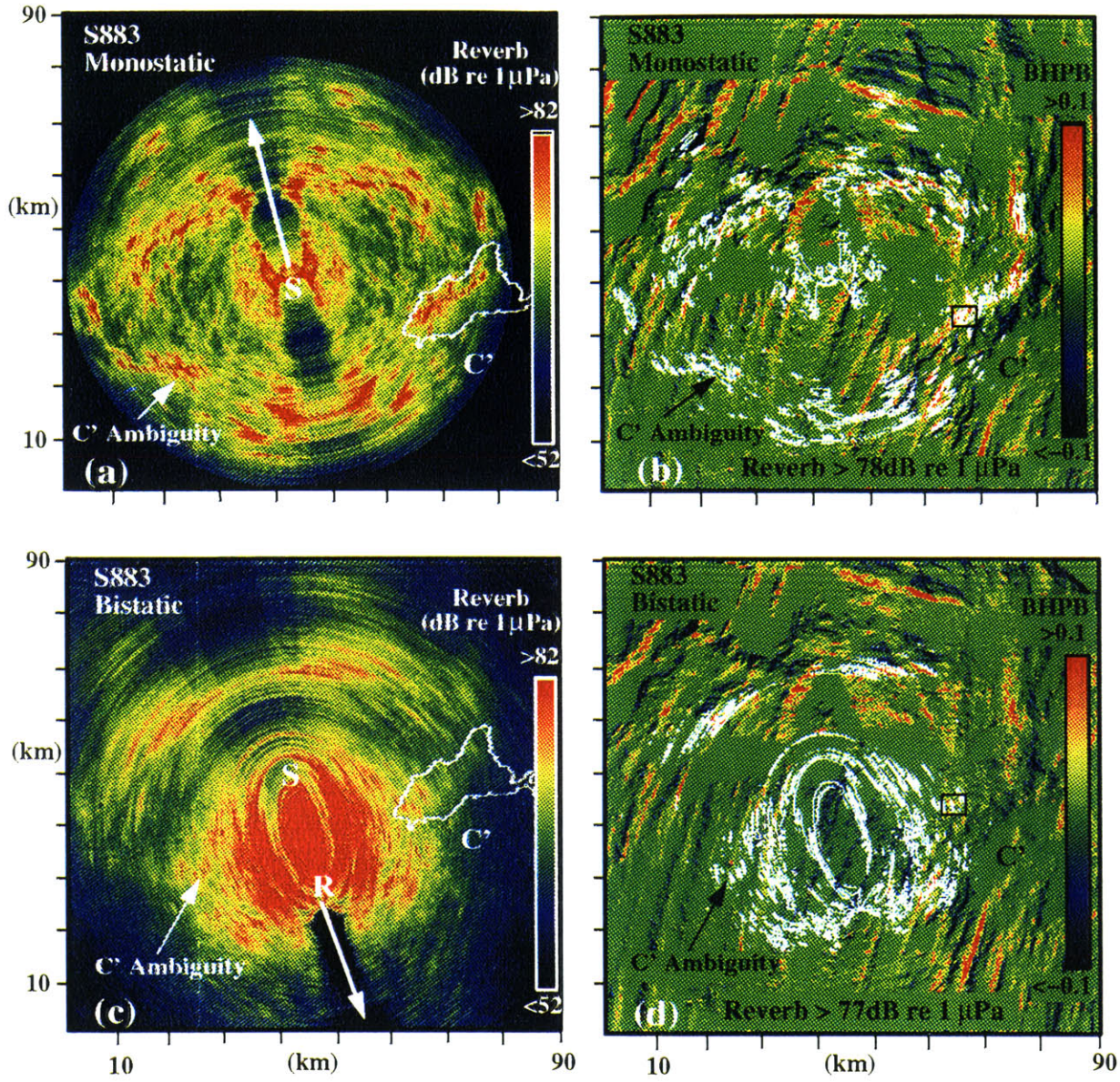

Figure 5–6: Wide–area images of monostatic and bistatic reverberation measured for 200–255 Hz LFM S883. (a) Monostatic reverberation chart showing symmetry about the array axis for Cory heading at 346^0. (b) Contours of high level backscatter, overlain on the BHBP, coregister with major scarps on C' facing the source–receiver. (c) Bistatic reverberation chart showing elliptical symmetry about the Alliance's array heading at 163^0. (d) Contours of high level backscatter overlain on the BHPB.

5.3 REVERBERATION MODELING AND SCATTERING STRENGTH ESTIMATION

Again, we assume a diffusely scattering surface at C' so that reverberation is modeled using Eq (6) as described in Section 4.3, except that the areal resolution is now changed to 200 x 200 m. The mean bi-azimuthal scattering strength (MBASS) at C' is estimated as in Eq (8) by taking the difference between the measured and modeled reverberation. Note that the grid size of 200-m is roughly 4 times of the towed-array range resolution (~ 50 m), and a factor of ¼ is multiplied to the outcome of spatial convolution, since the *normalized* range resolution, $dr=\frac{\Delta r}{\Delta x}$, was set to unity in our convolution program.

The correction factor of the discrete spatial convolution, as presented in Ref. [8], is expressed *dimensionlessly* as:

$$h_s(r,\theta)=\frac{\frac{r}{\Delta x}\beta(\theta)\frac{\Delta r}{\Delta x}}{\eta_s[m_0,n_0]}, \qquad (12)$$

where $r\beta(\theta)\Delta r$ denotes the annular sector of sonar resolution footprint, and $\eta_s[m_0,n_0]$ denotes the number of grid points per resolution area or integration number. This correction factor ensures that the modeled reverberation is computed independent of the grid size. In our Cartesian system, we denote $\Delta x=\Delta y$ since x and y grid increments are equal. Consequently, $\frac{r}{\Delta x}$ denotes the distance from bathymetry to the towed-array, while $\frac{\Delta r}{\Delta x}$ denotes the range resolution of sonar footprint, both normalized as *dimensionless* quantities.

To recast the modeled reverberation with reference to 1 m^2, a factor of $20*\log(\Delta x)$ is added to the result (in dB) after spatial convolution. For example, $\frac{\Delta r}{\Delta x}=10$ and $20*\log(\Delta x)\approx$ 14dB at 5-m resolution grid, while $\frac{\Delta r}{\Delta x}=0.25$ and $20*\log(\Delta x)\approx$ 46dB at 200-m resolution grid. For practical considerations, we set $\frac{\Delta r}{\Delta x}=1$ in our spatial convolution program during the 200-m resolution analysis, and the result was subsequently multiplied by a factor of ¼ to compensate for

the actual footprint range resolution of 50 m. Note that we can multiply this factor after convolution since Δr is a constant, unlike r and $\beta(\theta)$ which will affect the weighting in Eq. (12) depending on the distance and azimuth of local bathymetry to the towed-array. In which case, we assume the modeled reverberation is homogenous across the 200-m resolution, and reverberation integrated within the sonar resolution footprint is further assumed to be incoherently summed over the 200-m grid.

Figure 5-7 shows the surface projection and transmission loss charts computed, prior to spatial convolution, at the SW corner of C' for segment S229. Since the 3 x 2 km designated area cannot adequately display the spatial variations of transmission loss due to bathymetry-induced difference, a 9 x 6 km area is shown here to provide a broader pictorial view of the transmission loss variations. Specifically, the central white box in the figure indicates the scarp area designated for our study. The transmission losses from source to scattering patch, TL_i, and scattering patch to receiver, TL_r, are produced by sweeping the broadband incoherent TL maps across the bathymetry of C' at 200-m resolution. The surface projection terms from source to seafloor, C_i, and seafloor to receiver, C_r, are obtained by sweeping across the same area with the grazing angle maps produced by ray-tracing.

Figures 5-7(a) & (b) illustrate the surface projections of the SW corner (in dB) towards the source and receiver's locations. In segment S229, the RV Cory is located at the SW corner's broadside, while the RV Alliance is almost mid-way to the northern extreme of C'. Consequently, the SW corner scarp of C' projects a larger surface area towards the Cory's source than the Alliance's receiver. Note that an area of extremely low surface projection (dark blue color) is found at the right-hand side of Fig. 5-7(a), which is caused by the shadow zone of ray-tracing.

The transmission loss charts TL_i and TL_r in Figures 5-7(c) & (d) demonstrate the two different structures of broadband incoherent TL maps (given in Chapter 4) for source and receiver. Fig. 5-7(c) illustrates the well-structured main beam behavior of the broadband source TL map. The designated scarp area (in the central box) has a low transmission loss TL_i since it falls within the source's main beam, while the higher elevation above it suffers a large transmission loss due to the shadow zone of the source main beam's refractive path. Fig. 5-7(d) shows that the transmission loss from seafloor to the receiver TL_r has a relatively constant transmission loss across the site due to the little structure of broadband receiver TL map.

Consequently, TL_i is often found to be more dominant than TL_r in dictating the characteristics of the two-way TL across the SW corner of C'.

Figures 5-8(a) and (c) present two other versions of charted transmission loss, computed for segments S874 and S236 respectively. These two TL_i charts display some significant differences due to bathymetry-induced variations in their TL. While the source's main beam falls on the entire selected scarp in segment S229 (at a stand-off range of 26 km), it insonifies only the higher elevation of the scarp in segment S874 due to a closer stand-off range of 22 km. As a result, the modeled sum for S874, which is expressed as $-TL_i - TL_r + C_i + C_r$ in dB, predicts prominent echoes to be returned from the upper elevation of the SW corner scarp [Figure 5-8(b)].

In segment S236, the source's stand-off range is much further at roughly 30 km, and a large transmission loss is observed at the upper elevation of SW corner scarp since it falls into the shadow zone of the source's acoustics path. The lower elevation, on the other hand, is well insonified by the source's main beam. Hence, the modeled sum [Figure 5-8(d)] predicts the lower elevation to return prominent echoes, while its upper elevation has negligible returns due to large TL. Incidentally, it is observed that the modeled sum at C', though computed prior to spatial convolution, closely follows the characteristics of modeled reverberation which is subsequently computed.

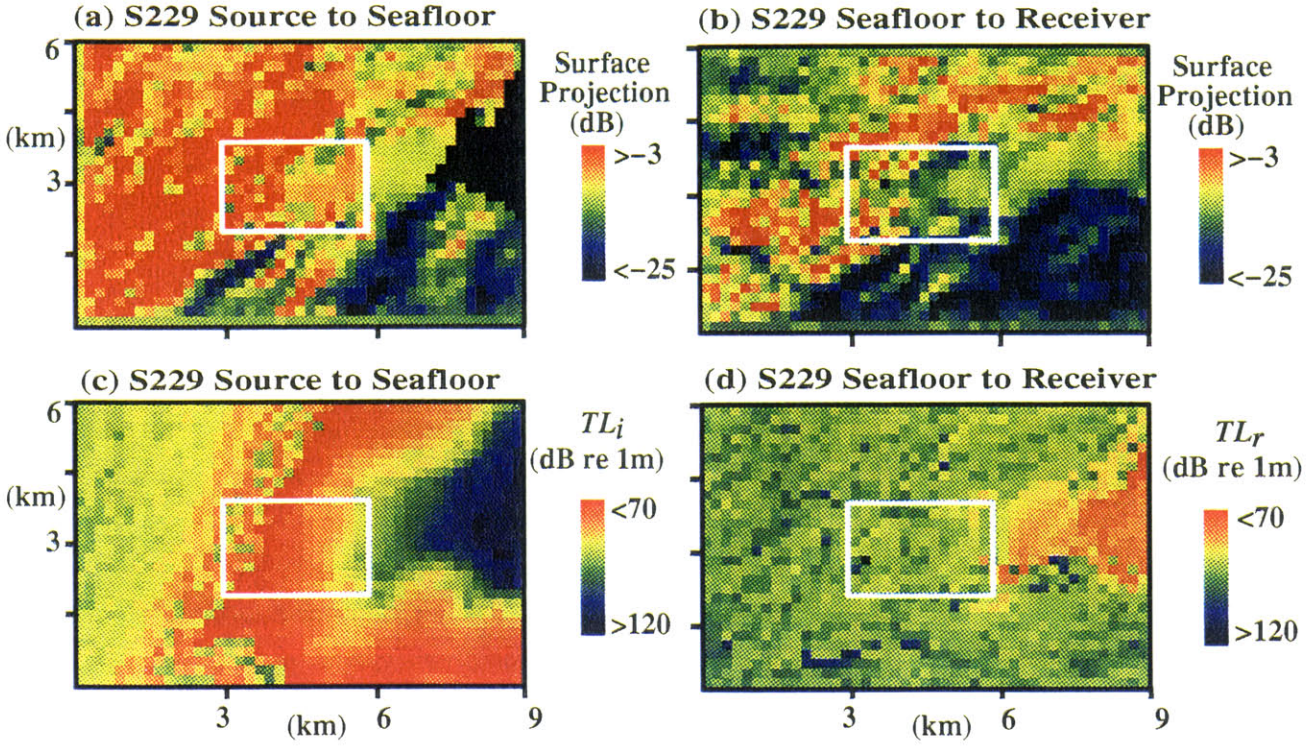

Figure 5–7: Surface projection and transmission loss charts computed over the SW corner of C' for S229 transmission. (a) Surface projection C_i =10log(cosθ_i) of bathymetry from source to seafloor using ray–trace. (b) Surface projection C_r =10log(cosθ_r) of bathymetry from seafloor to receiver using ray–trace. (c) Transmission loss TL_i from Cory's source to scattering patch. (d) Transmission loss TL_r from seafloor to Alliance's receiver.

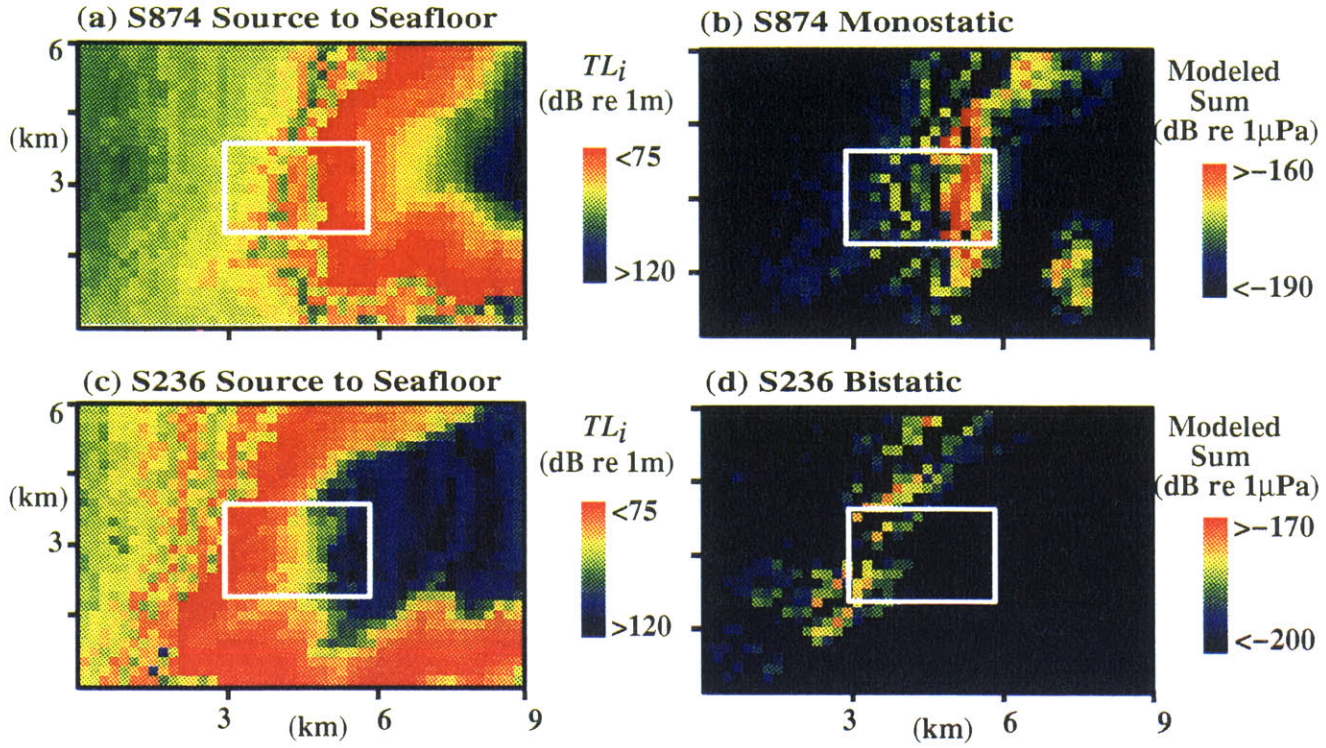

Figure 5–8: Transmission loss and modeled sum charts computed over the SW corner of C' for S874 and S236 transmission cycles. (a) Transmission loss TL_i from Cory source array to scattering patch for S874. (b) Modeled sum, which is expressed as $-TL_i - TL_r + C_i + C_r$ in dB, for S874. (c) Transmission loss TL_i from Cory source array to scattering patch in S236. (d) Modeled sum, which is expressed as $-TL_i - TL_r + C_i + C_r$ in dB, for S236.

5.4 COMPARISON BETWEEN MEASURED AND MODELED REVERBERATION

The measured and modeled reverberation charts for segments S229, S874 and S883 are presented in Figures 5-9 to 5-11 respectively. Generally, prominent echo returns from the SW corner scarp of C' show reasonably good agreement with the model in the monostatic reverberation charts. Across these three segments, the characteristic of reverberation changes predictably as a function of spatial variations of the transmission loss and surface projection. For example, the model predicts correctly that the lower elevation of the SW corner scarp at C' (near 3,800 m depth) will return prominent echoes in S229 and S883 monostatic receptions, while it predicts the higher elevation (near 3,600 m depth) to return prominent echoes in S874 monostatic reception. Indeed, the strongest echo returns measured over the SW corner scarp, indicated by the central box, agree well with the predictions for all three segments.

However, such a good visual correlation is often not found in the bistatic reverberation charts over the SW box. Frequently, the modeled bistatic reverberation predicts strong echo returns from a specific area of the scarp, while the measured reverberation appears more diffusely scattered over the entire scarp area. This inconsistency has been explained in our high resolution study of B'. Specifically, the signal-dependent speckle noise arising from statistical fluctuations of the scattered field is sufficient to mask out the predicted echo patterns. Since prominent echoes returned from the SW corner scarp are significantly higher than returns from neighboring bathymetry in both monostatic and bistatic receptions, there is no question that the scarp yields the dominant returns. However, within the scarp, the detailed structure of modeled bistatic returns is often measured with variations on the order of 5.6 dB standard deviation. Therefore, the expected echo patterns in the bistatic receptions are likely to be lost in the speckle noise.

There is also a possibility that the scarp area at C' might contain some small-scale features, which are under-resolved at 200-m resolution, responsible for the scattered echo patterns observed in the bistatic charts. However, we have found no distinct correlation between the scattered field and the bathymetry at large bistatic angles during the high resolution study of B'. Hence, the signal-dependent noise is believed to be the most probable cause for this discrepancy.

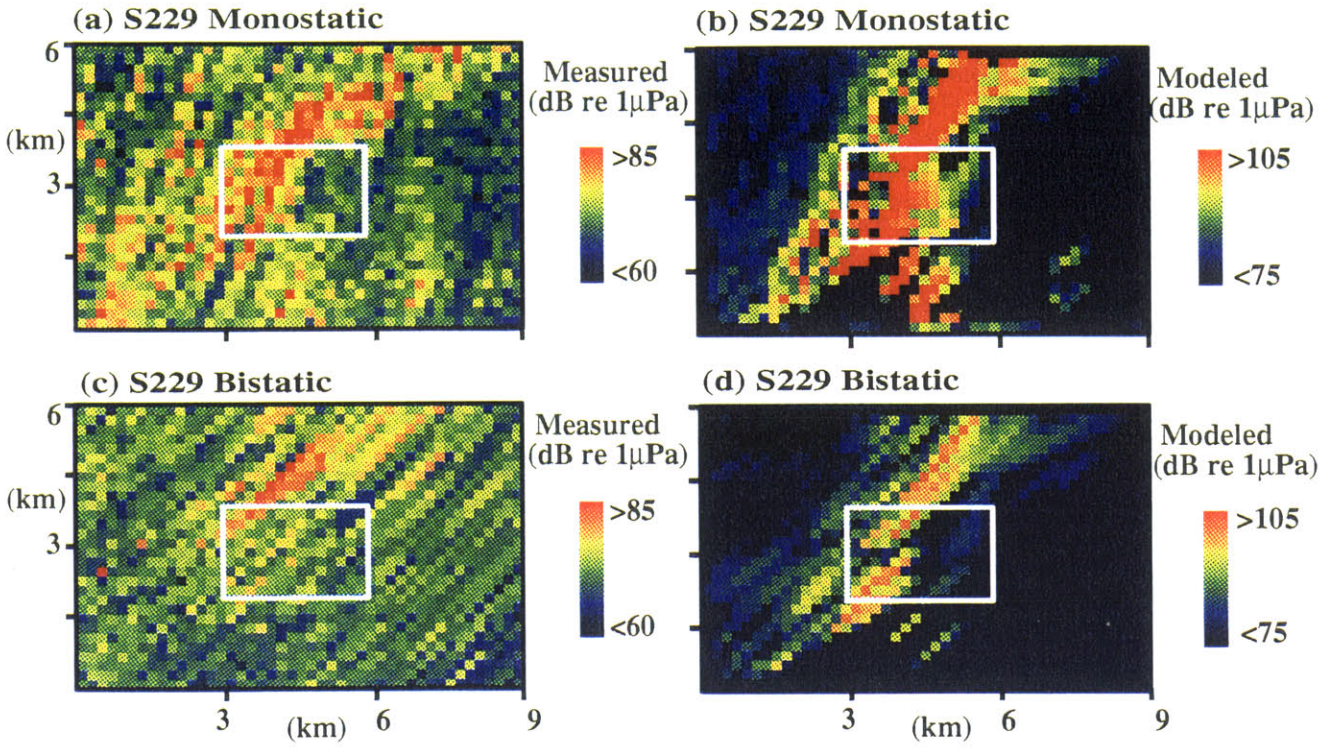

Figures 5–9: The 200–m resolution charts of the measured and modeled reverberation for S229 over the SW corner of C'. (a) Measured monostatic reverberation. (b) Model monostatic reverberation. (c) Measured bistatic reverberation. (d) Modeled bistatic reverberation. The central box indicates the 3 x 2 km area designated for our analysis.

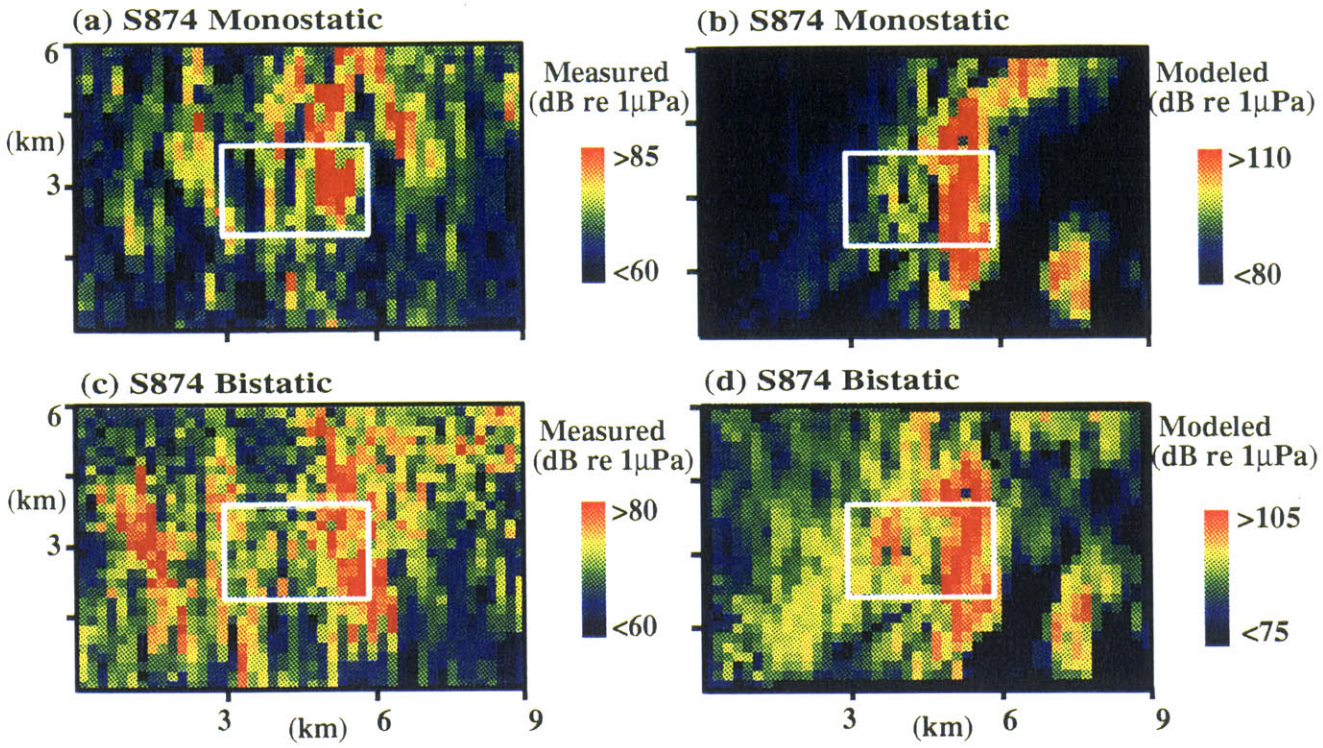

Figures 5–10: The 200–m resolution charts of the measured and modeled reverberation for S874 over the SW corner of C'. (a) Measured monostatic reverberation. (b) Model monostatic reverberation. (c) Measured bistatic reverberation. (d) Modeled bistatic reverberation. The central box indicates the 3 x 2 km area designated for our analysis.

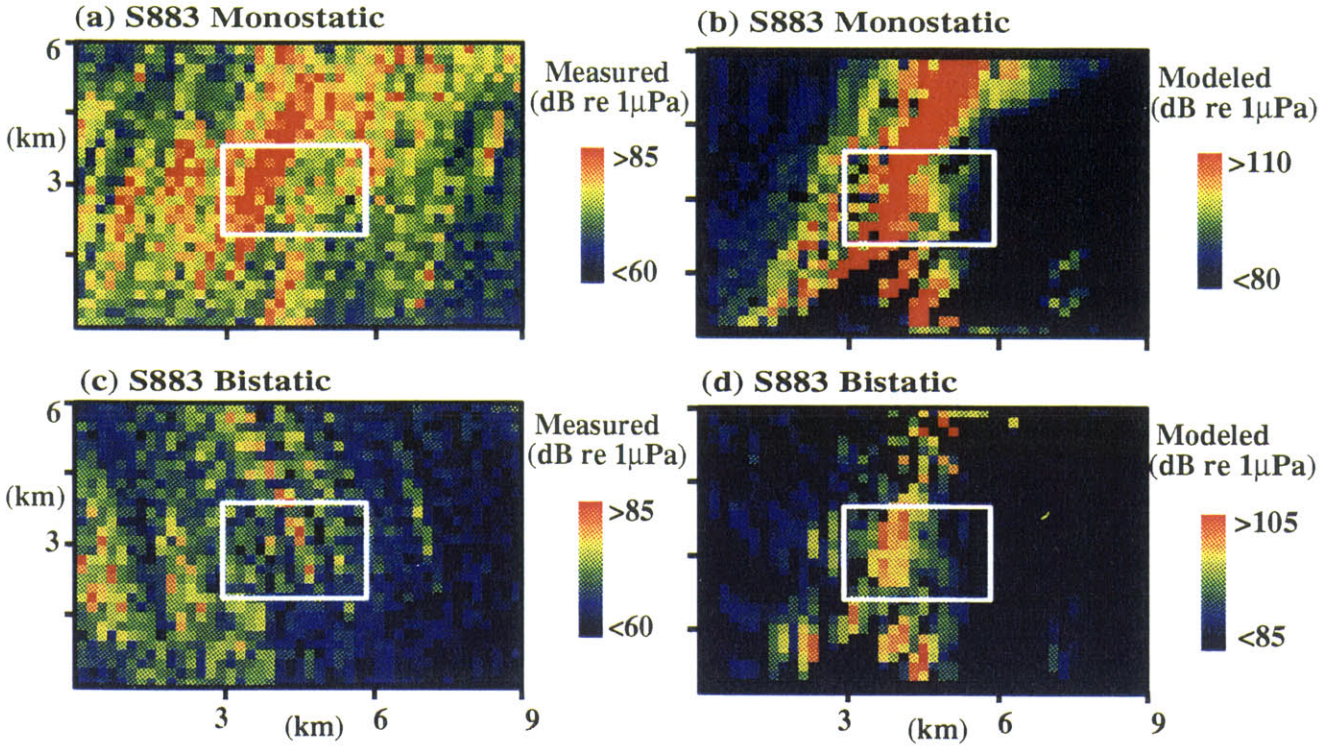

Figures 5–11: The 200–m resolution charts of the measured and modeled reverberation for S883 over the SW corner of C'. (a) Measured monostatic reverberation. (b) Model monostatic reverberation. (c) Measured bistatic reverberation. (d) Modeled bistatic reverberation. The central box indicates the 3 x 2 km area designated for our analysis.

5.6 MEAN BI-AZIMUTHAL SCATTERING STRENGTH

The mean measured and modeled reverberation level, at 200-m resolution, computed over the SW corner scarp of C', $< R(x, y|\Omega_i, \Omega_r) >_{A_{C'}}$ and $< R_M(x, y|\Omega_i, \Omega_r) >_{A_{C'}}$, are plotted as a function of receiver azimuth Ω_r in Fig. 5-12(a) & (b), together with their standard deviations $\sigma_{A_{C'}}\{R(x, y)\}$ and $\sigma_{A_{C'}}\{R_M(x, y)\}$. The subscript $A_{C'}$, which follows the same notation used in the B' study, indicates that the measured and modeled reverberation are averaged over an area A, namely the SW corner scarp of C'. A full bi-azimuthal description of these parameters, with respect to source and receiver azimuths, can be regained by referring to the source-receiver location pairs as shown in Figure 5-3.

The mean measured reverberation curve, in Fig. 5-12(a), shows a remarkably flat behavior across the receiver azimuths, with standard deviations of roughly 5 dB. These variations fall within the 5.6 dB standard deviation of speckle noise, and hence predicted echo patterns may be buried in these measurements. Compared to the B' reverberation curves, the mean value of C' curve is found, on average, to be lower by roughly 2 dB. In Fig. 5-12(b), the mean modeled reverberation curve displays a relative flat behavior, except for the extreme receiver azimuths, $\Omega_r < -60^0$, where a roughly 10 dB roll off is observed. This behavior can be explained by examining the surface projection and two-way transmission loss terms prior to spatial convolution.

Figure 5-13(a) illustrates the mean surface projection $< C_i(x, y|\Omega_i, \Omega_r) + C_r(x, y|\Omega_i, \Omega_r) >_{A_{C'}}$ plotted as a function of receiver azimuth Ω_r. A regular concave curve is observed with standard deviations of roughly 6 dB across the receiver azimuths. The mean value peaks at -15 dB near the origin, and gradually rolls off to roughly -20 dB at the two extremes. This concave behavior is expected since we have intentionally selected the scarp area at C' with its broadside facing towards the center of *Easternstar* ship tracks. Thus, the receiver azimuth at 0^0, which corresponds to the RV Cory's location at the center of star-shaped tracks, yields a higher surface projection than the extreme receiver azimuths.

Figure 5-13(b) shows the two-way transmission loss $< TL_i(x, y|\Omega_i, \Omega_r) + TL_r(x, y|\Omega_i, \Omega_r) >_{A_{C'}}$ plotted as a function of receiver azimuth Ω_r. The mean two-way TL curve is relatively flat across the receiver azimuths, except for $\Omega_r < -60^0$ where

the curve rises up by roughly 10 dB. Large two-way TL occurs at these extreme azimuths because the RV Cory and Alliance are furthest away from the SW corner scarp in these segments (indicated by alphabets A,B & C in Figure 5-1). In addition, the RV Cory is roughly 30-33 km away from the designated scarp area, and it is therefore close to the ½ CZ where the source's acoustic refractive path bends at a minimum depth near 3,800 m. As a result, the upper elevation of the C' scarp (>3,800 m depth) lies in the shadow zone above the source's main beam, and hence suffers a large transmission loss.

The lower elevation of C' scarp (~ 3,800 m depth), however, has a low transmission loss since it is well insonified by the source's main beam. Consequently, a wide spread of transmission loss occurs across this scarp area, which leads to large standard deviations in the two-way TL curve for $\Omega_r < -60^0$. In the other data segments, the RV Cory is located less than 27 km from the SW corner. At this stand-off range, the entire scarp area falls below the shadow zone of the source's acoustic path, and hence a low transmission loss is predicted uniformly across all other receiver azimuths.

The mean bi-azimuthal scattering strength (MBASS) estimated over the C' scarp, $< \hat{\tilde{S}}(x, y|\Omega_i, \Omega_r) >_{A_{C'}}$, is plotted as a function of receiver azimuth Ω_r along with its standard deviation $\sigma_{A_{C'}}\{\hat{\tilde{S}}(x, y)\}$ in Figure 5-14. The MBASS curve displays a relatively flat behavior, except for $\Omega_r < -60^0$. The roll-off observed at these extreme azimuths can be explained by the same behavior of the two-way TL and modeled reverberation curves. A mean of roughly -13 dB is obtained by averaging the MBASS curve across the entire receiver azimuths.

In summary, our results have shown that the measured reverberation of the C' scarp is spatially homogenous across the receiver azimuths within +/-90^0. This behavior is similar to the bistatic reverberation measured over the two B' scarps. The modeled and measured reverberation curves have also displayed similar characteristics, except for $\Omega_r < -60^0$ where our model predicts stronger shadowing effect than found in the data. All the data segments have been inspected to ensure that the left-right ambiguity of towed-array was not a problem for our analysis. Two such examples of the wide-area reverberation images for S236 (Ω_r ~-75^0) and S239 (Ω_r ~-80^0) are presented in Figure 5-15 to show that the discrepancy observed at $\Omega_r < -60^0$ is not caused by the left-right ambiguity errors.

More importantly, a constant line of -13 dB can be drawn across the entire receiver azimuths for the MBASS curve, and still falls within all the error bars of roughly 10 dB. This leads to the suggestion that the bi-azimuthal scattering function of the C' scarp is spatially homogenous, and roughly equals to the constant of -13dB +/- 10dB. Our comparison on the measured and modeled reverberation of this C' scarp has also supported the previous finding in the B' study that spatial variations in the transmission loss and projected area are dominant factors in yielding the variations of long-range reverberation.

Moreover, it is noted that the surface projection of the C' scarp is typically 6-10 dB lower than the surface projections computed over the two B' scarps using 5-m resolution bathymetry data. This is partly because the slope gradients of bathymetry are often under-estimated in the 200-m resolution sampling. Hence, the scattering strength difference between B' (evaluated at 5-m resolution) and C' (evaluated at 200-m resolution) is likely to be caused by the surface projection difference arising from the two resolutions of bathymetry data used. As such, we have also measured the bi-azimuthal scattering distribution of the B' scarps using 200-m resolution bathymetry data, which will be discussed in the next chapter, so as to compare the scattering characteristics of B' and C' appropriately.

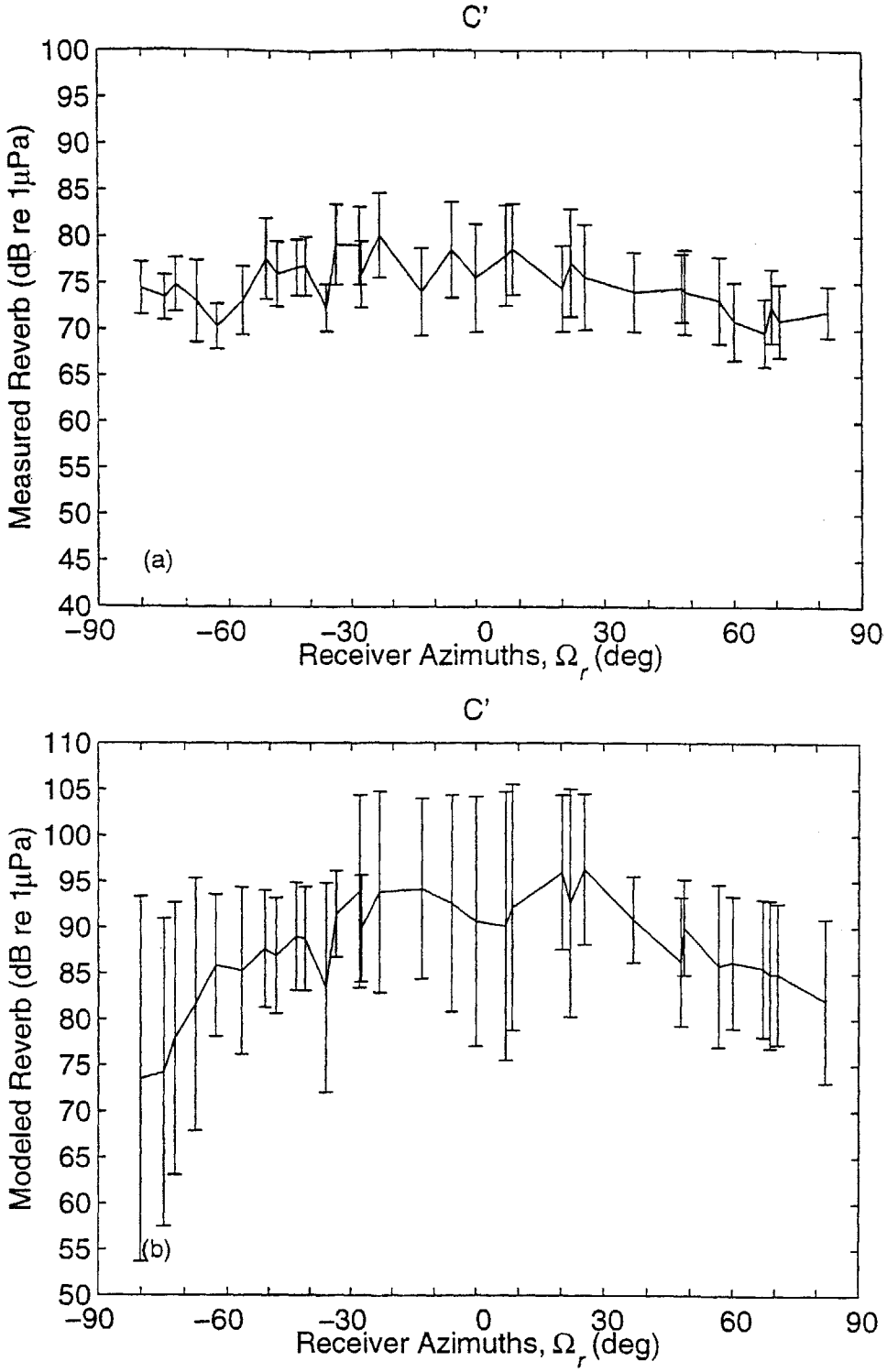

Figure 5-12: (a) The mean reverberation level measured over the SW corner scarp of C', $< R(x, y|\Omega_i, \Omega_r) >_{A_{C'}}$ and (b) the modeled reverberation $< R_M(x, y|\Omega_i, \Omega_r) >_{A_{C'}}$ as a function of receiver azimuth Ω_r, with their respective standard deviations $\sigma_{A_{C'}}\{R(x, y)\}$ and $\sigma_{A_{C'}}\{R_M(x, y)\}$.

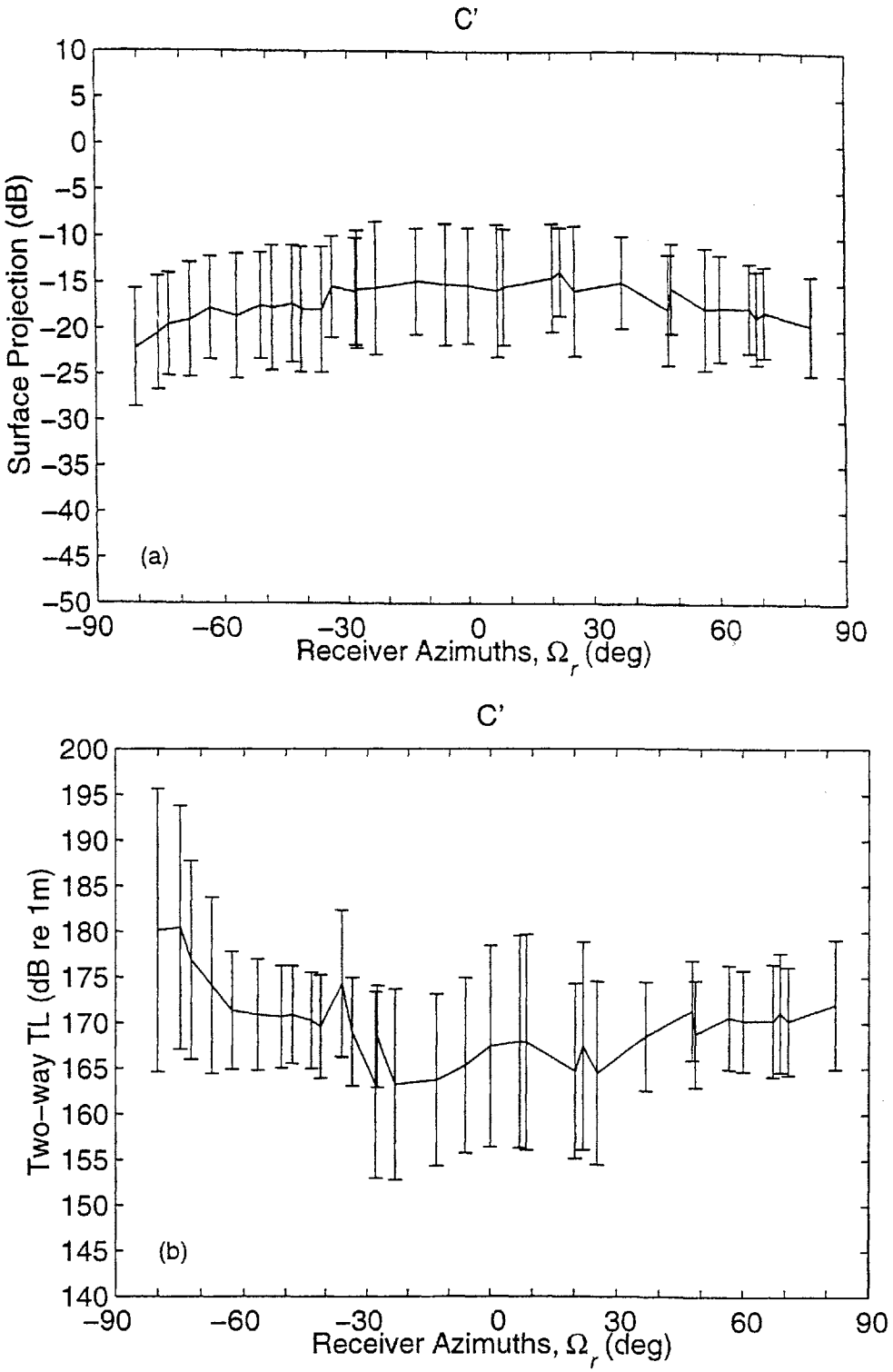

Figure 5-13: (a) The mean surface projection $< C_i(x, y|\Omega_i, \Omega_r) + C_r(x, y|\Omega_i, \Omega_r) >_{A_{C'}}$, and (b) the mean 2-way transmission loss $< TL_i(x, y|\Omega_i, \Omega_r) + TL_r(x, y|\Omega_i, \Omega_r) >_{A_{C'}}$ computed over the SW corner scarp of C' as a function of receiver azimuth Ω_r.

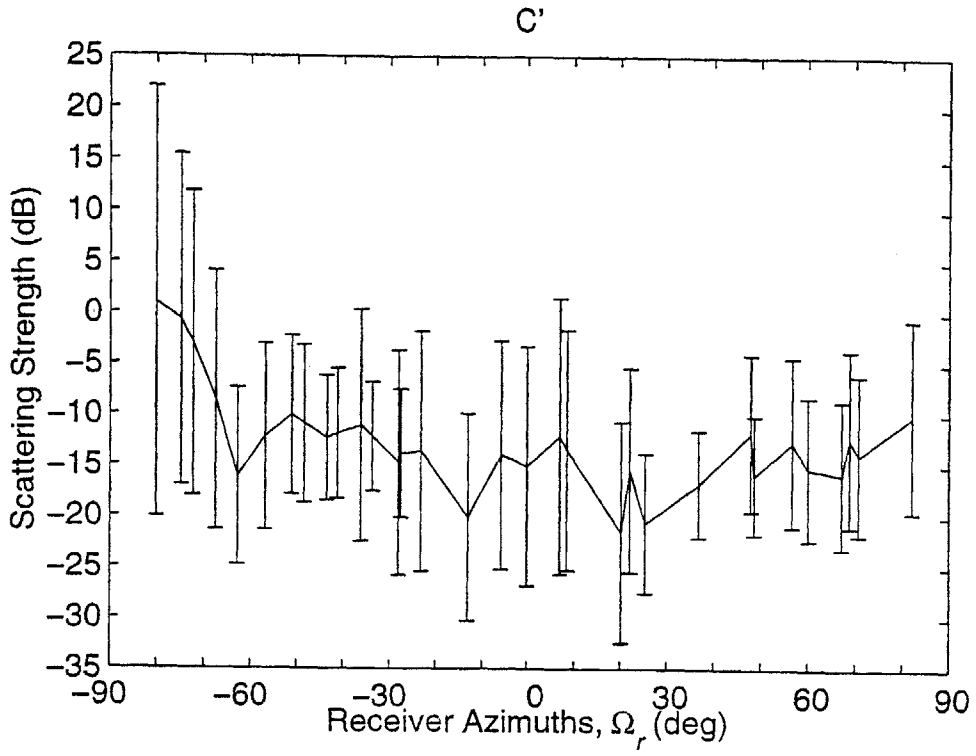

Figure 5-14: The MBASS curve estimated over the SW corner scarp of C' $< \hat{\tilde{S}}(x, y|\Omega_i, \Omega_r) >_{A_{C'}}$ as a function of receiver azimuth Ω_r along with its standard deviation $\sigma_{A_{C'}}\{\hat{\tilde{S}}(x, y)\}$.

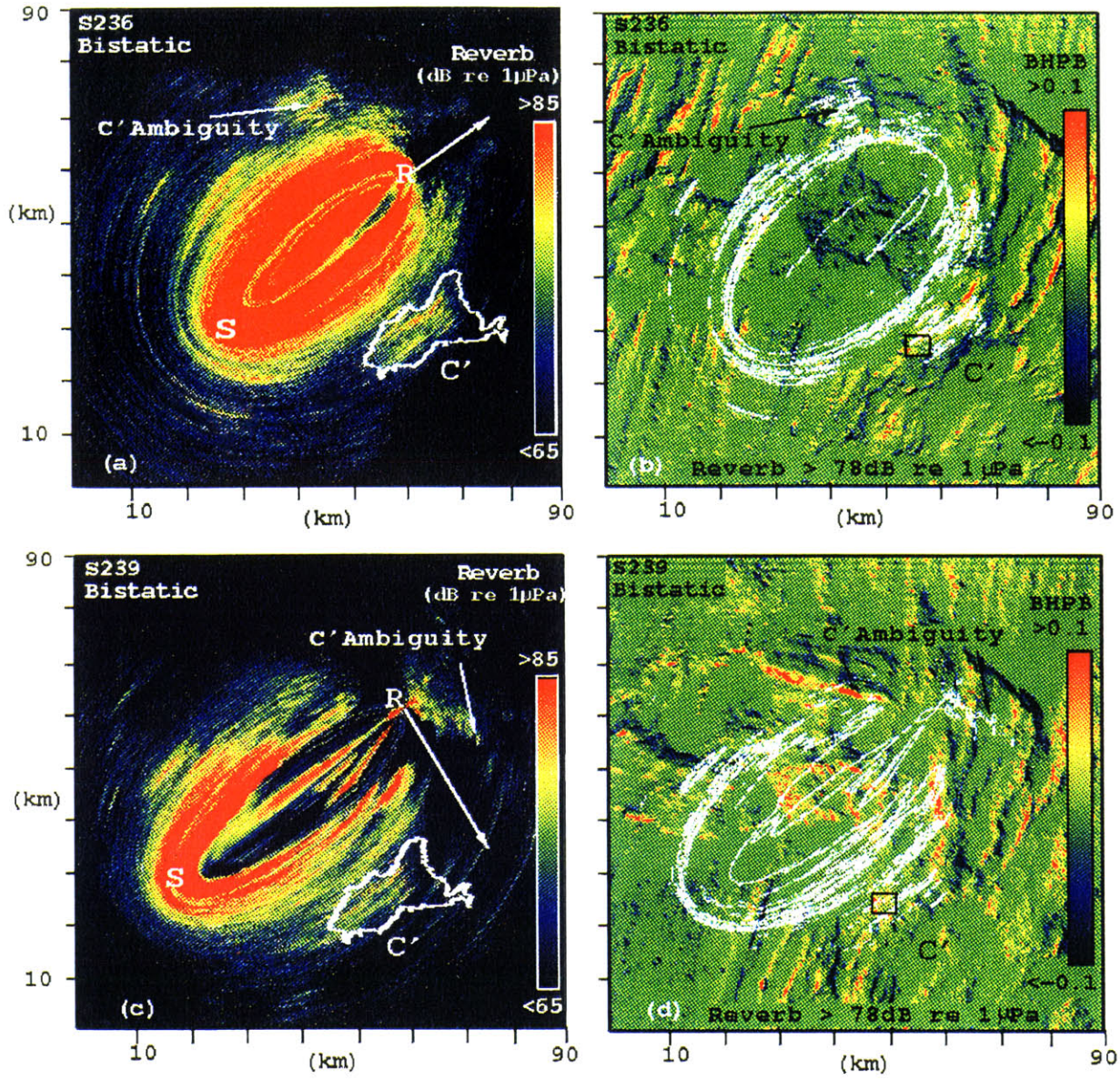

Figure 5–15: Wide–area images of bistatic reverberation measured for 200–255 Hz LFM S236 and S239. (a) Bistatic reverberation chart showing elliptical symmetry about the Allaince's array heading at 60^0 for S236. (b) Contours of high level backscatter overlain on the BHBP for S236. (c) Bistatic reverberation chart showing asymmetry about the Alliance's array heading at 147^0 for S239. (d) Contours of high level backscatter overlain on the BHPB for S239. The SW box of C' was not charted with any false ambiguities due to the towed–array.

6 COMPARISON OF THE BI-AZIMUITHAL SCATTERING DISTRIBUTIONS OF B' AND C'

Since only 200-m resolution bathymetry data is available at C', we need to measure the bi-azimuthal scattering distribution of B' at the same resolution in order to compare their scattering characteristics appropriately. In Section 6.1, we compare the similarities and differences associated with the scattering strengths of the two B' scarps estimated at 5-m and 200-m resolutions, from which we can determine the effects of reduced bathymetry resolution on the seafloor's scattering strength estimation. In Section 6.2, the bistatic scattering characteristics of the *outside corner* B' and *inside corner* C' are compared by examining their mean bi-azimuthal scattering strengths, measured and modeled reverberation evaluated at 200-m resolution.

6.1 COMPARISON OF THE BI-AZIMUTHAL SCATTERING DISTRIBUTIONS OF B' AT TWO DIFFERENT RESOLUTIONS

First, the areas designating the upper and lower scarps at B' in the high resolution study are mapped, point-to-point, into a 200-m grid chart. The resultant chart of the two scarps at 200-m resolution is plotted in Figure 6-1(a), while the original 5-m resolution data are overlain within the 200-m resolution contours in Figure 6-1(b) to confirm that the mapping has been carried out correctly.

This 8 x 9 km area is then extracted from the wide-area, 200-m grid bathymetry chart, with reference to its location at (26.54676N, -48.11122W). The two-way TL and surface projection, across the resultant 200-m grid bathymetry area, are computed by the same approach used in the B' high resolution study as described in Section 4-4. Ray tracing is used to compute the two-way travel time, and reverberation images are produced by the bistatic mapping procedure as mentioned in Chapter 3. The corresponding 200-m and 5-m resolution reverberation charts are compared, eg. S435 shown in Figures 6-4 and 4-10, to ensure that the mapping is done appropriately.

Shaded relief plots for a section of the upper scarp are plotted at 5-m and 200-m resolutions in Figures 6-2 (a) and (b) respectively. In the 5-m resolution plot, steep slopes and small-scale anomalies, such as canyons and gullies, are clearly observed along the upper scarp. In the 200-m resolution plot, the upper scarp appears relatively flat over the sonar resolution footprint, and small-scale anomalies are not properly resolved. There is a good possibility that, during the 200-m resolution hydrosweep survey, the upper scarp's slope gradient was averaged across the upper crest and plateau areas due to under-sampling. Consequently, the slope gradients of the two scarps are under-estimated in the 200-m resolution bathymetric data set.

Figures 6-3(a) and (b) illustrate the surface projection, $C_i = 10\log(\cos\theta_i)$, computed over the designated 8 x 9 km area using the two resolutions of bathymetry data for S435 transmission. Since the upper and lower scarps are typically inclined in the vertical at 50^0-90^0, their surface projections in the 5-m resolution chart appear mostly in red color, corresponding to values close to 0 dB as expected. On the other hand, the surface projections of the two scarps in the 200-m resolution chart are well below 0 dB due to their under-estimated slope gradients at 20^0-30^0. The plateau areas, which appear flat with respect to the incident rays at low grazing angles, are registered with extremely low surface projections. Figures 6.3(c) and (d) present the two-way transmission loss charted over the same site for S435 monostatic reception at 200-m and 5-m resolutions respectively. These two charts illustrate that the transmission losses across the entire area are generally similar in their magnitudes, despite the different resolutions of bathymetry data used.

Similar to the 5-m resolution charts, prominent echo returns from the two B' scarps reveal a good correlation between the measured and modeled reverberation at 200-m resolution. As an example, the measured and modeled reverberation charts obtained for segment S435 using 200-m resolution data are presented in Figure 6-4. While the model predicts strong lineated echoes to be returned along the scarp axes in the monostatic reception [Fig. 6-4(b)], a speckle-like echo pattern across the two scarps is expected in the corresponding bistatic reception [Fig. 6-4(d)]. Indeed, the general character of prominent echo returns measured over the two scarps, as shown in Fig. 6-4 (a) & (c), agree well with these predictions.

While a *smooth* echo pattern is often predicted in the 5-m resolution charts (see Fig. 4-10), the modeled reverberation are found more discretely charted over the two scarps in the 200-m resolution charts. This is partly due to the less effective smoothing of the spatial convolution in the 200-m resolution grid system. Since the 200-m grid size already exceeds the towed-array range resolution of ~50 m, there is no data averaging over the range resolution when performing the spatial convolution at 200-m resolution. Consequently, the modeled reverberation over the two scarps appear with more fluctuations in the 200-m resolution charts.

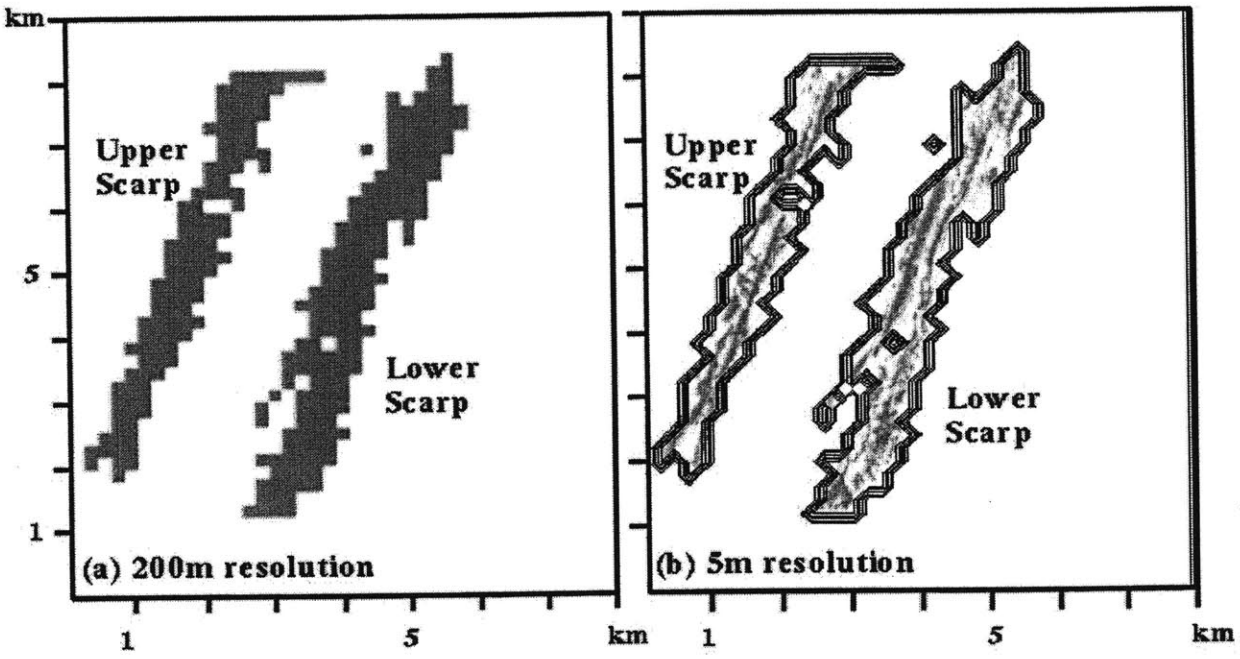

Figure 6–1: (a) Contours of the upper and lower scarps designated in the 200–m resolution study, which is mapped point–to–point from the 5–m resolution contours used in the high resolution study. (b) The 5–m resolution chart is overlaid with the outline of resultant 200–m resolution contours to confirm that the translation has been carried out correctly.

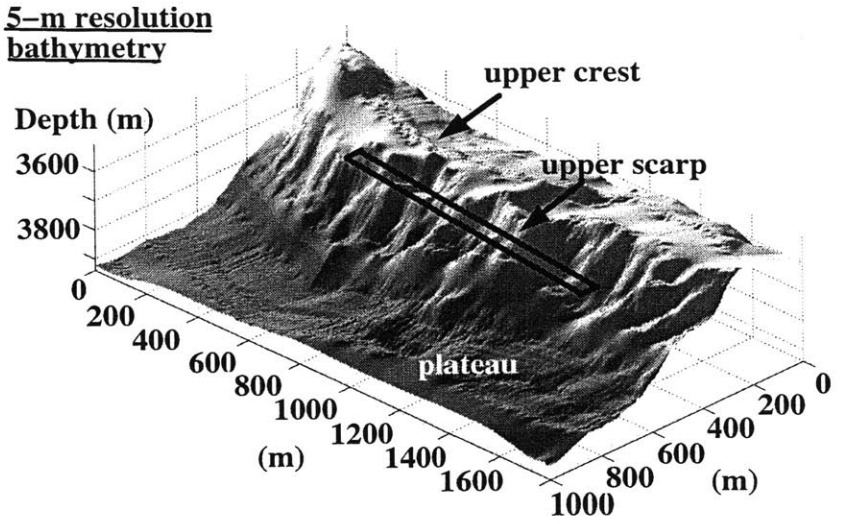

(a)

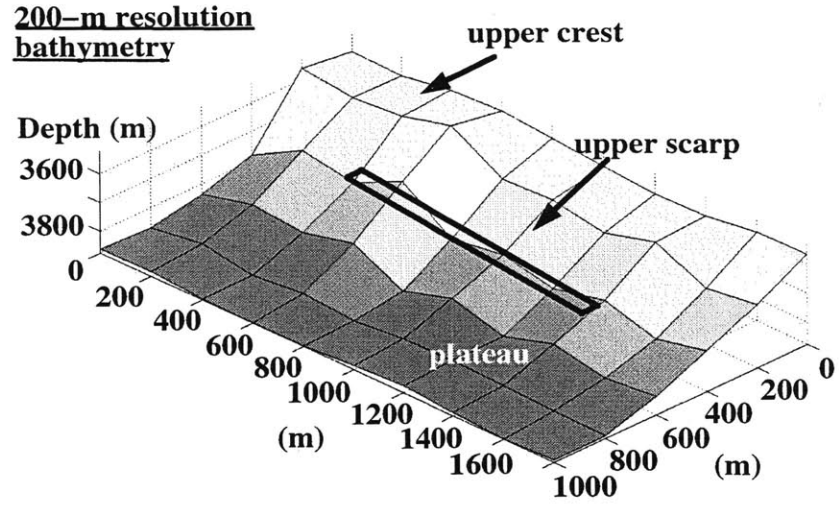

(b)

Figure 6–2: Shaded relief plots for a section of the upper scarp at (a) 5–m and (b) 200–m resolutions, which are overlain with a sonar resolution footprint for monostatic reception at 1/2 CZ with receiving array parallel to ridge–axis. The slope gradients are under–estimated in the 200–m resolution bathymetry data, and small–scale features along the scarps, such as canyons and gullies, are not properly resolved at 200–m resolution.

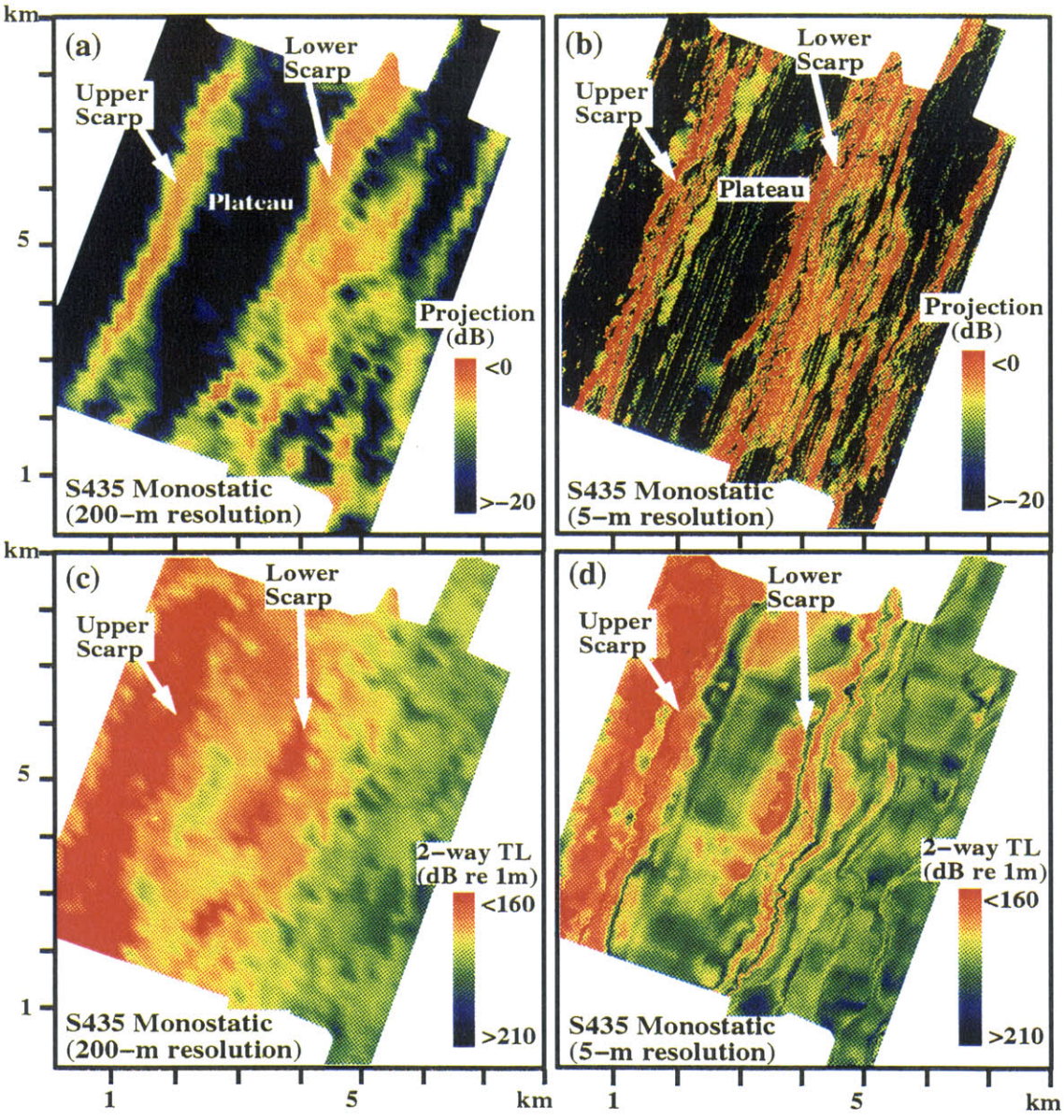

Figure 6–3: Surface projection, $10\log(\cos\theta_i)$, computed over the upper and lower scarps using (a) 5–m and (b) 200–m resolution bathymetry data. An example of S435 monostatic transmission is shown to illustrate that the two steep scarps of B' have lower projections at 200–m resolution due to under–resolved slope gradients. Figures (c) and (d) show the two–way transmission loss computed over the same site for 200–m and 5–m resolutions respectively. Their transmission losses across the area are found to be similar in their magnitudes.

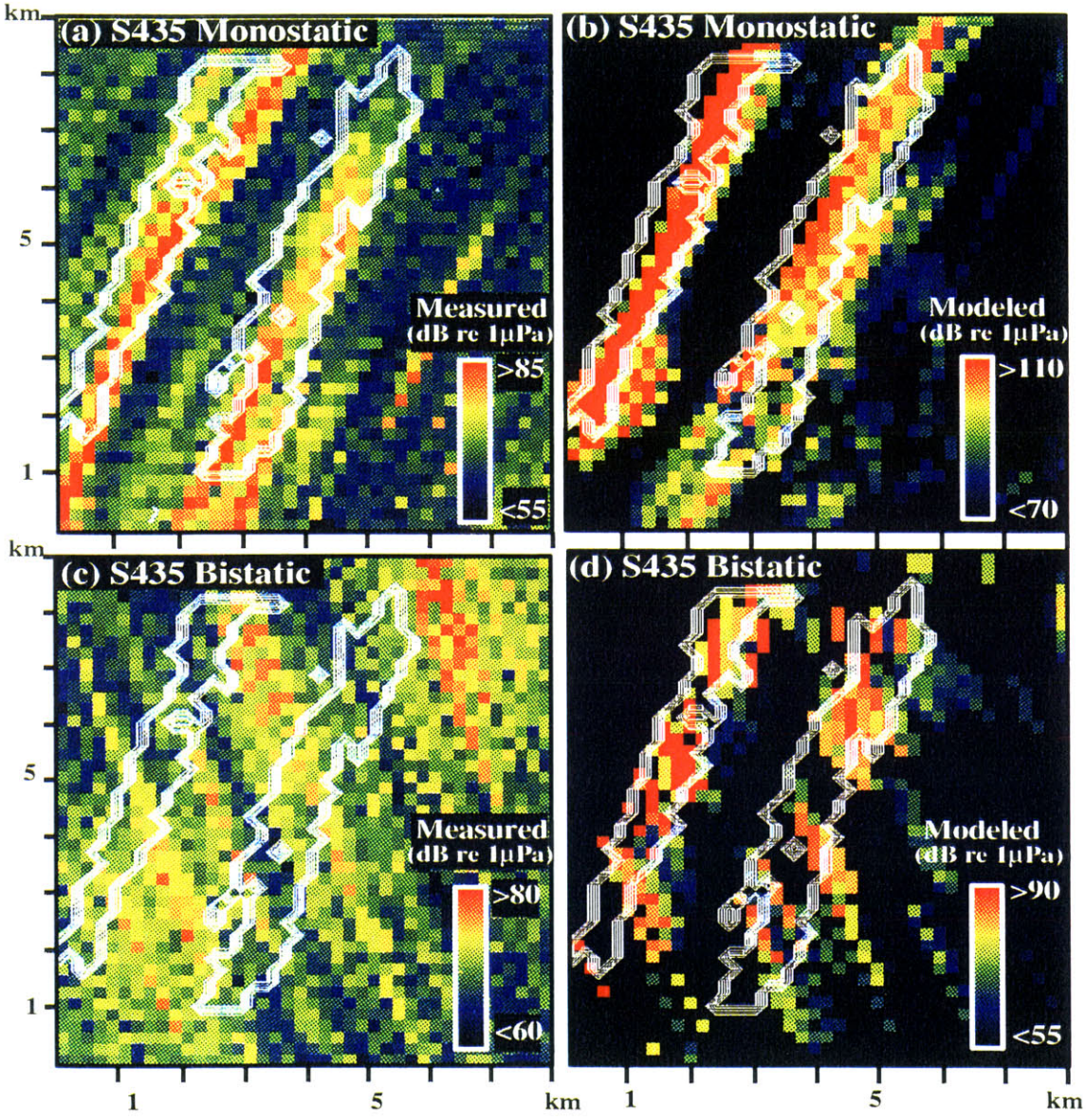

Figures 6–4: The 200–m resolution charts of monostatic and bistatic measured and modeled reverberation for S435 over the upper and lower scarp contours. (a) Measured monostatic reverberation. (b) Model monostatic reverberation. (c) Measured bistatic reverberation. (d) Modeled bistatic reverberation.

The mean reverberation levels, at 200-m resolution, measured over the upper scarp $< R(x, y|\Omega_i, \Omega_r) >_{A_{up}}$ and the lower scarp $< R(x, y|\Omega_i, \Omega_r) >_{A_{low}}$ are plotted as a function of receiver azimuth Ω_r in Figure 6-5 (a) & (b), together with their standard deviations $\sigma_{A_{up}}\{R(x, y)\}$, $\sigma_{A_{low}}\{R(x, y)\}$. For comparison purpose, the mean values of the 5-m resolution curves are shown in dotted lines. The 200-m resolution reverberation curves are remarkably flat across the receiver azimuths, and their respective mean values are closely matched to the 5-m resolution measurements.

The mean reverberation levels modeled over the two scarps, $< R_M(x, y|\Omega_i, \Omega_r) >_{A_{up}}$ and $< R_M(x, y|\Omega_i, \Omega_r) >_{A_{low}}$, are plotted as a function of receiver azimuth Ω_r in Figure 6-6 (a) & (b). Both the modeled reverberation curves, at 200-m resolution, follow the same behavior as their respective 5-m resolution curves across the +/-90^0 receiver azimuths. While the modeled mean across the upper scarp fluctuates within $|\Omega_r| < 30^0$, the modeled mean across the lower scarp displays a slight concave behavior, with the peak value within $|\Omega_r| < 30^0$ and rolling off by ~10 dB towards the extreme azimuths.

Figure 6-7 shows the mean surface projection terms, $< C_i(x, y|\Omega_i, \Omega_r) + C_r(x, y|\Omega_i, \Omega_r) >_{A_{up}}$ and $< C_i(x, y|\Omega_i, \Omega_r) + C_r(x, y|\Omega_i, \Omega_r) >_{A_{low}}$, computed over the upper and lower scarps as a function of receiver azimuth Ω_r. The two surface projection curves, at 200-m resolution, exhibit the same concave behavior as the 5-m resolution curves, with their peak values near the origin. However, the mean values of these 200-m resolution curves are found to be roughly 6-8 dB lower than their respective mean surface projections at 5-m resolution. One can easily deduce that this offset is caused by the under-estimation of slope gradients in the 200-m resolution bathymetry data.

The mean 2-way transmission loss, $< TL_i(x, y|\Omega_i, \Omega_r) + TL_r(x, y|\Omega_i, \Omega_r) >_{A_{up}}$ and $< TL_i(x, y|\Omega_i, \Omega_r) + TL_r(x, y|\Omega_i, \Omega_r) >_{A_{low}}$, are plotted as a function of receiver azimuth Ω_r in Figure 6-8. These two curves display an exceptionally good agreement with the 5-m resolution curves, both in terms of their mean values and standard deviations at each receiver azimuth. This observation seems to suggest that the transmission loss is independent on the two different resolutions of bathymetry data used.

The mean bi-azimuthal scattering strengths (MBASS) estimated at 200-m resolution over the upper scarp $<\hat{\bar{S}}(x,y|\Omega_i,\Omega_r)>_{A_{up}}$ and lower scarp $<\hat{\bar{S}}(x,y|\Omega_i,\Omega_r)>_{A_{low}}$ are plotted as a function of receiver azimuth Ω_r in Figure 6-9, along with their standard deviations $\sigma_{A_{up}}\{\hat{\bar{S}}(x,y)\}$ and $\sigma_{A_{low}}\{\hat{\bar{S}}(x,y)\}$. These MBASS curves again display similar characteristics as the 5-m resolution curves. Compared to the 5-m resolution curves, a higher standard deviation is observed across the 200-m resolution curves since there is less effective smoothing of the data by spatial convolution over the sonar resolution footprint at 200-m resolution grid.

A mean value of roughly -9 dB is obtained by averaging the MBASS of the upper scarp across the +/-90^0 receiver azimuths, while a mean value of -13 dB is found by similarly averaging the lower scarp's curve. More importantly, a constant line of -11 dB can be drawn across the entire receiver azimuths for these two curves, and still falls within all the error bars. This behavior is *consistent* with the scattering characteristics of the two scarps evaluated at 5-m resolution previously. In view of these results, one may conclude that the mean bi-azimuthal scattering strengths of the two scarps are identical, and both are spatially homogenous across the receiver azimuths within +/-90^0.

In particular, the mean bi-azimuthal scattering strengths of the two scarps, at 200-m resolution, are found to be roughly 6-8 dB higher than the results obtained at 5-m resolution. This scattering strength difference coincides with the difference of surface projected areas computed over the two resolutions of bathymetry data. The smaller surface projection obtained at 200-m resolution, which arises from the lower estimated slope gradients, has resulted a higher scattering strength estimation. This leads to the conclusion that the seafloor's scattering strength estimation has a *strong dependence* on the surface projection or slope gradient resolved by the supporting bathymetry data. In our study, insufficient sampling of the bathymetry has led to a higher scattering strength estimation by roughly an order of the surface projection difference, as compared to the previous estimation based on a fine resolution bathymetric dataset.

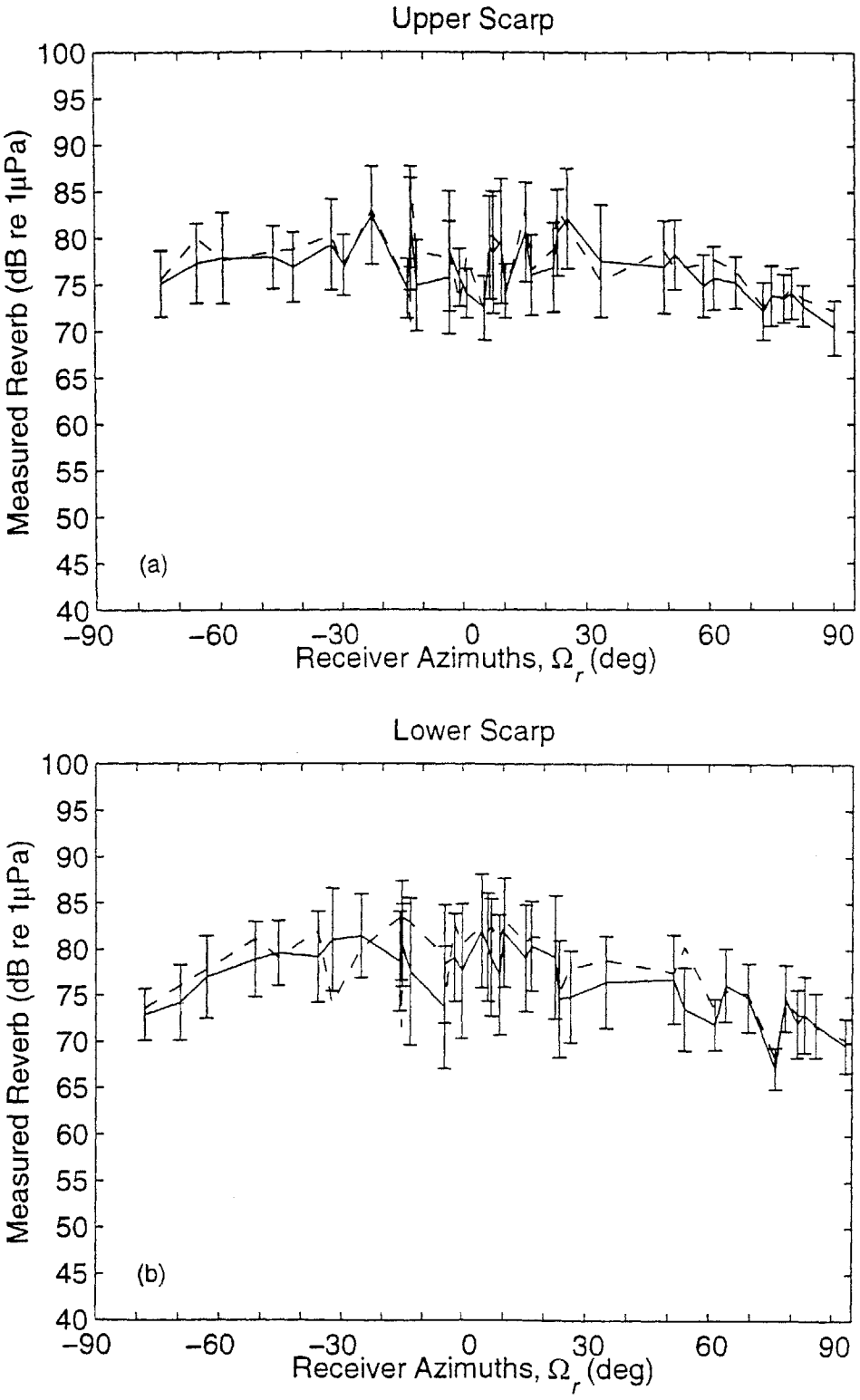

Figure 6-5: The mean reverberation level measured over (a) the upper scarp $< R(x, y|\Omega_i, \Omega_r) >_{A_{up}}$ and (b) the lower scarp $< R(x, y|\Omega_i, \Omega_r) >_{A_{low}}$ as a function of receiver azimuth Ω_r along with their respective standard deviations $\sigma_{A_{up}}\{R(x, y)\}$ and $\sigma_{A_{low}}\{R(x, y)\}$. Solid line denotes the 200-m resolution curve, and dashed line denotes the 5-m resolution curve.

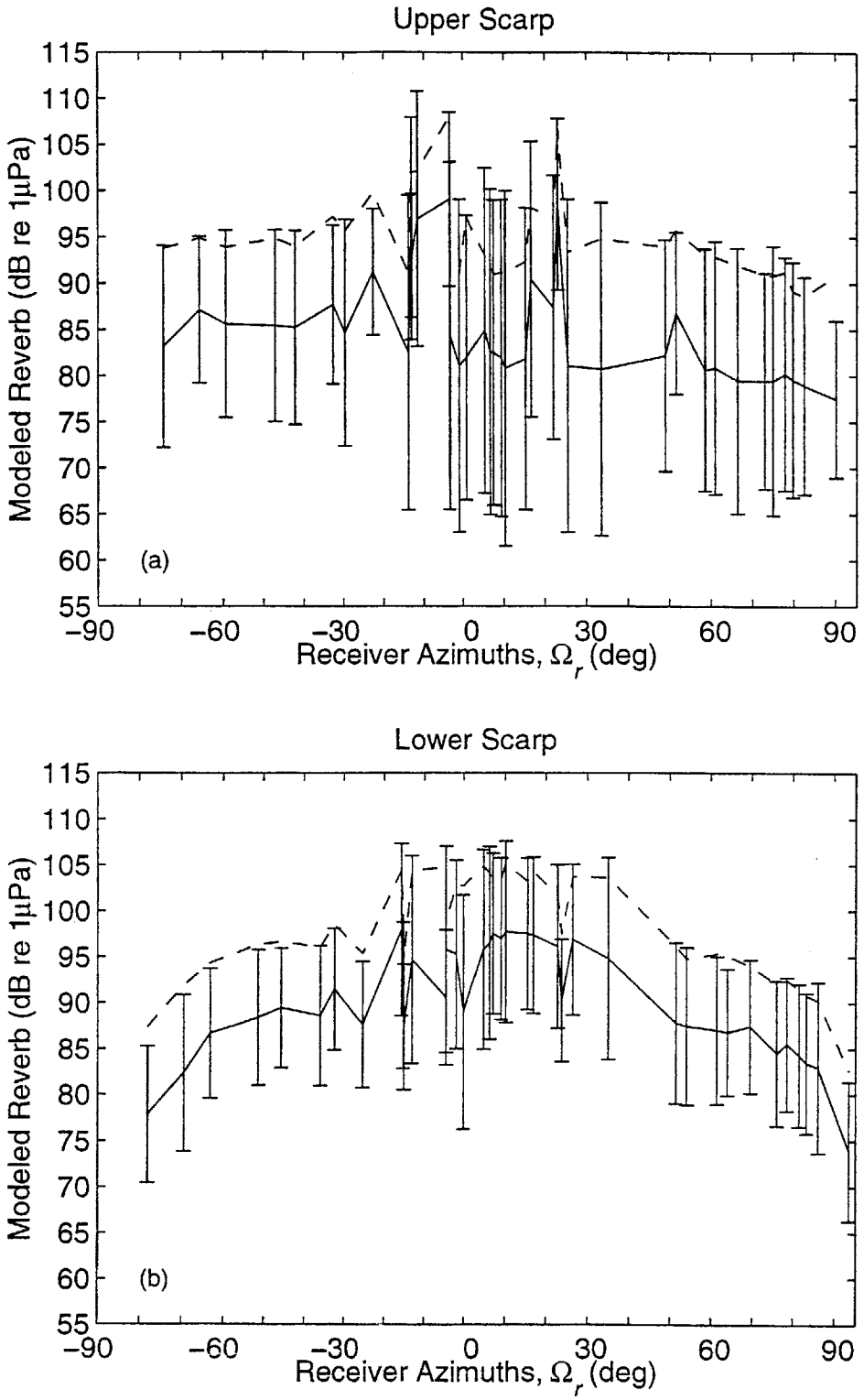

Figure 6-6: The mean reverberation level modeled over (a) the upper scarp $< R_M(x, y|\Omega_i, \Omega_r) >_{A_{up}}$ and (b) the lower scarp $< R_M(x, y|\Omega_i, \Omega_r) >_{A_{low}}$ as a function of receiver azimuth Ω_r along with their respective standard deviations $\sigma_{A_{up}}\{R_M(x, y)\}$ and $\sigma_{A_{low}}\{R_M(x, y)\}$. Solid line denotes the 200-m resolution curve, and dashed line denotes the 5-m resolution curve.

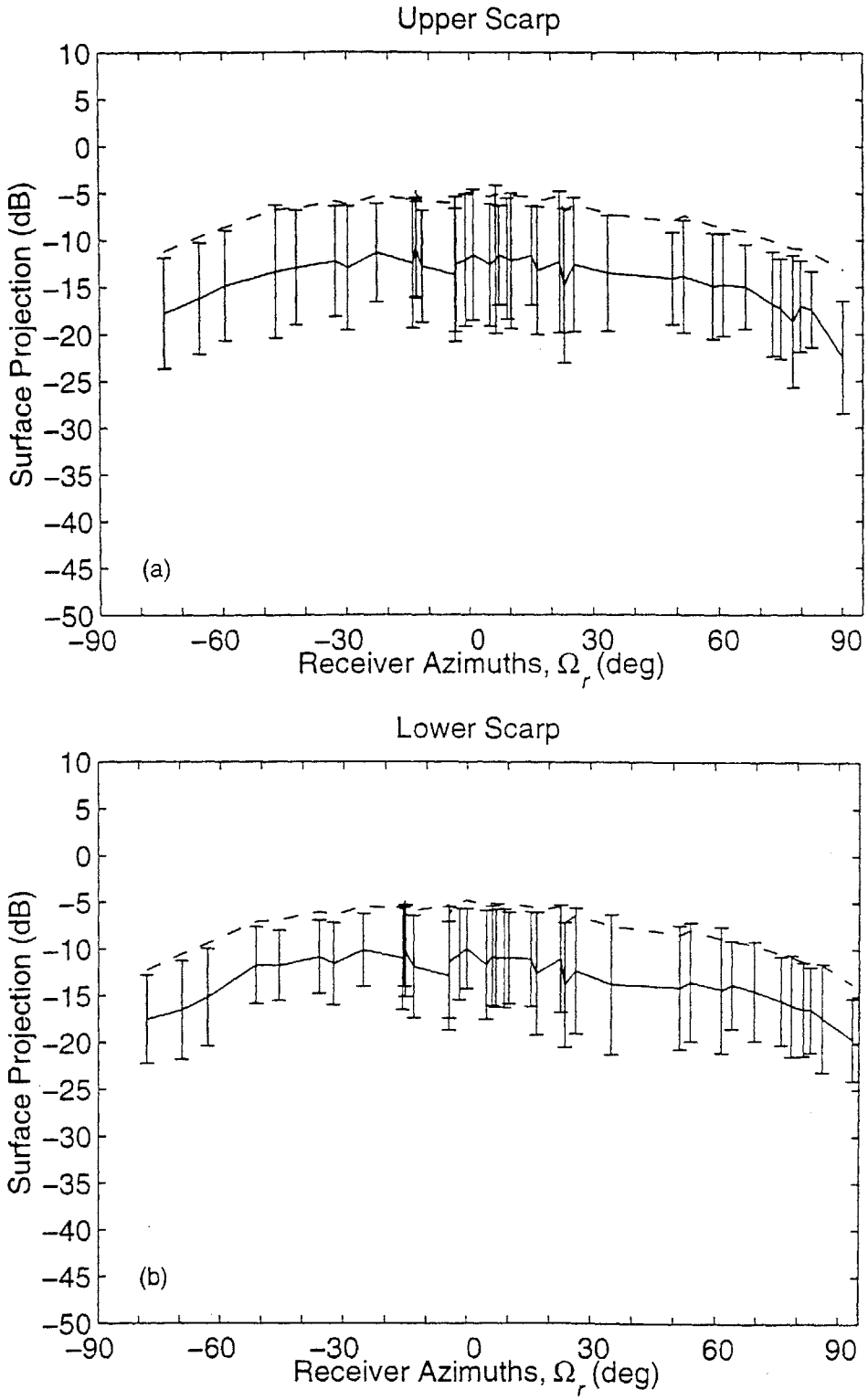

Figure 6-7: The mean surface projection, in dB, over (a) the upper scarp $< C_i(x, y|\Omega_i, \Omega_r) + C_r(x, y|\Omega_i, \Omega_r) >_{A_{up}}$ and (b) the lower scarp $< C_i(x, y|\Omega_i, \Omega_r) + C_r(x, y|\Omega_i, \Omega_r) >_{A_{low}}$ as a function of receiver azimuth Ω_r along with standard deviations. Solid line denotes the 200-m resolution curve, and dashed line denotes the 5-m resolution curve.

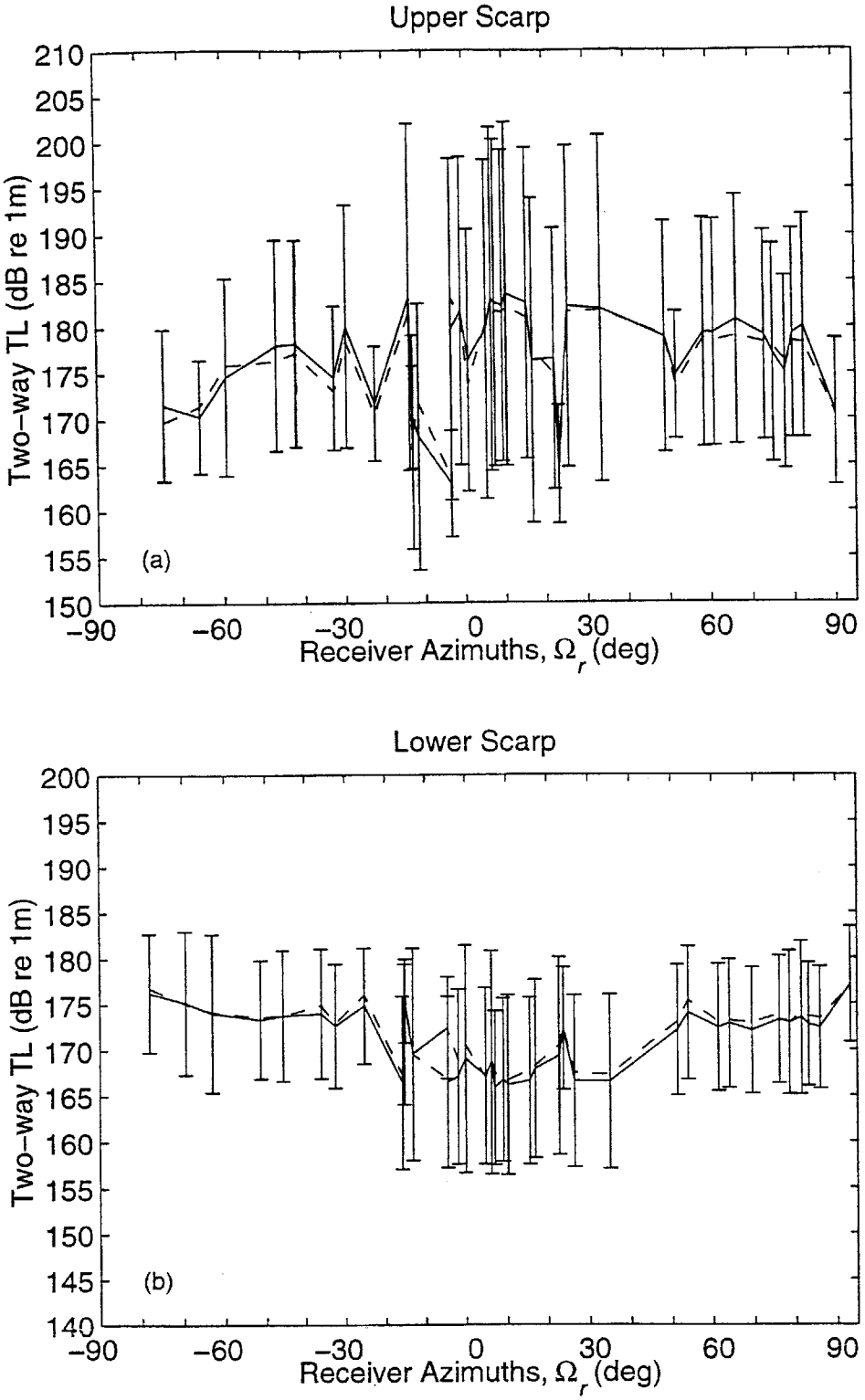

Figure 6-8: The mean 2-way transmission loss over (a) the upper scarp $< TL_i(x, y|\Omega_i, \Omega_r) + TL_r(x, y|\Omega_i, \Omega_r) >_{A_{up}}$ and (b) the lower scarp $< TL_i(x, y|\Omega_i, \Omega_r) + TL_r(x, y|\Omega_i, \Omega_r) >_{A_{low}}$ as a function of receiver azimuth Ω_r along with standard deviations. Solid line denotes the 200-m resolution curve, and dashed line denotes the 5-m resolution curve.

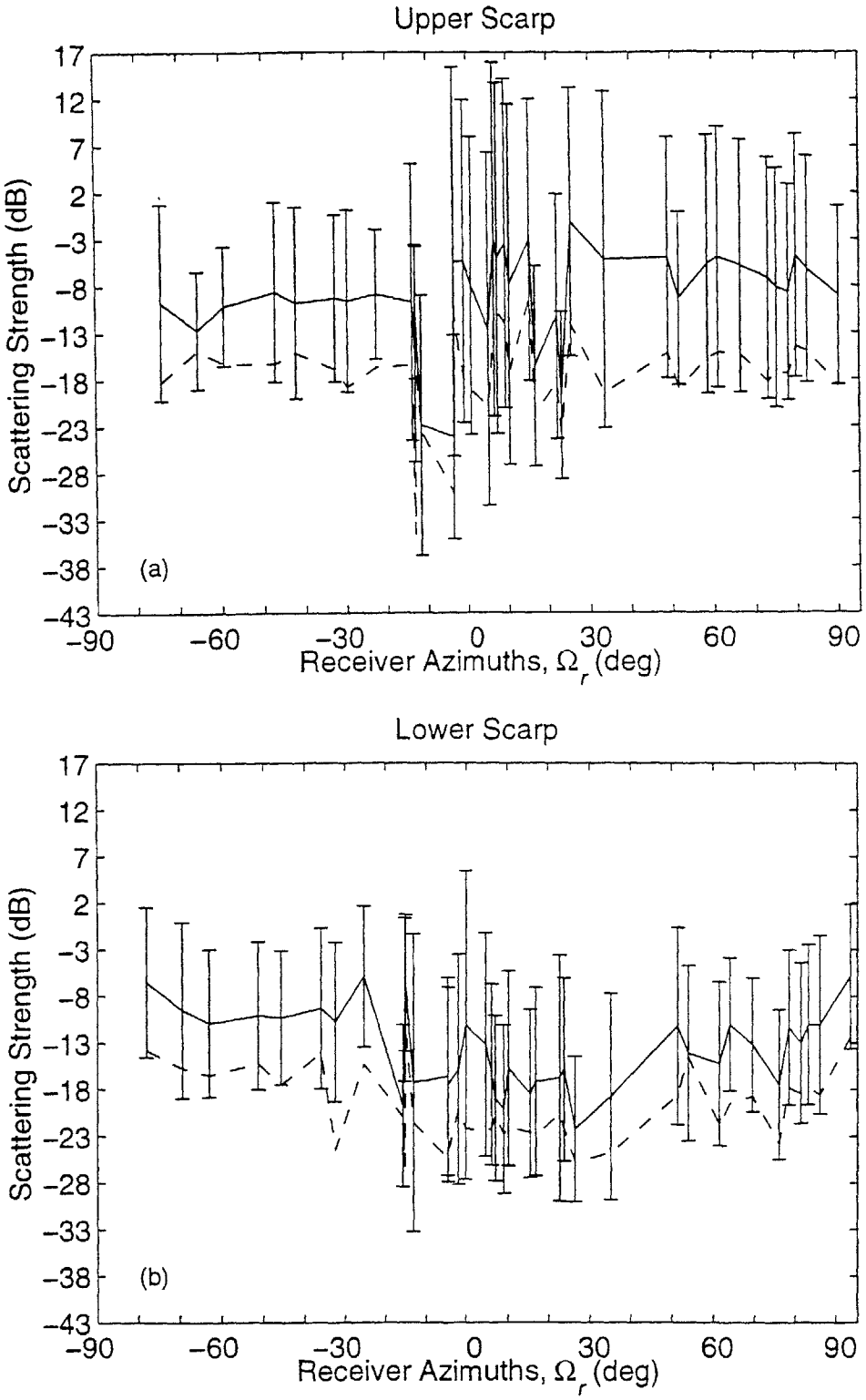

Figure 6-9: The MBASS curves estimated over (a) the upper scarp $< \hat{\bar{S}}(x, y|\Omega_i, \Omega_r) >_{A_{up}}$ and (b) the lower scarp $< \hat{\bar{S}}(x, y|\Omega_i, \Omega_r) >_{A_{low}}$ as a function of receiver azimuth Ω_r along with their standard deviations $\sigma_{A_{up}}\{\hat{\bar{S}}(x, y)\}$ and $\sigma_{A_{low}}\{\hat{\bar{S}}(x, y)\}$. Solid line denotes the 200-m resolution curve, and dashed line denotes the 5-m resolution curve.

6.2 COMPARISON BETWEEN B' AND C' SCATTERING DISTRIBUTIONS

For comparison purpose, the geomorphology of the two ocean ridges is given in Figure 6-9. While the B' ridge resembles an elliptical feature with long lineated scarps running parallel to its ridge axis, the C' ridge appears as a mound-like feature dominated by normal faults with variable orientations. The structural difference between these two classes of ocean ridge can be best illustrated by their directional derivative (DD) charts in Fig. 6.9(b) & (d). The two major scarps at B' are prominently displayed by two lines of positive DD parallel to its ridge axis. In contrast, the positive DD of C' appears sparsely scattered over the entire ridge, in accordance with its irregularly orientated faults.

In this section, the scattering distributions of the two geologically distinct ocean ridges are compared by examining their mean bi-azimuthal scattering strengths, measured and modeled reverberation at 200-m resolution. First, the mean reverberation levels measured across the C' scarp and the two B' scarps are plotted together as a function of receiver azimuth Ω_r in Figure 6-11. A typical standard deviation is plotted once on each curve to illustrate the spread of measured reverberation. Generally, the mean values of all three curves are uniform across $+/-90^0$ receiver azimuths. Although the mean reverberation measured over the C' scarp are a few dB lower than that of the B' scarps at several receiver azimuths, these minor differences lie within the standard deviations of roughly 6 dB. As a result, one may conclude that there is no significant difference between the mean reverberation levels measured over the B' and C' scarps at ½ CZ. More importantly, these three curves demonstrate that long-range reverberation measured over the major scarps of the two geologically distinct ocean ridges is spatially homogenous across the receiver azimuths within $+/- 90^0$.

The mean reverberation levels modeled over the C' scarp and the two B' scarps, at 200-m resolution, are plotted together as a function of receiver azimuth Ω_r in Figure 6-12. While the lower scarp and C' curves show a regular concave behavior with peak values within $|\Omega_r| < 30^0$, the upper scarp's curve exhibits some fluctuations within $|\Omega_r| < 30^0$, which often exceed 10dB. As discussed in Chapter 4, these fluctuations occur when the upper scarp falls into the shadow zone of the source main beam's refractive path. This shadowing effect is similarly revealed in the C' curve for $\Omega_r < -60^0$, where a 10 dB roll-off is observed. Apparently, the transmission loss

difference due to bathymetry-induced variations have caused these deviations in the modeled reverberation curves, which might otherwise follow a similar trend across Ω_r. The modeled reverberation over the lower scarp and C' show a better match, for $\Omega_r > -60^0$, since these two sites are well insonified by the source's main beam. The two-way transmission losses over these two sites are also similar, which leads to the good agreement in their modeled reverberation levels. On the other hand, the mean modeled reverberation of the upper scarp tends to deviate from these two curves due to large fluctuations of transmission loss within $|\Omega_r| < 30^0$.

Finally, the mean bi-azimuthal scattering strengths (MBASS) estimated over the C' scarp and the two B' scarps are plotted together as a function of receiver azimuth Ω_r in Figure 6-13. Large fluctuations in the upper scarp are observed due to the corresponding dips in its modeled reverberation curve. Although the MBASS of the C' scarp was estimated to -13dB +/- 10dB in Chapter 5, a constant line of -11 dB can be drawn across the entire receiver azimuths for the B' and C' curves, and still falls within all the error bars. Hence, this result suggests that there is no significant difference between the mean bi-azimuthal scattering strengths computed over these three sites. In other words, the mean bi-azimuthal scattering strengths of the steep scarps at B' and C' are comparable, and they are spatially homogenous across $+/-90^0$ receiver azimuths.

In the previous section, the MBASS curves of B' at 200-m resolution are found to be roughly 6 dB higher than the 5-m resolution curves, due to the lower slope gradients estimated in the 200-m resolution bathymetry data. For the same reason, one may speculate that the MBASS curve of C' should also be roughly 6 dB lower at 5-m resolution, assuming that the C' scarp is equally steep as the B' scarps at 5-m resolution measurements. Since the scattering characteristics of the B' scarps at the two resolutions behave similarly across the entire receiver azimuths, the scattering characteristics of the C' scarp are likely to have the same trend in both resolutions as well. This leads to the suggestion that our empirical scattering function derived for the two B' scarps at 5-m resolution should also hold well for the C' scarp. In other words, the evidence indicates that the bi-azimuthal scattering strengths of the major scarps at the two distinct ocean ridges are identical; and they can be modeled as the azimuth-independent constant of -17dB +/- 8dB.

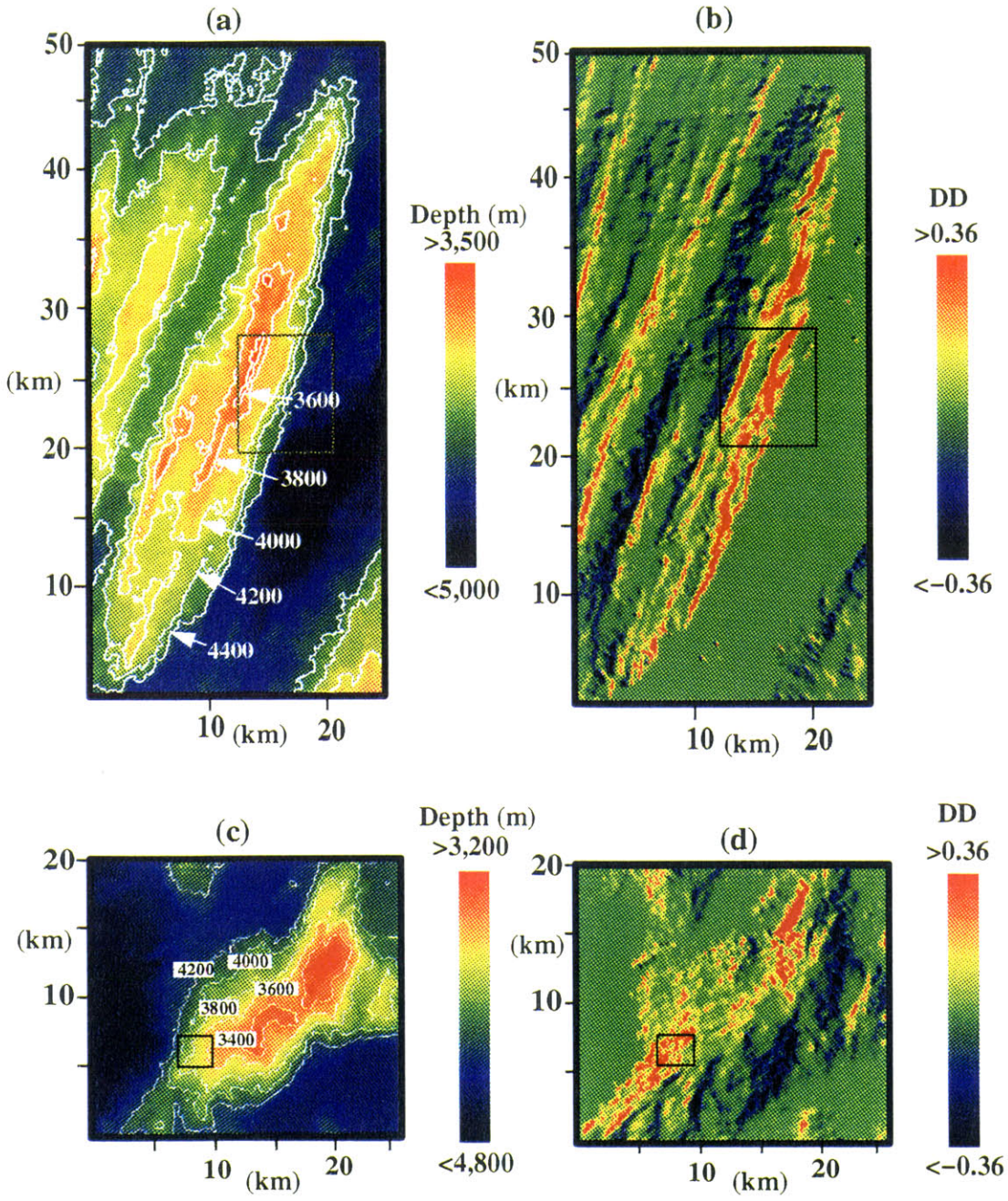

Figure 6–10: Comparison between the B' and C' bathymetric features and their corresponding directional derivatives (DD) charts. (a) The 200–m resolution bathymetry of the B' ridge. (b) The DD of B' with source insonification from the East. (c) The 200–m resolution bathymetry of the C' ridge. (d) The DD of C' with source insonification from the West.

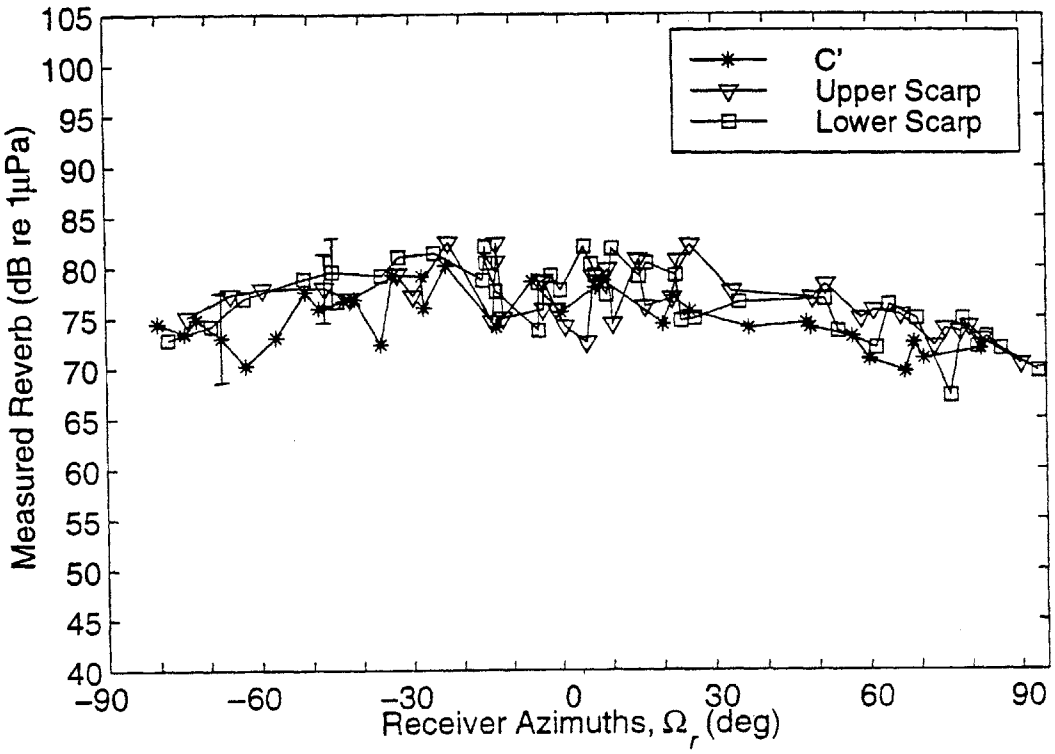

Figure 6-11: The mean reverberation levels, at 200-m resolution, measured over the C' scarp and the two B' scarps as a function of receiver azimuth Ω_r. Their typical standard deviations are plotted on each curve to illustrate the spread of measured reverberation.

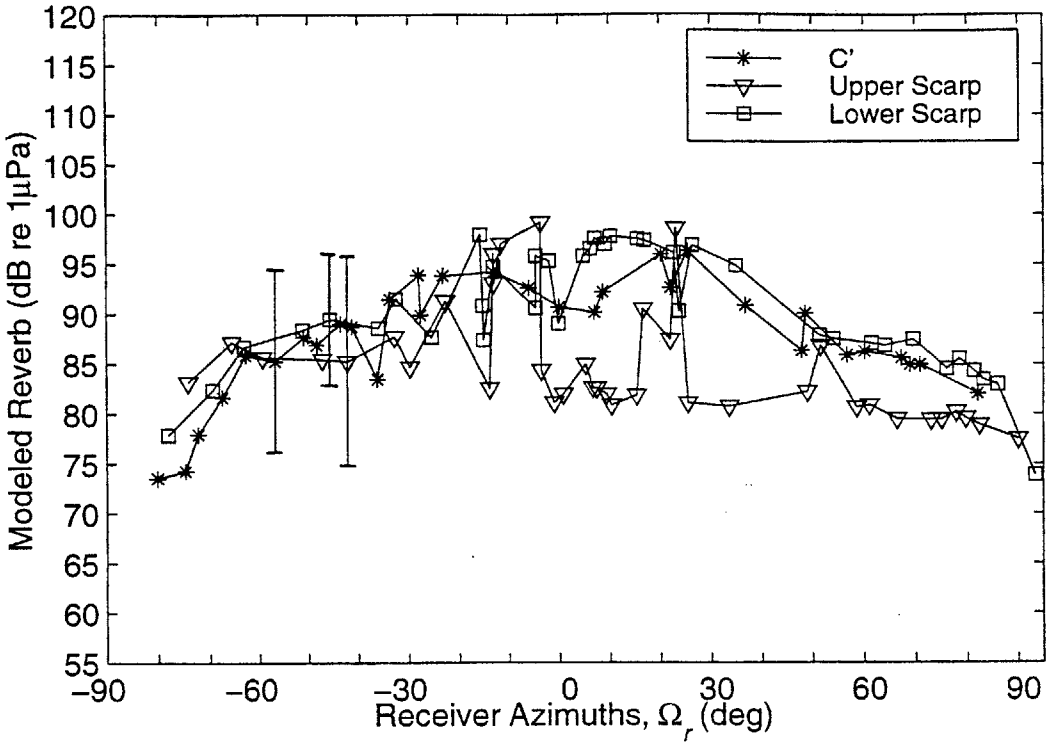

Figure 6-12: The mean modeled reverberation levels, at 200-m resolution, computed over the C' scarp and the two B' scarps as a function of receiver azimuth Ω_r. Their typical standard deviations are plotted on each curve to illustrate the spread of modeled reverberation.

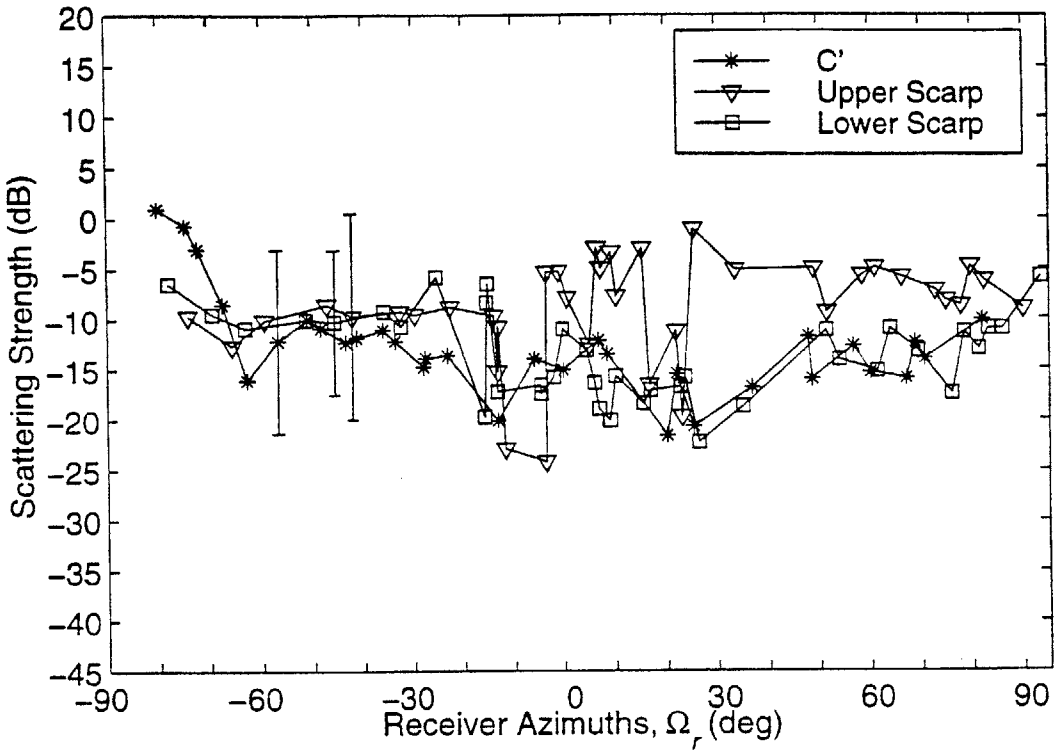

Figure 6-13: The mean bi-azimuthal scattering strengths, at 200-m resolution, estimated over the C' scarp and the two B' scarps as a function of receiver azimuth Ω_r. Their typical standard deviations are plotted on each curve to illustrate the spread of scattering strengths.

7 CONCLUSIONS

7.1 SUMMARY

In this thesis, the bistatic reverberation data collected by a system of low-frequency towed arrays at two selected ocean ridges, known as B' and C', during the Main Acoustics Experiment of 1993 have been processed and analyzed. This study is motivated by the fact that B' and C' belong to the two geologically distinct classes of ocean ridges that span the MAR. Their scattering distributions might therefore be characterized according to their respective geomorphologic features for identifying the other uncharted ocean ridges in the MAR. Concurrently, the effective resolving power of a towed-array system in imaging the seafloor geomorphology, and the effects on scattering strength estimation using two different resolutions of bathymetry data at B' have also been evaluated.

Some of the previous analyses, conducted by Prof. Makris and his former group at NRL-DC, are reviewed in Chapter 1. They have demonstrated that prominent echoes are returned from extended ridges with steep scarps such as B', and these echo returns are highly correlated with negative transmission loss. Subsequently, a further study was carried out to measure the bi-azimuthal scattering distributions of the two major scarps at B' using the supporting 5-m resolution bathymetry data, which led to the first part of this thesis.

During the experiments, as described in Chapter 2, the RV Cory employed a ten-element vertical source array, and transmitted from roughly ½ CZ (~33 km) to each selected ridge along waterborne paths. The returned echoes from these two ridges were measured by horizontal line arrays towed behind the RV Cory and Alliance. In this thesis, we only analyze the towed-array data associated to the Cory's LFM transmission (200-255 Hz) which provides the best range resolution for the towed-array imaging system. These data are extracted from the 8 mm magnetic tapes via an off-line computer system, and processed into reverberation images on a two-dimensional Cartesian map projection, as illustrated in Chapter 3.

A simple slant-range conversion method is used to compute the travel time for the wide-area reverberation images, which are subsequently checked to ensure the left-right ambiguity of towed-array is not a problem for our analysis. To achieve the required range accuracy, a range-dependent ray tracing is used to produce the high resolution reverberation images. In our modeling, the two-way transmission loss is computed by a Parabolic Equation technique, and the surface projection of bathymetry is computed via ray tracing. This model assumes a diffusely scattering surface at B' and C', and a spatial convolution is implemented to chart reverberation within the sonar resolution footprint. A full description of our model is presented in Section 4-4 and Ref. [14].

In the first part of this thesis, the bi-azimuthal scattering distributions of the two major scarps at B', an outside corner, are evaluated using the supporting 5-m resolution bathymetry data. This work is primarily conducted by Makris and Fialkowski. Generally, the modeled and measured reverberation show high visual correlation in the monostatic and bistatic images, and prominent echo returns are observed to resolve the upper and lower scarps distinguishably when the cross-range axis of sonar footprint coincides with the scarp axes. However, one-to-one correspondence between small-scale features in the modeled and measured reverberation along the scarp axes is sometimes absent when the bistatic separation is large. The most plausible explanation for this discrepancy is that signal-dependent noise, known as speckle, is sufficient to mask out the echo pattern since the variations predicted by the model along the scarp axes are on the order of 5.6 dB standard deviation of the speckle noise.

We have also demonstrated that the B' scarp's bathymetry within the sonar resolution footprint cannot be approximated as a planar surface. It is therefore meaningless to plot the scattering strength as a function of incident and scattered angles. Instead, a mean bi-azimuthal scattering strength (MBASS) of the B' scarps is computed as a function of receiver azimuth within $+/-90^0$ of the normal horizontally bisecting the scarp axis. Consequently, the mean bi-azimuthal scattering strengths of the two B' scarps are found to be identical, and roughly equal to the constant of -17dB +/- 8dB. A detailed analysis is presented in Chapter 4.

In the second part of this thesis, the same approach is used to measure the bi-azimuthal scattering distribution of a major scarp at C', an inside corner, using the supporting 200-m resolution bathymetry data. Unlike the outside corner B', which has long and lineated scarps, the

inside corner C' is characterized by irregularly oriented faults. A comparison of their bi-azimuthal scattering strengths is therefore useful since they span the two geologically distinct classes of ocean ridges found in the MAR. A steep scarp at the south-west corner of C' is subsequently chosen for our study since it is well insonified by the sonar source's main beam throughout the experiments. Our results show that the MBASS of the C' scarp is roughly equal to the constant of -13dB +/- 10dB, and its surface projection is typically 6-10 dB lower than the surface projections of the B' scarps at 5-m resolution. This difference is caused by the slope gradients of bathymetry that are under-estimated in the 200-m resolution sampling.

As such, the bi-azimuthal scattering distributions of the B' scarps are re-evaluated using the 200-m resolution bathymetry data so as to compare the scattering characteristics of B' and C' appropriately. It is found that the 200-m resolution MBASS of the B' scarps are equal to the constant of -11dB +/- 10dB, and are roughly 6 dB higher than the previous results obtained at 5-m resolution. This scattering strength difference can be accounted for by the surface projection difference measured over the two resolutions of bathymetry data. The smaller surface projection computed at 200-m resolution, which arises from the under-resolved slope gradients, has resulted the higher scattering strength estimations.

For comparison purpose, the MBASS curves obtained for the B' and C' scarps at 200-m resolution are plotted together as a function of receiver azimuth in Section 6-2. It is found that a constant line of -11 dB can be drawn across the entire receiver azimuths for these MBASS curves, and still falls within all the error bars. Hence, this result suggests that their mean bi-azimuthal scattering strengths are comparable; and they are spatially homogenous across the receiver azimuths within $+/-90^0$ of the normal horizontally bisecting the scarp axis.

7.2 CONCLUSIONS

The research objectives of this thesis, as stated in Section 1-4, are achieved as follows:

- The bistatic scattering returns from the two major scarps of B' received by a towed-array imaging system have been analyzed. We have demonstrated, via the wide-area and high resolution reverberation image charts, that prominent echo returns deterministically image the scarp morphology when the cross-range resolution of the towed-array system runs along the scarp axis. Although the small-scale features along the scarp, such as canyons and gullies (~100-200 m scale), are theoretically resolvable in range by the towed-array system at large bistatic angles, statistical fluctuations due to signal-dependent noise present in the actual data prevent the system from resolving these features. This leads to a conclusion that signal-dependent noise, known as speckle, is one of the primary factors limiting the towed-array system's resolving power in imaging the seafloor geomorphology.

- Based on our results obtained for the two B' scarps at 5-m resolution, their mean bi-azimuthal scattering strengths are found to be identical, and roughly equal to the constant of -17dB +/- 8dB. This proposes that the empirical scattering functions for the B' scarps can be modeled as Lambertian scatterers with albedo $\pi/10^{1.7}$. Spatial variations in the transmission loss and seafloor projected area are also found to account for the dominant variations in measured reverberation. This finding suggests that long-range reverberation from the ocean basin can be well predicted if the refractive index of the water column and the ocean bottom bathymetry, at sufficient resolution, are provided.

- The bi-azimuthal scattering distributions of the two major scarps at B' are further evaluated using the 200-m resolution bathymetry data. The mean bi-azimuthal scattering strengths computed over the two different resolutions of bathymetry data at B' are found to differ by their surface projection difference (~ 6dB), which arises from the under-estimated slope gradients in the 200-m resolution sampling. This finding indicates that sufficient sampling of the bathymetry data is necessary to accurately estimate the

seafloor's scattering strengths. Using low-resolution bathymetry data tends to over-estimate the scattering strengths of seafloor features because of the under-resolved slope gradients, as revealed by our results obtained for the B' scarps.

- The bi-azimuthal scattering distributions of the two distinct classes of ocean ridges, B' and C', are compared at 200-m resolution. Our results indicate that the bistatic scattering characteristics of the B' and C' scarps are similar. In particular, their mean bi-azimuthal scattering strengths are found to be comparable; and both are spatially homogenous across the receiver azimuths within $+/-90^0$ of the normal horizontally bisecting the scarp axis. If the slope gradients of these B' and C' scarps are assumed to be equally steep, we would expect their scattering strengths to be similar at 5-m resolution as well. This leads to the hypothesis that these two classes of ocean ridges can be modeled as diffuse scatterers with a constant bi-azimuthal scattering strength of -17dB +/- 8dB when remotely imaged by the towed-array system at ½ CZ range and beyond. This result also suggests that ridges throughout the MAR can be modeled as diffuse scatterers with albedo $\pi/10^{1.7}$.

BIBLIOGRAPHY

1. N. C. Makris, "Proposed experiment," in Acoustic Reverberation Special Research Program Research Symposium, Woods Hole oceanographic Institution (1992).

2. N. C. Makris, L. Avelino, R. Menis, "Deterministic reverberation from ocean ridges," J. Acoust. Soc. Am. **97**, 3547-3574 (1995).

3. N. C. Makris and J. M. Berkson, "Long-range backscatter from the Mid-Atlantic Ridge," J. Acoust. Soc. Am. **95**, 1865-1881 (1994).

4. J. Orcutt, Editor, *Acoustic Reverberation Special Research Program, Initial Report,* Scripps Institution of oceanography (1993).

5. B. E. Tucholke and J. Lin, "A geological model for the structure of ridge segments in slow spreading ocean crust," J. Geophys. Res. **99**, 11937-11958 (1994).

6. B. K. P. Horn and R. W. Sjoberg, "Calculating the reflectance map," Applied Optics Vol. **18**, No 11, 1770-1779 (1979).

7. J. R. Preston, E. Michelozzi, L. Troiano, and R. Hollett, *Cruise report on RV Alliance cruise MARE July 5 - August 1, 1993 SACLANTCEN's joint experiment with ONR's ARSRP Group,* SACLANT Undersea Research Centre, LaSpezia, Italy (1993).

8. N. C. Makris, "Imaging ocean-basin reverberation via inversion," J. Acoust. Soc. Am. **94**, 983-993 (1993).

9. N. C. Makris, "The effect of saturated transmission scintillation on ocean acoustic intensity measurements," J. Acoust. Soc. Am. **100**, 769-783 (1996).

10. J. R. Preston and W. A. Kinney, "Monostatic and bistatic reverberation results using linear frequency-modulated pulses," J. Acoust. Soc. Am. **93** (5), 2549-2565 (1993).

11. J. W. Goodman, *Statistical Optics*, (John-Wiley and Sons, New York, 1985).

12. F. B. Hildebrand, *Advanced Calculus for Applications*, (Prentice-Hall, Eaglewood Cliffs, NJ, 1976).

13. N. C. Makris, C. S. Chia, and L. T. Fialkowski , "A comparison of bistatic scattering from two geologically distinct mid-ocean ridges," in Proceedings 16th International Congress on Acoustics and the 135th meeting of the Acoustical Society of America, Seattle, USA, 20-26 June 1998, pp. 2705-2706.

14. N. C. Makris, C. S. Chia and L. T. Fialkowski, "The bi-azimuthal scattering distribution of an abyssal hill," J. Acoust. Soc. Am. (submitted in August 1998).

15. Y. Y. Dorfman, "Bistatic scattering of acoustic waves from a rough ocean bottom," Ph.D. thesis, MIT, Cambridge, MA, 1997.

16. H. Cox, "Fundamentals of bistatic active sonar," in *Underwater Acoustic Data Processing*, edited by Y. T. Chan (Kluwer Academic Publishers, Boston, USA, 1989), pp. 3-23.

17. A. J. Harding, M. A. H. Hedlin, and J. A. Orcutt, "Migration of backscatter data from the Mid-Atlantic Ridge," J. Acoust. Soc. Am. 103, 1787-1803 (1998).

18. J. W. Caruthers and E. J. Yoerger, "Modeling low-frequency reverberation near the Mid-Atlantic Ridge and comparison with ARSRP data," J. Acoust. Soc. Am. 101(5), 2555-2565 (1997).

19. N. C. Makris and B. Gardner, "Planned tracks/waypoints, runs 3-9," in Acoustics Reverberation Special Research Program Main Acoustics Experiment, Initial Report, Scripps Institution of Oceanography (1993), pp. 65-80.

20. N. C. Makris, "MFA beampattern," in Acoustic Reverberation Special Research Program Main Acoustics Experiment, Initial Report, Scripps Institution of Oceanography (1993), pp. 204-208.

21. R. C. Spindel and J. R. Heirtzler, "Long-Range Echo Ranging," J. Geophys Rev. **77**, 7073-7078 (1972).

22. D. E. Shifter, E. R. Franchi, J. M. Griffin, and B. B. Adams, "Hydrographic Reconnaissance of Large Undersea Topography using Scattered Energy," in Rec. 1980 IEEE Electron. Aerospace Syst. Conventions, 270-274 (1980).

23. F. T. Erskine, G. M. Bernstein, S. M. Brylow, W. T. Newbold, R. C. Gauss, E. R. Franchi, and B. B. Adams, "Bathymetric Hazard Survey Test (BHST Rep. No. 3), Scientific Results and FY 1982-1984 Processing," NRL Rep. 9048 (1987).

24. J. M. Berkson and T. Akal, "Simultaneous Reception of Long-Range Low-Frequency Backscattered Sound by a Vertical and Horizontal Array," IEEE J. Ocean. Eng. **OE-12**, 362-367 (1987).

25. J. R. Preston, T. Akal, and J. M. Berkson, "Analysis of backscattering data in the Tyrrhenian Sea," J. Acoust. Soc. Am. **87**, 119-134 (1990).